Electrokinetics in reactive and conical channels

Not-so-linear transport of charge, fluid, and salt

ISBN: 978-90-393-7551-8

About the cover: Pictured is a mountain stream transporting minerals from Alpine glaciers to sea level. The stream on the cover flows down Dôme de Chasseforêt, behind which lies Glacier de Péclet. The Péclet number plays a central role in this thesis, quantifying whether transport is dominated by flow or by diffusion.

Electrokinetics in reactive and conical channels

Not-so-linear transport of charge, fluid, and salt

Elektrokinetiek in reactieve en kegelvormige kanalen

Net-niet-lineair transport van lading, vloeistof, en zout

(met een samenvatting in het Nederlands)

Proefschrift

ter verkrijging van de graad van doctor aan de
Universiteit Utrecht
op gezag van de
rector magnificus, prof.dr. H.R.B.M. Kummeling,
ingevolge het besluit van het college voor promoties
in het openbaar te verdedigen op

maandag 17 april 2023 des ochtends te 10.15 uur

door

Willem Quirin Boon

geboren op 31 mei 1994
te Haarlem

Promotoren:

Prof. dr. R.H.H.G. van Roij
Prof. dr. ir. M. Dijkstra

Beoordelingscommissie:

Prof. dr. A. van Blaaderen
Prof. dr. R.A. Duine
Dr. B.H. Erné
Prof. dr. P.E. de Jongh
Prof. dr. F.G. Mugele

The hardest thing of all to see is what is really there.
- J.A. BAKER, *The Peregrine*

List of publications

In this thesis

1. P. Ober*, W. Q. Boon*, M. Dijkstra, E.H.G. Backus, R. van Roij, & M. Bonn, (2021). *Liquid flow reversibly creates a macroscopic surface charge gradient*†, Nature communications, 12(1), 1-11.

2. W.Q. Boon, M. Dijkstra, & R. van Roij, *Coulombic surface-ion interactions induce non-linear and chemistry-specific charging kinetics* (2023), Physical Review Letters, 130, 058001

3. W. Q. Boon*, T. E. Veenstra*, M. Dijkstra, M, & R. van Roij, (2022). *Pressure-sensitive ion conduction in a conical channel: optimal pressure and geometry*. Physics of Fluids, 34(10), 101701.

4. M. Aarts*, W.Q. Boon*, B. Cuénod, M. Dijkstra, R. van Roij, & E. Alarcon-Llado (2022). *Ion current rectification and long-range interference in conical silicon micropores*††, ACS Applied Materials & Interfaces.

Other publications by the author

- D.C. Yu, F.T. Rabouw, W. Q. Boon, T. Kieboom, S. Ye, Q.Y. Zhang, & A. Meijerink, (2014). *Insights into the energy transfer mechanism in Ce^{3+}-Yb^{3+} codoped YAG phosphors.* Physical Review B, 90(16), 165126.

- T. Kamsma, W.Q. Boon, T. ter Rele, C. Spitoni, & R. van Roij, *Iontronic neuromorphic signalling with conical microfluidic memristors*, Submitted, arXiv preprint arXiv:2301.06158

- H. Tao*, W.Q. Boon*, & R. van Roij, *How an electrochemical electrode sheds its double layer: electric double layer inversion and negative capacitance*, In preparation

*These authors contributed equally

†The experimental work for this publication was performed by P.O., E.H.G.B, and M.B. at the Max Planck Institute for Polymer Research in Mainz

††The experimental work for this publication was performed by M.A., B.C., and E.A. at AMOLF in Amsterdam

Contents

Chapter 1

Introduction

> Pumping through a trillion hearts and flowing over two-thirds of the earth's surface, few subjects are more deserving of study than the movement of salty liquids.

1.1 Introduction for a general audience

In this thesis we will describe the transport of liquids carrying dissolved salt, known as electrolytes. Our aim is to describe how much charge, liquid, and chemicals move from location A to location B per unit of time. Such transfer is critical for biology, where it nurtures cells, but also for industry, where it is used to purify our drinking water. Besides being crucially important, the transport of charge, liquid and chemicals is also so commonplace that it can even be observed when brewing your morning cup of coffee.

Transport in everyday life When turning on the coffee machine, a current of charge runs from the socket at high voltage to the machine at low voltage. Subsequently, fluid flows from the reservoir at high pressure to the filter at low pressure. Finally, diffusion of caffeine occurs from the coffee grounds at high concentration to the water at a low concentration. In all these examples transport occurs because substances are driven to lower energies, as a difference in

- **voltage** (energy/charge) moves **charges**,
- **pressure** (energy/volume) moves **fluid volume**,
- **concentration** ($\sim$energy/#atoms) moves **atoms**.

While in your coffee machine all these transport phenomena occur separately, in electrolytes they occur simultaneously at the same position and hence movement of charges, fluid and chemicals become intricately connected. Due to this connection it is possible to drive flow using voltage and charges using pressure. At first sight, such transport is strange as the units of driving potentials and transported substance do not match. In such cases it would be unclear why, and in what direction, this transport would even occur.

As we will demonstrate in later sections of the Introduction such transport in electrolytes, known as electrokinetics, occurs quite spontaneously. Transport

where the units of the transported substance do not match its driving force was first discovered in 1794 [1], when dead frogs were animated by currents driven by temperature differences, and was independently rediscovered in 1822 [2]. It has fascinated physicists ever since, but its behaviour remained mysterious until the governing laws were found in 1931 [3]. This theory assumes a linear relation between transport and driving potentials to hold: Ohm's law is a prime example of such a linear relation where increasing the voltage difference over a resistor ten-fold will yield ten-times more current. But why then does the title refer to "not-so-linear" transport?

Linear or nonlinear transport? The term "not-so-linear" is due to experimental observations which show that this linearity actually breaks down already in relatively simple electrolyte systems, such as reactive and conical channels. What makes all these findings surprising is that these deviations from linearity occur in systems which only differ minutely from a charged, straight, non-reactive, channel for which transport is linear over a large range of driving forces. Examples of non-linearities in this thesis are conical pores which allow an electric current to go through only one way and reactive channels whose charge changes with flows. Furthermore we show that even chemical kinetics become non-linear at the electrolyte-mineral interface. For all these problems we have to disentangle the subtle interplay of fluid flow, electric currents, and chemical transport responsible for the observed deviations from linearity.

The following sections in this Introduction will start by introducing the governing equations for fluid and ions after which we will derive the well-known linear response relations for a straight, non-reactive, channel. During the derivation we highlight which details are crucial for the understanding of electrokinetic experiments. Many methods and considerations in the Introduction will prove useful in later Chapters. In Section 1.2 we use single-particle dynamics to derive the governing equations for electric fields, fluid and ions in electrolytes. Subsequently, in Section 1.3 we zoom out to derive the linear transport relations for a straight, non-reactive, micrometer cylinder. Finally in Section 1.4, we zoom out even further to discuss the limits set on such transport relations by thermodynamics. Gradually moving from microscopic (atomic) to macroscopic (micrometer) transport, we show that for relatively plain microscopic physics it is easy to obtain rich and complex macroscopic physics. In the Introduction we focus on linear transport through a non-reactive, straight, cylindric channel while in the rest of the thesis we consider non-linear transport through reactive and conical channels.

Introductory notes As in the Introduction we treat a wide variety of physics the following sections will necessarily be compact. For longer expositions we refer to Ref. [4] for electrostatics, Refs. [5, 6] for fluid mechanics, to Ref. [7]

for treatment of the Langevin equation and the seminal papers Refs. [3, 8, 9] for the thermodynamics of linear-response. For Poisson-Boltzmann theory and its range of validity we recommend Ref. [10] while the Supplementary Material of Ref. [11] was often consulted for the derivation of electrokinetic linear response relations. We recommend Refs. [12, 13] for excellent introductions to the surface chemistry of mineral-water interfaces.

1.2 Governing equations for dilute electrolytes

In this second section of the Introduction, we derive the equations of motion for momentum, mass, charge and ions in dilute electrolytes, known as the Poisson-Nernst-Planck-Stokes equations by considering single particle motion. The phenomena introduced in this section constitute well-known 19th and 20th century physics, and during their derivation we discuss sensible ways of dealing with such equations for transport problems. Furthermore, we estimate the relevant time- and length-scales of transport relevant in microfluidic experiments.

Usually the non-equilibrium governing equations are derived by considering a perturbation to a thermodynamic equilibrium state, but here we choose to present a purely kinetic derivation. This ensures not only that the mathematical machinery remains light, but also puts us on sure footing when transport becomes non-linear (as derivations from thermodynamics usually imply a linearization). However, our derivation which considers the movement of single ions, extends poorly to dense electrolytes which require the treatment of particle interactions beyond mean field.

1.2.1 Continuity and conservation

Before delving into the specifics of transport, it will be useful to consider general transport behaviour of an abstract quantity φ, allowing us to find properties the trajectory of φ must obey in steady-state where $\partial_t \varphi = 0$. These properties can often be used to sketch out a solution before doing any calculations.

For any transported quantity φ the continuity equation

$$\partial_t \varphi = S_\varphi - \nabla \cdot (\varphi \mathbf{u}_\varphi), \tag{1.1}$$

describes the local change in the quantity $\partial_t \varphi$ as function of its local velocity $\mathbf{u}_\varphi$ and local source strength S_φ, which is a source when $S_\varphi > 0$ and a sink when $S_\varphi < 0$. The continuity equation essentially states that if transport does not balance production then either accumulation or depletion must occur. In principle ions should be conserved as they carry both mass and charge, but in Chapter 2 and 3 we will see that chemical reactions can add ions to an electrolyte solution through charge separation and dissolution of a solid. Similarly, momentum ought to be

conserved but can actually be injected into the electrolyte through an externally applied gravitational or electric field.

When no sources are present anywhere, the transport must be divergence-free everywhere ($\nabla \cdot \mathbf{u}_\varphi = 0$) and in this case the trajectory of fluid and ions must either form closed loops, or extend to infinity. Trajectories starting at a source must either end in a sink, or also extend to infinity. Such a trajectory, also known as a streamline $\mathbf{z}_\varphi(s)$ with s the parametrization of the streamline, always follows the local velocity $\mathbf{v}_\varphi$ and hence can be found by solving for $\mathrm{d}\mathbf{z}_\varphi(s)/\mathrm{d}s \times \mathbf{v}_\varphi = 0$. As the velocity can only have a single value at every position, this definition directly shows that streamlines can never intersect. These properties often allow one to sketch paths that momentum, ions and fluids will take before really grappling with any equations [14].

1.2.2 Electric fields

To induce net transport of ions or fluid requires a force to change their momentum. While such forces can be exerted locally by atomic collisions, it is also possible to inject momentum into an ion over long ranges through an electric field. Here we will briefly discuss the laws governing electric fields, and by what methods explicit expressions for electric fields can be found.

Poisson equation From experimental observation it is known that the electric field $-\nabla\psi$ at position $\mathbf{r}$ resulting from a single proton charge e in the origin $\mathbf{0}$ is given by the Coulombic inverse-square law

$$-\nabla\psi = \frac{\hat{\mathbf{r}}}{|\mathbf{r}|^2}\frac{e}{4\pi\varepsilon}, \tag{1.2}$$

with $\hat{\mathbf{r}}$ the unit vector, and the dielectric permittivity ε which in water is 4.4 e (mV μm)$^{-1}$. This inverse-square law is valid as long as the velocity and acceleration of the ions (with respect to that of the fluid) is slow enough for relativity to be negligible. As the divergence of the field is entirely localized at the origin $\nabla^2\psi = -e\delta(\mathbf{r})/\varepsilon$, with $\delta(\mathbf{r})$ the Dirac delta function, it can be seen that every (static) electric field ultimately results from a charge. This electric field is linear in charge e, and hence the electric field of a continuous (negative) charge density $e\rho_\mathrm{e}(\mathbf{r})$ is given by the sum of fields from the individual charges resulting in

$$\nabla^2\psi = -\frac{e}{\varepsilon}\rho_\mathrm{e}(\mathbf{r}), \tag{1.3}$$

which is the well-known Poisson equation. Strictly speaking ρ_e is not a source of electric field in the sense of the continuity Eq. (1.1), however it is possible to construct streamlines $\mathbf{z}_{\nabla\psi}(s)$, obeying $\mathbf{z}_{\nabla\psi}(s) \times \nabla\psi = 0$, which actually describe

the paths ions in water would take were there no flow or diffusion. Such a particle trajectory, known as an electric field line, starts at a positive and terminates at a negative charge distribution when the total system is charge neutral.

Gauss' law While the Poisson equation is hard to solve for general charge distributions $\rho_e(\mathbf{r})$, some simple solutions are known when the charge distribution is localized on a two-dimensional surface. In such cases the two-dimensional charge distribution $e\sigma(\mathbf{r})$ defines the electric field normal to the charged surface by Gauss' law

$$\hat{\mathbf{n}} \cdot \nabla \psi = -\frac{e}{\varepsilon}\sigma, \tag{1.4}$$

where $\hat{\mathbf{n}}$ is the inward pointing normal vector of the charged surface. In such cases the approach is often to use Gauss' law as as a boundary condition to the Laplace equation $\nabla^2\psi = 0$, which is much simpler to solve than the Poisson Eq. (1.3). For several highly-symmetric geometries such as spheres, cylinders and parallel plates the Laplace equation can be simplified even further by using symmetries to reduce it to a one-dimensional ordinary differential equation. Some classical results following this approach can be found in [4]. Such simple results can be used to construct solutions for more complicated problems by, carefully, gluing several simple solutions together, as we show in Chapter 2 and 4.

1.2.3 Fluid mechanics

When electric fields change the momentum of ions, this momentum is quickly dissipated in the fluid thereby setting it into motion. Interestingly, we will see that the mechanism by which momentum is transported is similar to the mechanism by which particles are transported, namely diffusion. While fluid mechanics can be quite complex and rich in its own right, in this section we will show that at small (micrometer) scales the equations governing flow can be dramatically simplified.

Incompressibility When there is no net force, the momentum density $\mathbf{p} = \rho_m \mathbf{u}$ over a closed system should be conserved, where ρ_m is the mass density and $\mathbf{u}$ (without subscript) is the local fluid velocity. From experiments it is known that the typical density of a dilute aqueous electrolyte $\rho_m \simeq 1$ kg L^{-1} barely varies, at constant temperature and low salt concentration. As mass is generally also conserved $S_{\rho_m} = 0$ the continuity equation for the flow of mass $\partial_t \rho_m = -\nabla \cdot \rho_m \mathbf{u}$ simplifies to

$$\nabla \cdot \mathbf{u} = 0, \tag{1.5}$$

for an incompressible fluid with constant density.

Momentum transport Considering momentum conservation in electrolytes will result in richer physics. Not only can momentum be added and extracted but it is also transported by two distinct mechanisms: advection and diffusion. Advection of momentum occurs when movement of a fluid parcel carries away its own momentum: increasing the electrolyte velocity twofold hence increases momentum transport fourfold. Diffusion occurs when nearby water molecules with different velocities interact, thereby exchanging momentum. The rate of diffusive momentum transfer is proportional to the average velocity difference between two fluid elements $-\nu\nabla\mathbf{u}$ where ν is the diffusion constant of (transverse) momentum, also known as the kinematic viscosity, which in water $\simeq 1$ mm^2 s^{-1}. Considering both diffusive and advective transport the continuity equation for the momentum density reads $\partial_t\mathbf{p} = \mathbf{S}_\mathbf{p} - \nabla\cdot(\mathbf{p}\otimes\mathbf{v}_\mathbf{p}) = \mathbf{F} - \rho_\mathrm{m}\nabla\cdot(\mathbf{u}\otimes\mathbf{u} - \nu\nabla\mathbf{u})$, where $\mathbf{F}$ is an external force density acting as a momentum source, which after some algebra reads

$$\rho_\mathrm{m}\left(\partial_t\mathbf{u} + \mathbf{u}\cdot\nabla\mathbf{u} - \nu\nabla^2\mathbf{u}\right) = \mathbf{F}, \tag{1.6}$$

which is the famous Navier-Stokes equation. Whether diffusive or advective momentum-transport dominates is quantified by the Reynolds number Re$= uL/\nu$, with L a typical length-scale over which the flow occurs. Flowing water in everyday life moving over more than a millimeter in a second has Re$\gg 1$, and here momentum transport is dominated by advection. In this thesis, however, we consider fluid flows over micrometers where Re$\ll 1$ and hence the advective term $\mathbf{u}\cdot\nabla\mathbf{u}$ can be neglected. Furthermore, the momentum source $\mathbf{F}$ in this thesis consists of merely two components (i) the normal stress, equal to the pressure gradient $-\nabla P$, and (ii) an external electric field $-\nabla\psi$ acting on a charge density ρ_e within the fluid. This allows us to reduce the Navier-Stokes equation to the following (purely diffusive) Stokes equation

$$\rho_\mathrm{m}\partial_t\mathbf{u} = \eta\nabla^2\mathbf{u} - \rho_\mathrm{e}\nabla\psi - \nabla P, \tag{1.7}$$

with $\eta = \nu\rho_\mathrm{m}$ the dynamic (shear) viscosity. Together with Eq. (1.5) the Stokes Eq. (1.7) will be used to describe flow everywhere in this thesis. Typically flow in the low-Reynolds regime is much more well-behaved than flow in the high-Reynolds regime where the non-linear advection term $\mathbf{u}\cdot\nabla\mathbf{u}$ in Eq. (1.6) allows for chaotic and turbulent flows beyond Re $\simeq 10^3$, introducing a variety of complications that are often undesirable in experiments and applications. However, turbulence is also responsible for mixing of fluids at macroscopic scales. The lack of turbulence at micrometer-scales makes the mixing of fluids very difficult.

1.2.4 Diffusion, conduction and advection of ions

Much of this thesis will be focused on the transport of ions over micrometer lengths and in this section we consider how ions are transported by three separate

transport mechanisms: advection, conduction and diffusion. During the derivation we highlight that in microfluidic experiments advection, conduction and diffusion of ions all have comparable velocities. The balance and interplay of these transport mechanisms is key to understanding the experiments in this thesis.

Advection and conduction Ions in the electrolyte not only move with the surrounding fluid at a velocity $\mathbf{u}$ but can also undergo conductive and diffusive transport on their own. The velocity $\mathbf{v}$ of a single ion within the fluid is given by the Langevin equation

$$m\frac{\mathrm{d}\mathbf{v}_{\pm}(t)}{\mathrm{d}t} = -m\xi(\mathbf{v}_{\pm}(t)-\mathbf{u}) \mp e\nabla\psi + \mathbf{f}(t), \tag{1.8}$$

where m is the mass of the ion and ξ is the friction coefficient for a single spherical particle as derived by Stokes divided by the mass, $\xi = (6\pi\eta a)/m$ such that ξ^{-1} has dimensions of time. The hydrodynamic radius $a \simeq 0.1$ nm for ions in water, and counter-intuitively the hydrodynamic radius is inversely proportional to the ionic radius [15]. When the random thermal force vanishes, $\mathbf{f}(t) \simeq 0$, the terminal velocity of an ion

$$\mathbf{v}_{\pm} = \mp e\nabla\psi(m\xi)^{-1} + \mathbf{u} \quad \text{if} \quad t \gg \xi^{-1} \tag{1.9}$$

will be reached at a characteristic time $\xi^{-1} \simeq 10$ fs, comparable to the time between atomic collisions. Any excess momentum injected into the ion by the external field $\nabla\psi$ will have diffused into the fluid over this timescale, driving flow as discussed in the derivation of Eq. (1.7). For typical electric fields in this thesis $\simeq 1$ MV/m (for voltage drops of 1 V over 1μm) we find typical terminal velocities of 1 mm/s, comparable to the fluid velocity and resulting in a typical residence time of 1 ms for an ion in a micrometer channel.

Diffusion Ions dispersed in fluids do not only undergo steady-state forces by external fields, but also experience random thermal forces $\mathbf{f}(t)$ due to solvent molecules bumping into the ion by thermal motion. This thermal force is well approximated by random, uncorrelated, white noise which has no preferred direction and hence an expectation value $\langle\mathbf{f}(t)\rangle = \mathbf{0}$ but a non-zero mean square amplitude $\langle f_i(s)f_j(s')\rangle = (2mk_{\mathrm{B}}T\xi)\delta_{ij}\delta(s-s')$, with δ_{ij} the Kronecker-delta [7]. We aim to find the transport induced by this random forcing, and we start by substituting the random force into the Langevin Eq. (1.8) for vanishing external fields $\nabla\psi \simeq 0$ and obtain the velocity correlation $\langle\mathbf{v}(t)\cdot\mathbf{v}(t')\rangle = 3\exp(-\xi|t-t'|)k_{\mathrm{B}}T/m$, from which we directly observe that the average thermal-energy of an ion $(m/2)\langle\mathbf{v}(0)\cdot\mathbf{v}(0)\rangle = 3k_{\mathrm{B}}T/2$, as required by equipartition of energy, thereby showing the amplitude $(2mk_{\mathrm{B}}T\xi)$ of the noise term $\langle f_i(s)f_j(s')\rangle$ was chosen correctly. The mean-square

velocity can be converted to a mean-square displacement $\langle|\mathbf{R}(t)-\mathbf{R}(0)|^2\rangle$ by integration

$$\langle|\mathbf{R}(t)-\mathbf{R}(0)|^2\rangle = \int_0^t \int_0^t \mathrm{d}s\,\mathrm{d}s' \langle \mathbf{v}(s)\cdot\mathbf{v}(s')\rangle \simeq 6Dt \quad \text{if} \quad t \gg \xi^{-1}, \tag{1.10}$$

where we defined the diffusion constant $D = k_\mathrm{B}T/(m\xi)$ which is typically on the order of $\mu\mathrm{m}^2\ \mathrm{ms}^{-1}$ for ions in water.

From Eq. (1.10) it can be seen that the time it takes to travel a given length L grows as L^2/D and for macroscopic lengths $L \geq 1$ mm diffusive transport is very inefficient and takes more than 20 minutes. However, on micrometer length scales the diffusive transport time $L^2/D \simeq 1$ ms is comparable to both advective transport time $L/u \simeq 1$ ms, and conductive transport time $e\nabla\psi L/(m\xi) \simeq 1$ ms for typical electric fields of $-\nabla\psi \simeq 1$ MV/m. It is this delicate balance of diffusion, advection, and conduction that lead to rich physics in microfluidics. The balance of diffusion and advection is described by the Peclet number Pe=uL/D, reminiscent of the Reynolds number Re=uL/ν. While the Reynolds is often small at micrometer length scales, as in water the ratio of momentum to ionic diffusion is large $\nu/D \simeq 10^3$ the micrometer systems considered in this thesis have large Pe$\simeq 1$ but small Reynolds number Re$\ll 1$. Specifically the transition from diffusion (Pe$\ll 1$)- to flow (Pe$\gg 1$)- dominated ion-transport is key to much of the interesting physics observed in Chapter 2, 4 and 5. Furthermore, in Chapter 5 we introduce the ratio of the conductive and advective (electro-osmotic) transport rates $w = eD\eta/(k_\mathrm{B}T\varepsilon|\psi_0|)$ which is dimensionless and depends only on the surface potential ψ_0 and electrolyte properties: in water typically $w \in [1-10]$ for $|\psi_0| \in [0.1-0.01]$ V.

To find an explicit equation of motion for diffusive transport we calculate the probability $p(\mathbf{R},t)$ of finding a particle at location $\mathbf{R}$ at time t from its initial position $\mathbf{0}$. While the mean displacement by random thermal motion is zero over N timesteps

$$\langle\mathbf{R}\rangle = N^{-1}\sum_{i=0}^{N}\int_{t_i}^{t_{i+1}} \mathrm{d}s\ \mathbf{v}_i(s) \simeq 0 \quad \text{if} \quad N\to\infty, \tag{1.11}$$

as we have seen from Eq. (1.10) the mean-square displacement will increase with time due to random thermal collisions. This probability distribution $p(\mathbf{R},t)$ can be calculated straightforwardly by observing that Eq. (1.11) describes the summation of independent, statistically identical, displacements which per the central limit theorem [7] will result in a Gaussian distribution which is uniquely defined by (i) normalization and (ii) the variance $\langle|\mathbf{R}(t)-\mathbf{R}(0)|^2\rangle$ as already calculated above, resulting in $p(\mathbf{R},t) = (12\pi Dt)^{-3/2}\exp(-|\mathbf{R}|^2/(12Dt))$. As announced this probability profile is peaked around the origin, but spreads out over time due to the random thermal motion of the ions. The spread of this probability distribution

obeys

$$\partial_t p(\mathbf{R},t) = D\nabla^2 p(\mathbf{R},t), \tag{1.12}$$

which is aptly named the diffusion equation as it is the equation of motion for a diffusive particle.

Diffusion-conduction-advection Having described the motion of a single particle in an external field (Eq. (1.9)) as well as by thermal motion (Eq. (1.12)) we now combine these results after first converting the single-particle velocities into many-particle densities $\rho_\pm = pN_\pm/V$ and fluxes $\mathbf{j}_\pm = \rho_\pm \mathbf{v}_\pm$, with $N_\pm$ the number of negative and positive ions within an arbitrary small volume V. While this conversion may seem innocent, this step actually introduces a variety of errors as the single-particle equation of motion implicitly neglect any ion-ion correlations present for a collection of ions. Such ion-ion correlations invalidate both the presented derivation of the diffusion equation and the diffusion constant. The deviations stemming from these correlations become very relevant at high concentrations $\rho_\pm \gtrsim 1$ M where 1% of the electrolyte consists of ions and transport qualitatively differs from the dilute transport described in this thesis. Without further comment we hereby refer the reader to several theories that may be more appropriate in this dense electrolyte regime: Ref. [16, 17].

Continuing in the dilute regime and focusing on a 1 : 1 electrolyte of monovalent ions with equal diffusion constants $D_\pm = D$, we substitute Eq. (1.9) and Eq. (1.12) in the continuity equation $\partial_t \rho_\pm = -\nabla\cdot(\mathbf{v}_\pm \rho_\pm)$ to obtain the diffusion-conduction-advection equation

$$\partial_t \rho_\pm = D\left(\nabla^2\rho_\pm \pm \nabla\cdot(\rho_\pm \frac{e\nabla\psi}{k_\mathrm{B}T})\right) - \nabla\cdot(\rho_\pm \mathbf{u}), \tag{1.13}$$

also known as the Fokker-Planck or Smoluchowski equation. Again writing this equation as a continuity equation $\partial_t\rho_\pm = -\nabla\cdot\mathbf{j}_\pm$ we find for the flux

$$\mathbf{j}_\pm = -D(\nabla\rho_\pm \pm \rho_\pm \frac{e\nabla\psi}{k_\mathrm{B}T}) + \rho_\pm \mathbf{u}, \tag{1.14}$$

which is known as the Nernst-Planck equation. Here the first diffusive term reproduces Fick's law, the second term represents Ohmic conduction, and the third term Stokesian advection. In principle Eq. (1.13) is a linear differential equation which can be solved analytically with the proper boundary conditions provided $\nabla\psi$ and $\mathbf{u}$ are fixed. However in the next section we will see that coupling this equation to the Poisson and Stokes Eqs. (1.3)-(1.7) introduces non-linearities and hence complications.

1.2.5 Putting everything together

Combining the Poisson, incompressibility, Stokes, and diffusion-conduction-advection, Eqs. (1.3,1.5,1.7,1.13) resulting from the continuity equation for momentum, mass and ions a closed set of equations is found

$$\nabla^2\psi = -\frac{e}{\varepsilon}\rho_\mathrm{e}, \tag{1.15}$$

$$\nabla\cdot\mathbf{u} = 0, \tag{1.16}$$

$$\rho_\mathrm{m}\partial_t\mathbf{u} = \eta\nabla^2\mathbf{u} - \rho_\mathrm{e}\nabla\psi - \nabla P, \tag{1.17}$$

$$\partial_t\rho_\pm = D\left(\nabla^2\rho_\pm \pm \nabla\cdot(\rho_\pm\frac{e\nabla\psi}{k_\mathrm{B}T})\right) - \nabla\cdot(\rho_\pm\mathbf{u}), \tag{1.18}$$

that are known as the Poisson-Nernst-Planck-Stokes equations. Each individual equation in this set describes relatively plain physics and constitutes a linear, second order, differential equation. However by coupling these equations together a non-linear feedback emerges: as momentum transports ions, it changes the ion distributions, which again changes how much momentum is injected into the fluid. While such coupling makes the PNPS equations interesting, simultaneously any rigorous mathematical treatment becomes difficult due to the non-linearities emerging from the coupling.

Not-so-linear A standard approach in dealing with such non-linear equations is linearizing the differential equations around a homogeneous solution with $\nabla\psi = \nabla\rho = \nabla P = 0$, and afterwards solving for the lowest order term for small gradients. However by this approach we immediately lose the coupling that we wish to capture [18], such as the coupling of fluid flow to electric field or the coupling between electric current and pressure. The linear-response referred to in the title is thus explicitly not the expansion of the PNPS equations to lowest order.

Instead we study transport near thermodynamic equilibrium, such that the ion densities $\rho_\pm$ remain near their equilibrium values $\rho_{\pm,\mathrm{eq}}$, as described by Poisson-Boltzmann theory in Section 1.3.2, for which together with the equilibrium pressure and electric field all fluxes vanish $\mathbf{u} = \mathbf{j}_\pm = 0$ and $\partial_t\rho_\pm = 0$. For a non-equilibrium electric field and pressure the Stokes equation is then a differential equation linear in $\nabla\psi$ and ∇P. Substituting this flow in the Nernst-Planck Eq. (1.14) we find that the ion fluxes $\mathbf{j}_\pm$ are likewise linear in pressure and voltage. As flow remains coupled to voltage and ion fluxes remain coupled to pressure this approach qualitatively differs from an expansion around a homogeneous state, yet still results in fluxes linear in ∇P and $\nabla\psi$. No explicit linearization is performed around equilibrium, instead this approach assumes that combining equilibrium densities $\rho_{\pm,\mathrm{eq}}$ with non-equilibrium fields ∇P and $\nabla\psi$ results in valid, self-consistent, solutions obeying the continuity Eq. (1.1). In Section 1.3 we will find that this

assumption is valid for straight, non-reactive channels, and for this system transport is indeed linear. However in later Chapters we show that this assumption is no longer valid when the channel radius $R(x)$ varies laterally, or when the non-reactive channel is replaced by a dissolving channel. For these systems the ion densities vary with pressure and voltage, and hence transport becomes non-linear.

1.3 Fluid and charge transport through a pipe

In this third section of the introduction we use the equations of motion (1.15)-(1.18) derived in the last section to solve for the transport of charge and ions through a, micrometer, non-reacting, charged pipe. First we propose a set of appropriate (standard) boundary conditions for Eqs. (1.15)-(1.18) and then we solve for the ion profiles $\rho_{\pm}(\mathbf{r})$ within the charged pipe in thermodynamic equilibrium where all fluxes vanish $\mathbf{u} = \mathbf{j} = \mathbf{0}$, resulting in the so-called Poisson-Boltzmann solutions. We then solve the PNPS Eqs. (1.15)-(1.18) to describe transport of charge and fluid through a pipe, and find that transport resulting from the non-linear equations of motion is linear in both pressure and voltage. In the rest of thesis we find that this linearity is fragile to any change in the standard boundary conditions.

As depicted in Fig. 1.3, we consider a pipe with radius R and length L such that $L \gg R$ in cylindrical (x, r, θ) coordinates with $x \in [0, L]$ and $r \in [0, R]$, with the system being rotationally (θ) invariant such that the system is fully characterized in two-dimensional (x, r) coordinates. In the next subsection we discuss the forces ΔP and $\Delta\psi$ driving transport, while in the section thereafter we consider the ionic layer of thickness λ_{D} (Debye length) screening the surface charge $e\sigma$ on the channel wall.

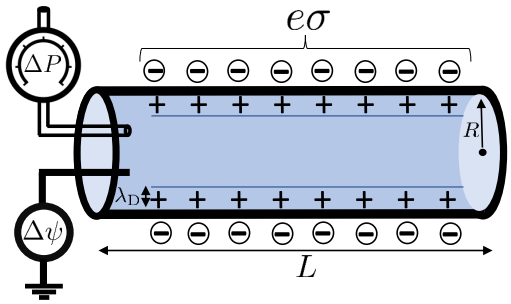

Figure 1.1: Schematic of the cylindrical channel of length L and radius R considered in Section 1.3. The channel wall carries a surface charge density $e\sigma$, attracting counter-ions and repelling co-ions, thereby forming a layer of length λ_{D} screening the surface charge. A pressure and potential difference, ΔP and $\Delta\psi$ respectively, are applied from $x = 0$ (left) to $x = L$ (right).

1.3.1 Boundary conditions

The governing PNPS Eqs. (1.15)-(1.18) describe most experiments involving dilute electrolytes reasonably well, but to model an experiment a set of representative boundary conditions must be chosen. This is actually the most crucial step in modelling any experiment, and as such we will carefully present the procedure by which boundary conditions are chosen.

Potential difference As Eqs. (1.15)-(1.18) constitute four second-order differential equations, we need eight boundary conditions. Four of these boundary conditions will be at the channel ends $(0,r)$ and (L,r) setting the thermodynamic potentials of the two reservoirs connected to the channel: the pressure P, electric potential ψ, and chemical potential $\mu_\pm - \mu_{0,\pm} = k_\mathrm{B}T\log(\rho_\pm/\rho_{0,\pm})$ of each ion which is proportional to their concentration, with $\rho_{0,\pm}$ an arbitrary reference concentration. For transport the difference in the potentials is the most relevant, and therefore we write the boundary conditions as

$$P(0,r) - P(L,r) = \Delta P, \tag{1.19}$$

$$\psi(0,r) - \psi(L,r) = \Delta\psi, \tag{1.20}$$

$$\rho_\pm(0,r) - \rho_\pm(L,r) = 0, \tag{1.21}$$

with reference potentials $P(L,r) = P_0$, $\psi(L,r) = 0$, and concentration $\rho_\pm(L,r) = \rho_\mathrm{b}$. Not only does the concentration ρ_b set the chemical potential difference, but it will also be key to the transport properties of the channel. By setting the boundary conditions at the channel edges, we implicitly assume that the potential at the edge of the channel immediately decays to the value deep within the connected reservoir: this is a good assumption when the aspect ratio is large, $L \gg R$, however in Chapter 5 we consider the case where this assumption is not met.

Surface transport properties The remaining three boundary conditions are set on the channel-electrolyte boundary at (x,R). The choice of boundary condition is determined by the mechanism by which ions, momentum, and fluid are exchanged between the solid channel wall and electrolyte. Momentum transfer from the electrolyte to the solid is the subject of active research [19, 20], but for channels with a radius larger than the slip length $\simeq 10$ nm it is appropriate to assume collisions between wall and solvent are perfectly inelastic setting $u_x(x,R) = 0$, known as the no-slip boundary condition. As everywhere in this thesis the solid surface is assumed to be impermeable to solvent, the total fluid velocity at the boundary is set $\mathbf{u}(x,R) = 0$. The boundary condition for the electric field at the surface is determined by Gauss' law (Eq. (1.4)), as described in Section 1.2.2. Finally, while the impermeability of the solid wall for ions $\mathbf{j}_\pm(x,R)$ may seem trivial,

it is actually violated by chemical reactions which can extract ions from the surface. When the channel is non-reactive, the boundary conditions on the channel wall read

$$\mathbf{u}(x,R) = \mathbf{0}, \tag{1.22}$$

$$\hat{\mathbf{n}} \cdot \nabla \psi = -e\sigma/\varepsilon, \tag{1.23}$$

$$\hat{\mathbf{n}} \cdot \mathbf{j}_{\pm} = 0, \tag{1.24}$$

where $\hat{\mathbf{n}}$ is the inward pointing surface normal. For a fixed and given surface charge $e\sigma$, the PNPS Eqs. (1.15)-(1.18) constitutes a closed set of equations with the boundary conditions Eq. (1.19)-(1.23). For straight channels this set of equations can be solved analytically and it will be convenient to first solve them for vanishing pressure and potential drop $\Delta P = \Delta\psi \simeq 0$ where similarly all flow and fluxes vanish $\mathbf{u} = \mathbf{j}_{\pm} \simeq \mathbf{0}$. Thereafter we can use these results to calculate transport for finite ΔP and $\Delta\psi$. When the flow and fluxes vanish the system is effectively in thermodynamic equilibrium, which is described by Poisson-Boltzmann theory as described in Section 1.3.2.

1.3.2 Note on surface chemistry

In this thesis we change the boundary conditions Eqs. (1.22)-(1.24) in Chapters 2 and 3 to more realistically model the surface charge $e\sigma$ at the solid-electrolyte interface. Such surface chemistry can be dominated by ions present at trace amounts: in Chapter 2 the charge is determined by fluoride present at a $1:1000$ ratio to chloride. This sensitivity requires distinguishing ions by chemical species rather than solely by their charge. In this thesis we make the distinction between two kinds of surface reactions: charging reactions where the net charge of the surface changes, and charge neutral dissolution where neutral sub-units detach from the surface.

Charging An example of a charging reaction is

$$\mathrm{CaF}_{2(\mathrm{s})} \underset{k_{\mathrm{ads}}\rho_{\mathrm{F}}}{\overset{k_{\mathrm{des}}}{\rightleftharpoons}} \mathrm{CaF}^{+}_{(\mathrm{s})} + \mathrm{F}^{-}_{(\mathrm{aq})}, \tag{1.25}$$

where an ion, in this case fluoride, desorbs from a solid (calcium fluoride) surface (s), to the aqueous electrolyte (aq) at a constant rate k_{des}. The rate of the reverse process, where an ion adsorbs onto the surface from the electrolyte, occurs at a rate $k_{\mathrm{ads}}\rho_{\mathrm{F}}$ with ρ_{F} the density of fluoride ions at the solid surface $r = R$. The rate $\partial_t\sigma$ by which the surface charge density changes does not only depend on ρ_{F} but also on σ: a reaction can only occur when a charged site and fluoride ion meet, and this probability is proportional to $\rho_{\mathrm{F}}\sigma$. Conversely, when the probability of a single uncharged surface site releasing an ion is constant, the total rate of desorption is proportional to the total number of uncharged sites $\Gamma - \sigma$ with Γ the saturation

charge density. From these considerations we can directly write down the kinetic Langmuir equation

$$\partial_t \sigma = k_{\text{des}}(\Gamma - \sigma) - k_{\text{ads}} \rho_{\text{F}} \sigma, \tag{1.26}$$

and the corresponding fluoride flux at the wall becomes $\hat{\mathbf{n}} \cdot \mathbf{j}_{\text{F}} = \partial_t \sigma$. In steady-state $\partial_t \sigma = 0$ and charging reactions can never be a source of ions in this case. Solving for $\partial_t \sigma = 0$ we find the equilibrium surface charge density $\sigma_{\text{eq}} = \Gamma/(1 + (k_{\text{ads}} \rho_{\text{F}} / k_{\text{des}}))$, known as the Langmuir isotherm.

Dissolution An example of a dissolution reaction is

$$\text{CaF}_{2(\text{s})} \underset{k_{\text{prec}} \rho_{\text{Ca}} \rho_{\text{F}}^2}{\overset{k_{\text{dis}}}{\rightleftharpoons}} \text{Ca}^{2+}_{(\text{aq})} + 2\text{F}^{-}_{(\text{aq})}, \tag{1.27}$$

where an entire charge neutral calcium fluoride unit dissolves with rate k_{dis} and precipitates at rate $k_{\text{prec}} \rho_{\text{Ca}} \rho_{\text{F}}^2$. From similar considerations as for charging, we can write down the rate of dissolution

$$2\hat{\mathbf{n}} \cdot \mathbf{j}_{\text{F}} = \hat{\mathbf{n}} \cdot \mathbf{j}_{\text{Ca}} = k_{\text{dis}} - k_{\text{prec}} \rho_{\text{F}}^2 \rho_{\text{Ca}}. \tag{1.28}$$

When neglecting the change in channel radius due to dissolution, such a reaction can form a steady-state source of ions, thereby invalidating Eq. (1.24). In Chapter 2 we will consider what happens when charging and dissolution reactions are coupled.

While such simple treatment of chemical reactions already leads to rich physics, in reality reactions (1.25)-(1.27) are highly idealized: not only do multiple reactions occur concurrently on real surfaces, the rates k_{des}, k_{ads}, k_{dis} and k_{ads} also depend on σ and all local densities ρ_i. An extensive literature disentangling surface chemistry exists for which we recommend Ref. [12, 13] as introductions and Ref. [21] as reference work.

1.3.3 Equilibrium theory

In this section we discuss the equilibrium space charge density $e\rho_{\text{e}} = e(\rho_+ - \rho_-)$ near the channel wall screening the surface charge $e\sigma$. The theory describing this equilibrium distribution is known as Poisson-Boltzmann theory [10]. The equilibrium charge density, known as the electric double layer (EDL), is responsible for coupling the Poisson, Stokes and Nernst-Planck equations together and it is this equilibrium space charge density that couples current to pressure and flow to voltage, as discussed at the end of Section 1.2.5. Furthermore, when the surface charge density is large not only does the charge density vary radially but also the total salt density $\rho_{\text{s}} = \rho_+ + \rho_-$ increases. This change in salt density modifies the channel conductance as we will see in Chapter 4 and 5.

Poisson-Boltzmann theory Before calculating the fluxes through the cylindrical channel, we have to find the ion profiles $\rho_\pm$ in thermodynamic equilibrium where the fluid velocity $\mathbf{u} = \mathbf{0}$ and ion fluxes $\mathbf{j}_\pm = \mathbf{0}$ all vanish. From the PNPS equations we find that in this case the ion density obeys the Boltzmann distribution $\rho_\pm(\mathbf{r}) = \rho_\mathrm{b} \exp(\mp e\psi(\mathbf{r})/k_\mathrm{B}T)$ fixing the concentration when the electric potential $\psi(\mathbf{r})$ is known. Writing the space charge density $\rho_\mathrm{e} = \rho_+ - \rho_- = \rho_\mathrm{b} \sinh(e\psi/k_\mathrm{B}T)$ we obtain the Poisson-Boltzmann equation

$$\frac{e\nabla^2\psi}{k_\mathrm{B}T} = \lambda_\mathrm{D}^{-2} \sinh\left(\frac{e\psi(\mathbf{r})}{k_\mathrm{B}T}\right), \tag{1.29}$$

from Eq. (1.3) which in other fields is better known as the sinh-Gordon equation [22]. Here the Debye screening length is defined as

$$\lambda_\mathrm{D} = (8\pi\lambda_\mathrm{B}\rho_\mathrm{b})^{-1/2} \tag{1.30}$$

and the Bjerrum length $\lambda_\mathrm{B} = e^2/(4\pi\varepsilon k_\mathrm{B}T)$ is the length at which two ions have an electrostatic energy of $k_\mathrm{B}T$, which in water $\simeq 0.7$ nm. The Debye screening length results from the competition between electrostatic attraction pulling screening-ions to the charged surface, repulsion of co-ions, and random thermal forces (Eq. (1.10) dispersing the ions. In the dilute range where the PNPS Eqs. (1.15)-(1.18) are valid, $\rho_\mathrm{b} \in [10^{-6} - 1]$ M, the Debye length varies between $\lambda_\mathrm{D} \in [10^3 - 1]$ nm and hence electrostatic attraction typically localizes counterions within a nanometer range of the charged surface. This layer is known as the electric double layer (EDL) and this equilibrium charge density in the fluid is key to all of the interesting physics in this thesis.

Gouy-Chapman equation While Eq. (1.29) is a non-linear differential equation, the potential-distribution can actually be solved for analytically when the channel curvature is smaller than the double-layer decay range $R \gg \lambda_\mathrm{D}$ in which case $(\partial_r^2\psi + \partial_r/r)\psi \simeq \partial_r^2\psi$ at the EDL near the channel wall. When integrating Eq. (1.29) once and evaluating the potential at $r = R$, substituting Gauss' law Eq. (1.4) we obtain the Gouy-Chapman, a.k.a. Grahame, equation [10] relating the surface charge $e\sigma$ to surface potential ψ_0

$$\frac{e\psi_0}{k_\mathrm{B}T} = 2\sinh^{-1}(2\pi\lambda_\mathrm{B}\lambda_\mathrm{D}\sigma). \tag{1.31}$$

Integrating the Poisson-Boltzmann equation once more we find an expression for the electric potential

$$\frac{e\psi(r)}{k_{\mathrm{B}}T} = 4\tanh^{-1}\left(\gamma\,\exp\left(\frac{r-R}{\lambda_{\mathrm{D}}}\right)\right) \simeq \tag{1.32}$$

$$\begin{cases} (e\psi_0/k_{\mathrm{B}}T)\,\exp\left(\frac{r-R}{\lambda_{\mathrm{D}}}\right) & \text{if} \quad e\psi_0 \ll k_{\mathrm{B}}T; \\ 4\tanh^{-1}\left(\exp\left(\frac{r-R}{\lambda_{\mathrm{D}}}\right)\right) & \text{if} \quad e\psi_0 \;>\; 4k_{\mathrm{B}}T, \end{cases} \tag{1.33}$$

with $\gamma = \tanh\left(e\psi_0/(4k_{\mathrm{B}}T)\right) \in [-1,1]$ quantifying whether the surface is "weakly charged" when $|\gamma| \ll 1$, in which case the Gouy-Chapman Eq. (1.31) becomes linear in the surface charge $e\psi_0/k_{\mathrm{B}}T \simeq 4\pi\lambda_{\mathrm{B}}\lambda_{\mathrm{D}}\sigma$ or "strongly charged", when $|\gamma| \simeq 1$, in which case the relation is logarithmic $e\psi_0/k_{\mathrm{B}}T \simeq 2\log(2\pi\lambda_{\mathrm{B}}\lambda_{\mathrm{D}}\sigma)$. In Chapter 3 we show that weakly and strongly charged surfaces exhibit qualitatively different reaction kinetics. While the equilibrium EDL always contains as much charge as need to screen the charged surface, $2\pi\int_0^R \mathrm{d}r r\rho_{\mathrm{e}}(r) = -(2\pi R)\sigma$, the amount of salt $\rho_{\mathrm{s}}(r) = \rho_+(r) + \rho_-(r)$ in the EDL depends strongly on the degree of charging as $2\pi\int_0^R \mathrm{d}r r(\rho_{\mathrm{s}}(r) - 2\rho_{\mathrm{b}}) = (2\pi R)\gamma\sigma$ [11], which is always positive. In this thesis we structurally neglect the contribution of salt adsorption to transport which is justified in the small EDL limit $\lambda_{\mathrm{D}} \ll R$ as long as the surface potential is not too large $\psi_0 \leq 4k_{\mathrm{B}}T/e \simeq 100$ mV. In Section 1.4 we derive an explicit range of validity for this assumption. Analytic expressions including salt adsorption are known [10, 11] but are somewhat cumbersome.

1.3.4 Transport matrix

Having fully characterized the equilibrium state of a cylindrical channel with surface charge $e\sigma$ in thermodynamic equilibrium, we can now explicitly calculate the transport of charge $e\mathbf{j}_{\mathrm{e}} = e(\mathbf{j}_+ - \mathbf{j}_-)$ and fluid $\mathbf{u}$. For straight, non-reactive, channels with the boundary conditions Eqs. (1.19)-(1.24) this derivation is straightforward. However, any small change in the boundary conditions (Eqs. (1.21)-(1.24)) makes such a calculation very difficult, as flow and flux driven by small ΔP and $\Delta\psi$ with equilibrium densities $\rho_\pm$ no longer satisfy the continuity equation (1.1), as discussed at the end of Section 1.2.5. When we encounter such problems we often turn to numerical (finite-element) calculations of the full PNPS Eqs. (1.15)-(1.18), looking for reasonable approximations that reduce the complexity of the transport problem.

Mobility matrix For a straight, non-reactive, cylindrical channel we will find that $\mathbf{u}(r)$ and charge flux $e\mathbf{j}_{\mathrm{e}}(r) = e(\mathbf{j}_+(r) - \mathbf{j}_-(r))$ are accurately described by the

linear relation

$$\begin{pmatrix} \hat{\mathbf{x}} \cdot \mathbf{u}(r) \\ \hat{\mathbf{x}} \cdot e\mathbf{j}_{\mathrm{e}}(r) \end{pmatrix} = \mathbb{M}(r) \begin{pmatrix} \Delta P \\ \Delta \psi \end{pmatrix}, \tag{1.34}$$

with $\hat{\mathbf{x}}$ the lateral normal vector. Our aim is to calculate the four components of the (linear) mobility matrix $\mathbb{M}_{11}$, $\mathbb{M}_{12}$, $\mathbb{M}_{21}$ and $\mathbb{M}_{22}$. To calculate these components we must first solve for the pressure $P(x,r)$ and potential profiles $\psi(x,r)$, which from the incompressibility Eq. (1.5) and the Poisson Eq. (1.3) are found to be divergence free, and hence obey the Laplace equation $\nabla^2 P = 0$ and $\nabla^2 \psi = 0$ as discussed in Section 1.2.2, when the charge density outside of the EDL vanishes $\rho_{\mathrm{e}} \simeq 0$. When the aspect ratio is large $L \gg R$ all radial gradients vanish and hence the divergence free electric field and pressure gradient are spatially constant, and for boundary conditions Eqs. (1.19)-(1.20) these gradients are given by

$$\partial_x \psi = -\frac{\Delta \psi}{L} \quad \text{and} \quad \partial_x P = -\frac{\Delta P}{L}. \tag{1.35}$$

Having obtained expressions for $\nabla\psi$ and ∇P in the PNPS equations, to obtain the fluidic-mobilities $\mathbb{M}_{11}(r)$ and $\mathbb{M}_{12}(r)$ we must now solve the Stokes equation for $\Delta\psi = 0$ in which case the Stokes equation reads $\eta \partial_x^2 u_x = \partial_x P$ and for $\Delta P = 0$ in which case it reads $\eta \partial_x^2 u_x = \rho_{\mathrm{e}} \partial_x \psi$. After integrating both of these differential equations twice, we obtain respectively the pressure and potential dependent flow which can be substituted in Eq. (1.14) to obtain the electric-mobilities $\mathbb{M}_{21}(r)$ and $\mathbb{M}_{22}(r)$ which are equal to $\rho_{\mathrm{e}}(r) u_x(r)$ with $\Delta\psi = 0$ and $\rho_{\mathrm{s}}(r)\partial_x\psi + \rho_{\mathrm{e}}(r) u_x(r)$ with $\Delta P = 0$. Collecting all our results we find that in the thin-EDL limit $\lambda_{\mathrm{D}} \ll R$ where we neglect salt-adsorption in the EDL (as described in Section 1.3.2 on Poisson-Boltzmann) the mobility matrix is given by

$$\begin{aligned} \mathbb{M}_{11} &= \frac{1}{4\eta L}(R^2 - r^2), & \mathbb{M}_{12} &= \frac{\varepsilon}{\eta L}(\psi(r) - \psi_0), \\ \mathbb{M}_{21} &= \frac{\varepsilon}{4\eta L \lambda_{\mathrm{D}}^2}(R^2 - r^2)\psi(r), & \mathbb{M}_{22} &= \frac{2\rho_{\mathrm{b}} e^2 D}{L k_{\mathrm{B}} T}. \end{aligned} \tag{1.36}$$

Here $\mathbb{M}_{11}(r)$ is a parabolic-flow profile known as Poiseuille flow, and $\mathbb{M}_{12}(r)$ has a constant mobility $-\varepsilon\psi_0/\eta$ outside of the EDL, representing an electro-osmotic plug flow. The electric mobility $\mathbb{M}_{21}(r)$ shows how the space-charge in the EDL gets carried away by pressure-driven Poiseuille flow, often named the streaming current, and finally $\mathbb{M}_{22}(r)$ is Ohmic conduction, which is radially constant as we have neglected both the advective current due to electro-osmotic flow and the salt adsorption in the EDL.

Transport matrix Up to this point the only use of the mobility matrix $\mathbb{M}(r)$ was to keep track of all fluxes of fluid and charge and this matrix $\mathbb{M}(r)$ has no

structure [23]. However, when we integrate the mobility matrix to obtain the total flux of fluid $Q = 2\pi\hat{\mathbf{x}} \cdot \int_0^R \mathrm{d}r r\, \mathbf{u}(r)$ and charge $I = 2e\pi\hat{\mathbf{x}} \cdot \int_0^R \mathrm{d}r r\, \mathbf{j}_\mathrm{e}(r)$ we obtain

$$\begin{pmatrix} Q \\ I \end{pmatrix} = \frac{\pi R^2}{L} \begin{pmatrix} \frac{R^2}{8\eta} & -\frac{\varepsilon\psi_0}{\eta} \\ -\frac{\varepsilon\psi_0}{\eta} & \frac{2\rho_\mathrm{b} De^2}{k_\mathrm{B}T} \end{pmatrix} \begin{pmatrix} \Delta P \\ \Delta\psi \end{pmatrix}, \tag{1.37}$$

where we observe that the linear response matrix $\mathbb{L} = 2\pi \int_0^R \mathrm{d}r r \mathbb{M}(r)$ is symmetric! This is not coincidental as it turns out there is a very strong connection between the transport matrix $\mathbb{L}$ and thermodynamics which guarantees that $\mathbb{L}$ both has positive eigenvalues (such that $\det(\mathbb{L}) > 0$) and is symmetric $\mathbb{L}_{ij} = \mathbb{L}_{ji}$, as first proposed in 1931 [3], popularized more than 10 years later [8] and afterwards extensively verified in experiments [9].

That the transport relations emerging from the PNPS equations, which at no point made a reference to thermodynamics, should obey limits set by thermodynamics is not only interesting but also useful; generalizations of the Onsager matrix $\mathbb{L}$ and mobility matrix $\mathbb{M}(r)$ can be used to describe transport in a variety of systems such as transport of heat and charge in graphene [24] and metals [3]. From this consideration, there may be an inkling of hope that interesting features of $\mathbb{L}$ and $\mathbb{M}(r)$ such as the not-so-linear Onsager matrix found in Chapter 4 might generalize to other systems.

1.4 Thermodynamic limitations on transport

In this fourth section we will treat the transport of heat and entropy due to charge and fluid transport from a, macroscopic, thermodynamic perspective. We will show that the temperature differences resulting from friction are indeed negligible as assumed in the derivation of the PNPS equations. Furthermore we will find that entropy transport and production places strong constraints on both the symmetry and the sign of the transport matrix. In the first section we will show that the eigenvalues and determinant of $\mathbb{L}$ in Eq. (1.37) must be positive, and in the second section we will show that $\mathbb{L}$ must be symmetric.

These derivations are notoriously subtle and we will neglect any complications due to temperature gradients, magnetic fields and tensorial conductance: in the first half of this section we work within the framework as presented by Mazur [25], while in the second section we closely follow the derivation as presented by Casimir [8]. We refer readers to these seminal publications for more general and rigorous treatments.

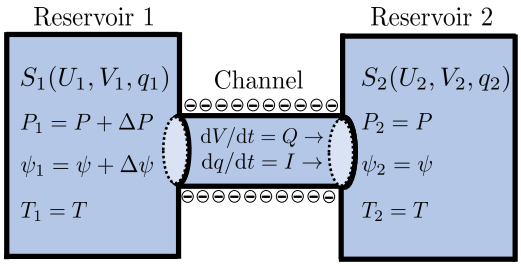

Figure 1.2: Schematic representation of a closed system at fixed energy consisting of two electrolyte reservoirs (1 and 2) and a charged channel connecting them. The two reservoirs respectively have entropy $S_i(U_i, V_i, q_i)$, with U_i the internal energy, V_i the fluid volume and q_i the total ionic charge. The final entropy of the closed system is $S \simeq S_1 + S_2$. In thermodynamic equilibrium the pressure P_i, electric potential ψ_i, and temperature T_i in the two reservoir are equal, but outside of equilibrium a small pressure difference $\Delta P = P_1 - P_2$ and $\Delta\psi = \psi_1 - \psi_2$ can exist. The two reservoirs are connected by a charged cylindrical channel allowing for exchange of fluid $\mathrm{d}V = -\mathrm{d}V_1 = \mathrm{d}V_2$ and charge $\mathrm{d}q = -\mathrm{d}q_1 = \mathrm{d}q_2$. The sign conventions of ΔP, $\Delta\psi$, $\mathrm{d}V$ and $\mathrm{d}q$ are chosen such that the fluid $Q = \mathrm{d}V/\mathrm{d}t$ and charge $I = \mathrm{d}q/\mathrm{d}t$ transfer rate are described by Eq. (1.37).

1.4.1 Transport matrix is positive

We consider a closed system, with fixed *system* volume $\tilde{V}$, consisting of two electrolyte reservoirs, labelled 1 and 2, and a channel with charged walls connecting them as depicted in Fig. 1.2. As the system is closed the total charge q, (incompressible) fluid volume V and energy U is conserved. From the extensivity of the entropy it follows that $S(U,V,q) \simeq S_1(U_1,V_1,q_1) + S_2(U_2,V_2,q_2)$ and this total entropy S should be maximal in equilibrium. Here S_i, U_i, V_i and q_i are the equilibrium entropy, energy, volume and charge in each respective reservoir and where we neglected the entropy of the channel.

Solvent number or fluid volume transport? We will consider a closed system where the change in *system* volume $\mathrm{d}\tilde{V}$ is strictly zero: instead our *fluid* volume flux $\mathrm{d}V = \nu_\mathrm{s}\mathrm{d}N_\mathrm{s}$ refers to the flux of solute molecules N_s for which the volume per particle ν_s is constant due to incompressibility. We then define the partial pressure $\mu_\mathrm{s}/\nu_\mathrm{s} = P_\mathrm{s}$, where μ_s is the solvent chemical potential, at a suitable reference potential $\mu_{0,\mathrm{s}}$. For a dilute electrolyte $P_\mathrm{s} \simeq P$ [11, 26] holds and then the well-known first law of thermodynamics $\mathrm{d}U = -P\mathrm{d}\tilde{V} + T\mathrm{d}S + \mu_\mathrm{s}\mathrm{d}N_\mathrm{s}$ can be rewritten as $\mathrm{d}U = +P\mathrm{d}V + T\mathrm{d}S$ when $\mathrm{d}\tilde{V} = 0$, since $\mu_\mathrm{s}\mathrm{d}N_\mathrm{s} = +P\mathrm{d}V$. Thus $-P\mathrm{d}\tilde{V}$ is replaced by $+p\mathrm{d}V$. While perhaps somewhat uncomfortable, this subtle distinction is of critical importance when considering the salt flux $\mathbf{j}_+ + \mathbf{j}_- = \mathbf{j}_\mathrm{s}$ as discussed in Refs. [11, 26, 27], to which we refer for further discussion. The underlying physics is that the pressure does not actually involve a compression of dense fluid, but rather the transport of fluid from high to low pressures.

Reversible entropy transport As in equilibrium the two reservoirs are in mechanical, diffusive, electrical and thermal equilibrium they must have equal pressure $P_1 - P_2 = \Delta P = 0$, potential $\psi_1 - \psi_2 = \Delta\psi = 0$ and temperature $T_1 - T_2 = \Delta T = 0$. When due to a fluctuation in equilibrium an infinitesimal amount of fluid $\mathrm{d}V$ or charge $\mathrm{d}q$ is *reversibly* exchanged from Reservoir 1 to Reservoir 2, entropy must be conserved and $\mathrm{d}S = \mathrm{d}S_1 + \mathrm{d}S_2$ must be zero. As the entropy change in a given reservoir i is given by

$$\mathrm{d}S_i = -(P_i/T)\mathrm{d}V_i - (\psi_i/T)\mathrm{d}q_i, \tag{1.38}$$

we find that an exchange of charge $\mathrm{d}q$ and fluid $\mathrm{d}V$ is only reversible $\mathrm{d}S_1 = -\mathrm{d}S_2$ when the two reservoirs are in equilibrium $\Delta P = \Delta\psi = \Delta T = 0$. For such a reversible exchange from Reservoir 1 to Reservoir 2 occurring at a steady-state rate $Q = \mathrm{d}V/\mathrm{d}t$ for fluid and $I = \mathrm{d}q/\mathrm{d}t$ for charge, the total reversible entropy transport then occurs at a rate

$$J_\mathrm{S} = -(P/T)Q - (\psi/T)I, \tag{1.39}$$

which is the current of entropy carried by fluid and charge as defined by Mazur [25]. This entropic current is divergence free in equilibrium where $\Delta P = \Delta\psi = 0$, as Q and I are by definition also divergence free in steady state. Hence per the continuity Eq. (1.1) no entropy can be generated by this reversible current J_S, in accordance with reversibility.

Irreversible entropy transport However when fluid, charge and entropy are transported outside of equilibrium for small $\Delta P \neq 0$ and $\Delta\psi \neq 0$, the non-equilibrium pressure $P(x)$ and $\psi(x)$ are given by Eq. (1.35) and the divergence of the entropic current $\partial_x J_\mathrm{S} \neq 0$: during this non-equilibrium transport entropy is created and is thus *irreversible*. The created entropy $\mathrm{d}S = \mathrm{d}S_1 + \mathrm{d}S_2$ for an irreversible exchange, at a pressure and potential difference ΔP and $\Delta\psi$ but at equal temperature T, can be calculated from Eq. (1.38) and reads $\mathrm{d}S = (\Delta P/T)\mathrm{d}V + (\Delta\psi/T)\mathrm{d}q$. Again writing the rate of exchange as Q and I, we find the rate of entropy creation $\sigma = \mathrm{d}S/\mathrm{d}t = Q(\Delta P/T) + I(\Delta\psi/T)$. This result matches both the result as derived by Mazur [28] and that obtained from taking the divergence of the entropic current Eq. (1.39) $\sigma = J_\mathrm{S}(0) - J_\mathrm{S}(L) = Q(\Delta P/T) + I(\Delta\psi/T)$. Substituting the obtained linear response relation Eq. (1.37) for I and Q we find that the rate of energy dissipation by non-equilibrium transport

$$T\sigma = \begin{pmatrix}\Delta P \\ \Delta\psi\end{pmatrix} \mathbb{L} \begin{pmatrix}\Delta P \\ \Delta\psi\end{pmatrix} \geq 0, \tag{1.40}$$

and as entropy production and energy dissipation must always be positive per the 2nd Law of Thermodynamics, the eigenvalues and hence determinant of $\mathbb{L}$ likewise must be positive.

Consequences of dissipation Using the rate of energy dissipation Eq. (1.40) we can support the approximation that T is constant everywhere in this thesis. The increase in temperature per second is at most $T\sigma/C\tilde{V}$, with the specific heat capacity $C \simeq 4.2$ J mL^{-1} K^{-1} and a reservoir volume $\tilde{V}$, for which we take $\tilde{V} = 1$ mL. For the largest current in this thesis $I = 0.1$ μA at $\Delta\psi = 0.5$ V (Chapter 5) the dissipation is 0.05μJ/s and hence this experiment must run for three years (10^8 s) to heat a 1 mL reservoir by 1 Kelvin. Similarly, for a pressure differential of 1 bar a fluid flux of $Q = 10^{-2}$ mL/s would also need three months to heat 1 mL by 1 Kelvin: in a channel with $R = 1\mu$m this requires an exceptionally large velocity of around 10 m/s. These estimates show that temperature gradients due to Joule heating and fluid friction can safely be neglected for single channels. However, these estimates crucially depend on comparing transport through micrometer channels to mL reservoir volumes. For membranes with pore densities of $> 10^6$ pores mm^{-2} Joule heating can be expected to be relevant.

We can also use the requirement $\det(\mathbb{L}) > 0$ to calculate an explicit range of validity for Eq. (1.37) as we find that $\det(\mathbb{L}) < 0$ when $(\lambda_D/R)(e\psi_0/k_BT) \geq (\lambda_B/18a)^{-1/2} \simeq 0.4$ (with a the ion radius). As a negative determinant is forbidden we have found an explicit limit for when the assumption of negligible salt-adsorption made in Eq. (1.37) fails; a limit which is already met at $R = 10\lambda_D$ and $\psi_0 \simeq 100$ mV. At this point surface terms present in $\mathbb{L}_{22}$ scaling as $(e\psi_0/k_BT)(\lambda_D/R)$ implicitly neglected during our derivation in Section 1.3 but derived in the SI of [11], and important in Chapter 5, have to be taken into account.

1.4.2 Transport matrix is symmetric

Here we we will show that the transport matrix is symmetric, which implies the reciprocity relations $\mathbb{L}_{ij} = \mathbb{L}_{ji}$. These reciprocity relations are very useful as it almost halves the number of transport coefficients that must be calculated. Furthermore they are a useful consistency check for both theory and experiments.

Magnitude of fluctuations As shown in the previous section, to first order the equilibrium entropy upon an infinitesimal exchange $S(U, V + \mathrm{d}V, q + \mathrm{d}q) \simeq S(U, V, q)$ is reversible. However, in thermodynamic equilibrium the total entropy S of an isolated system must be maximal, and hence for a larger exchange of fluid ΔV and charge Δq the expansion of entropy up to second order yields

$$S(V,q) \simeq S_0 - \frac{k_B}{2}\left(C_{11}\Delta V^2 + 2C_{12}\Delta V\Delta q + C_{22}\Delta q^2\right), \tag{1.41}$$

where following the notation of Casimir C_{ij} are second derivatives of the entropy with units such that S has units of entropy (J/K), and $C_{12} = C_{21}$. This ex-

pression for the entropy allows us to calculate the expectation value of thermodynamic variables $\langle Vq\rangle = \int \mathrm{d}V\mathrm{d}q(Vq\omega(V,q))/\int \mathrm{d}V\mathrm{d}q\omega(V,q)$ as the density-of-states $\omega(V,q) = \exp\left(k_\mathrm{B}^{-1}S(V,q)\right)$ per the Boltzmann equation. Using Eq. (1.41) we straightforwardly find that $\langle \Delta q\Delta V\rangle = \langle \Delta q\rangle = \langle \Delta V\rangle = 0$ as they should for electrical and mechanical equilibrium to hold. The less trivial correlations

$$\begin{aligned}\langle \Delta P\Delta V\rangle &= \langle \Delta\psi\Delta q\rangle = k_\mathrm{B}T,\\ \langle \Delta P\Delta q\rangle &= \langle \Delta\psi\Delta V\rangle = 0,\end{aligned} \tag{1.42}$$

are found when realizing that the so-called thermodynamic conjugate for ΔV is $\Delta p = T\partial S/\partial(\Delta V) = -k_\mathrm{B}T(C_{11}\Delta V + C_{12}\Delta q)$ and for Δq it is $\Delta\psi = T\partial S/\partial(\Delta q) = -k_\mathrm{B}T(C_{22}\Delta q + C_{12}\Delta V)$ [8]. Here the first line of Eq. (1.42) is expected from equipartition while the second line shows there are no correlations between pressure and charge nor between fluid volume and electric potential.

Time-correlation of fluctuations We can use the correlated fluctuations Eq. (1.42) to derive the symmetry of the Onsager matrix by considering how an average thermodynamic fluctuation decays. In equilibrium not only is the average fluctuation independent from the time of observation, $\langle \Delta V'\Delta q'\rangle = \langle \Delta V(\delta t)q(\delta t)\rangle$, (with δt a small timestep and following Casimir's notation $\Delta V' = \Delta V(t=0)$), but in equilibrium the average rate by which a fluctuation decays should be the same as its average rate of formation $\langle \Delta V'\Delta q(\delta t)\rangle = \langle \Delta V'\Delta q(-\delta t)\rangle$. This so-called time-reversal symmetry of fluctuations is key to the symmetry of $\mathbb{L}$. Using time-translation and -reversal symmetry we find that cross-correlations obey $\langle \Delta V'\Delta q(\delta t,\Delta V')\rangle = \langle \Delta q'\Delta V(\delta t,\Delta q')\rangle$ which after some algebra can be simplified to

$$\langle \Delta V'\partial_t q'\rangle = \langle \Delta q'\partial_t V'\rangle, \tag{1.43}$$

when δt is sufficiently short for $\Delta q(\delta t,\Delta V') \simeq \Delta q' - \delta t\partial_t q'$ to hold. Here $\Delta q(\delta t,\Delta V')$ denotes Δq at time δt after at $t=0$ the volume difference was ΔV. Now we explicitly assume that the linear-response Eq. (1.37) is valid and $\partial_t q' \simeq \mathbb{L}_{22}\Delta\psi' + \mathbb{L}_{21}\Delta P'$ and similarly $\partial_t V' \simeq \mathbb{L}_{12}\Delta\psi' + \mathbb{L}_{11}\Delta P'$ thereby making the connection between thermodynamic fluctuations to transport theory. Only when this approximation is valid the relation

$$\mathbb{L}_{12}\langle \Delta P'\Delta V'\rangle = \mathbb{L}_{21}\langle \Delta\psi'\Delta q'\rangle \tag{1.44}$$

holds. Now substituting Eq. (1.42) results in the desired relation $\mathbb{L}_{21} = \mathbb{L}_{12}$, which is the Onsager reciprocal relation for the 2×2 electrokinetic transport matrix.

Assumptions underlying reciprocity It is useful to reflect on the three ingredients essential to this derivations: (i) the quadratic approximation Eq. (1.41) for $S(V,q)$ necessary for the stability of thermodynamic equilibrium, (ii) time-reversal symmetry of fluctuations in equilibrium Eq. (1.43), and (iii) linearizing

the decay of a fluctuation Eq. (1.43) in ΔP and $\Delta\psi$ as to ensure its time decay is described by Eq. (1.37). This linearization in the third approximation is the reason $\mathbb{L}$ is named the linear-response matrix. Both Onsager [3] and Casimir [8] remarked that the validity of this linearization is justified on empirical rather than theoretical grounds. As we noted in Section 1.2, the validity of the linear response matrix itself only holds for the straight channel because linear transport satisfies the continuity Eq. (1.1).

In Chapter 2, 3, 4 and 5 we consider systems for which this assumption does not hold, and non-linear transport can already occur for small ΔP and $\Delta\psi$. For these systems non-linear transport can already occur when driving potentials are comparable to $k_{\mathrm{B}}T$, the characteristic energy of thermodynamic fluctuations. From this consideration the question naturally arises if the near-equilibrium, linear, transport relation Eq. (1.44) holds similarly for near-equilibrium, nonlinear, transport.

Chapter 2

Liquid flow reversibly creates a macroscopic surface charge gradient

Abstract

The charging and dissolution of mineral surfaces in contact with flowing liquids are ubiquitous in nature, as most minerals in water spontaneously acquire charge and dissolve. Mineral dissolution has been studied extensively under equilibrium conditions, even though non-equilibrium phenomena are pervasive and substantially affect the mineral-water interface. Recent experiments demonstrate that liquid flow along a calcium fluoride surface creates a reversible spatial charge gradient, with decreasing surface charge downstream of the flow. In this Chapter we show that the surface charge gradient can be quantitatively accounted for by a reaction-diffusion-advection model, revealing that the charge gradient results from a delicate interplay between diffusion, advection, dissolution, and desorption/ adsorption. The underlying mechanism is expected to be valid for a wide variety of systems, including groundwater flows in nature and microfluidic systems.

This Chapter is based on the following publication:

P. Ober, W.Q. Boon, M. Dijkstra, E.H.G. Backus, R. van Roij, & M. Bonn, (2021). *Liquid flow reversibly creates a macroscopic surface charge gradient*, Nature communications, 12(1), 1-11.

The experimental work therein was performed by P.O., E.H.G.B. and M.B. at the Max Planck Institute for Polymer Research in Mainz. There are paragraphs and figures that are taken or modified from the above-mentioned publication and its supporting information. The co-authors gave their permission for the reproduction. The author contributions to this publication are as follows:

P.O., E.H.G.B., and M.B. designed the experimental part of the research project and provided a qualitative interpretation of the experimental results. P.O. performed the experiments and analyzed the data. W.Q.B., M.D., and R.v.R. provided a quantitative interpretation of the experimental results. W.Q.B. performed the numerical and analytic calculations and generalized the findings. All authors discussed the results and wrote the manuscript. P.O. and W.Q.B. contributed equally.

2.1 Introduction

Reactions at the interface between a charged solid surface and a flowing fluid play a key role on macroscopic scales in geochemical cycles [29–32], as well as on microscopic scales in micro- and nanofluidic systems [33]. They are also central in technological applications in areas as diverse as froth flotation [34], electrophoresis [35], water desalination [36], soil remediation [37], and even dentistry [38]. Only a few years ago, LIS et al. [32] presented the first experimental evidence that the surface potential of mineral surfaces (silica and calcium fluoride) in contact with water changes substantially when liquid flow is applied. This observation implies that fluid flow can directly affect a chemical equilibrium. For the mineral fluorite (CaF_2) under acidic conditions, the change of the surface charge upon flow was argued to be due to the dilution of reactive ions partaking in the surface charging reaction [32]. This dilution is caused by the concentration difference between the fresh solution from the reservoir and that in the flow channel. The dilution changes the charging equilibrium and increases the surface charge. A similar explanation has also recently been given by XI et al. [39]. Even though the flow-induced disturbance of the charging equilibrium qualitatively explains several experimental features, there are also inconsistencies. For instance, the question remains how a concentration difference between the reservoir and channel is generated. The surface charging reaction itself cannot supply the excess ion concentration in the channel over the reservoir concentration, as the number of reactive ions on the surface is too small to support a steady flux of ions, especially over many flow cycles.

Therefore, a fully self-consistent quantitative model is missing. In fact, several different hypotheses have been put forward for the change of the v-SFG signal upon flow, for instance, a surface conduction model by WERKHOVEN et al. [40], which would lead to a surface charge gradient and a 1D model by LIAN et al. [39] that considers net dissolution as the driving force. Moreover, SCHAEFER et al. [41] concluded that a change in surface potential could be explained by a flow-induced change of the concentration of ions that screen the surface charge. A flow-dependent surface charge not only paves the way for novel electrokinetic effects [42], but it also has important consequences for the interpretation of zeta potential measurements. However, the mechanism by which the flow alters the surface charge is poorly understood as of yet [43].

Outline In this Chapter we theoretically model the flow-dependent surface potential recorded by our experimental collaborators, Patrick Ober, Ellen Backus and Mischa Bonn of the Max Planck Institute for Polymer Research in Mainz, who recorded v-SFG spectra at several positions in a channel with a length of 2.48 cm and a radius of 0.24 cm. The local changes in the surface potential upon

flow are tracked through the intensity of the OH-stretch band in vibrational Sum Frequency Generation (v-SFG) spectra. The v-SFG response is a measure of the electric field at the surface (see Supplementary Note of Ref.[44] for details) and is connected to the surface charge which in turn is directly related to the surface potential. These v-SFG experiments by our collaborators reveal that flow triggers an increase of surface charge at every position in a channel as can be seen in Fig. (2.1), which shows that the v-SFG response decreases monotonically along the channel length so that it is largest at the inlet and smallest at the outlet. Additionally, it was found that the surface charge variation is also a function of the flow rate. We refer the interested reader to the Appendix for a more elaborate description of the experiments. To explain these observations quantitatively, we need a model that combines microscopic surface chemistry and macroscopic processes such as advection and diffusion over the centimeter-scale experimental geometry. In the following section, we will introduce a self-consistent model that extends the model of LIS et al. [32] and describes not only the flow-dependent surface charge but also the dependency on flow rate and position.

2.2 Surface chemistry

Here we will briefly discuss the qualitative features of our model. We incorporate two reactions that take place at the CaF_2-water interface (i.e., the wall of the flow channel): (i) The surface charging reaction Eq. (2.1a) in which only F^- desorbs from the surface (with a rate k_{des}) to leave behind a positively charged CaF^+ unit on the surface, together with its back-reaction that involves F^- adsorption (with a characteristic rate k_{ads}). This reaction is responsible for the surface charging, and has been considered responsible for the flow-induced change of the surface charge in previous work [32]. However, as we show below, a second reaction is necessary to explain the experimental results: (ii) The dissolution reaction of Eq. (2.1b) in which a charge-neutral CaF_2 unit dissolves at a rate k_{dis} resulting in three dissolved ions,one Ca^{2+} and two F^-. These ions can also precipitate back onto the surface with a characteristic rate k_{prec}, thereby consuming ions and whether the surface is a sink of source of ions depends on the ratio of the dissolution and precipitation rates. The reactions are given by:

$$\text{Charging}: \qquad \mathrm{CaF_{2(s)}} \underset{k_{\mathrm{ads}}\rho_{\mathrm{F}}}{\overset{k_{\mathrm{des}}}{\rightleftharpoons}} \mathrm{CaF^+_{(s)}} + \mathrm{F^-_{(aq)}}; \tag{2.1a}$$

$$\text{Dissolution}: \qquad \mathrm{CaF_{2(s)}} \underset{k_{\mathrm{prec}}\rho_{\mathrm{F}}^3/2}{\overset{k_{\mathrm{dis}}}{\rightleftharpoons}} \mathrm{Ca^{2+}_{(aq)}} + 2\mathrm{F^-_{(aq)}}. \tag{2.1b}$$

Here ρ_{F} is the fluoride concentration at the surface. As both the charging and dissolution reactions have a fluoride in common these reactions are coupled. While LIS et al. [32] and XI et al. [45] only considered the charging reaction from

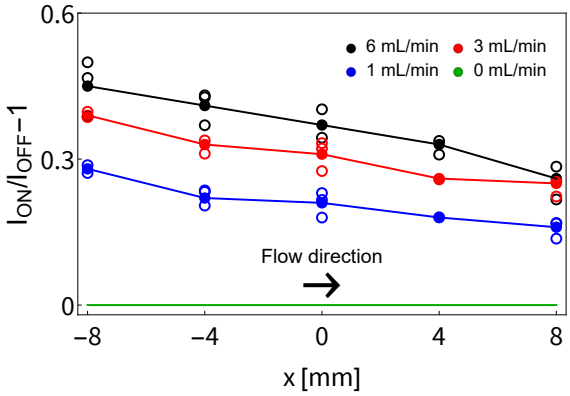

Figure 2.1: At different positions, the relative increase in the v-SFG intensity at the CaF_2-water interface is calculated based on averaged steady-state spectra under flow-on and flow-off conditions for four different flow rates. The solution used was a 1 mM NaCl solution in pH 3 HCl with an additional 1 μM NaF. The addition of a very low NaF concentration fixes the bulk fluoride concentration. Additional details on how these experiments are performed are presented in the Appendix. The x position is given as displacement from the center with x increasing along the flow direction as indicated by the arrow.

Eq. (2.1a) to qualitatively explain the flow-induced changes in v-SFG spectra, we argue that a consistent and quantitative description of the experimental results also requires to incorporate the dissolution as described by Eq. (2.1b). The charging reaction of Eq. (2.1a) alone could not serve as a steady-state source for fluoride ions. During the continuous dilution with fresh solution from the reservoir in the flow-on period, the surface charge and thus the v-SFG signal would have to keep increasing , which is not observed experimentally as a steady-state v-SFG signal is reached after about 5 minutes as shown in the Appendix.

Therefore, our model considers the CaF_2 surface not only as an adsorption-desorption site for fluoride anions but also as an ion source for charge-neutral dissolution and precipitation of Ca^{2+} and two F^- according to Eq. (2.1b). In fact, the dissolution reaction is not only a theoretical necessity but is also supported by the presence of Ca^{2+} cations in flow experiments with CaF_2 [32]. The appearance of a surface charge gradient upon flow as depicted in Fig. 2.1 can be explained when considering a flow-induced gradient in fluoride concentration along the mineral surface, as illustrated in Fig. 2.2(a). This gradient forms when the laminar flow transports dissolved fluoride anions along the interface, which leads to a build-up of fluoride ions at the outlet and a positive gradient in fluoride concentration in the flow direction. Moreover, because the solution flowing into the channel from the reservoir has a lower fluoride concentration, the fluoride ions are also diluted by the fresh solution, the more so the closer to the inlet. Thus, flow reversibly lowers the fluoride concentration everywhere in the channel, yet more so closer to

the inlet.

As the surface charge increases with lower fluoride concentration according to Eq. (2.1a), the surface charge becomes larger at positions closer to the inlet. This qualitatively explains the gradient of the increase in surface charge along the surface upon flow and thus in the v-SFG response. To quantitatively describe the change in surface charge upon flow we have to solve the full dissolution-diffusion-advection problem, which we do using numerical calculations.

2.3 Numerical model

We model the channel as a cylinder of length $2L$ and radius R, and introduce the radial and axial coordinate r and x, respectively. The charged and dissolving mineral surface of the channel is located at $r = R$ for $x \in [-H, H]$ (with $H < L$). The channel inlet and outlet are at $x = \pm L$, and $|x| \gg L$ denotes the interior of the two reservoirs in which we specify bulk concentrations and bulk pressure. The model geometry is depicted in Fig. 2.2(a). Throughout, we will assume azimuthal symmetry and consider water to be an incompressible fluid with viscosity η and dielectric constant ε at fixed room temperature T. We are interested in finding the areal density $\sigma(x)$ of charged surface groups on the mineral surface, the fluid velocity $\mathbf{u}(x,r)$ in the channel, and the concentrations $\rho_i(x,r)$ of ion species i=H^+, Cl^-, Na^+, Ca^{2+}, F^- of which, however, only calcium and fluoride will turn out to be relevant. The system is solved for steady-state without any explicit time-dependence. The fluid flow is driven by an imposed static pressure drop between the two reservoirs such that the pressure profile $P(x,r)$ is also to be determined.

Langmuir kinetics We model the surface chemistry in terms of the dynamic Langmuir equation

$$\partial_t \sigma = k_{\mathrm{des}}(\Gamma - \sigma) - k_{\mathrm{ads}} \rho_{\mathrm{F}}(x,R)\sigma = 0 \tag{2.2}$$

that accounts for the charging reaction of Eq. (2.1a). Here k_{des} and k_{ads} denote the desorption and adsorption rate constants of fluoride, respectively, and Γ denotes the surface density of chargeable groups. The surface charge density is thus denoted by $e\sigma(x)$, with e the proton charge. In the steady-state conditions of interest here, $\partial_t \sigma = 0$, we can solve the dynamic Langmuir Eq. (2.2) to obtain the Langmuir isotherm

$$\sigma(x) = \frac{\Gamma}{1 + \dfrac{k_{\mathrm{ads}}}{k_{\mathrm{des}}} \rho_{\mathrm{F}}(x,R)} \tag{2.3}$$

Note that when the surface charge is in steady-state, $\partial_t \sigma = 0$ the flux of calcium ions equals twice the flux of fluoride ions, $2J_{\mathrm{F}} = J_{\mathrm{Ca}}$ and hence in steady-state the

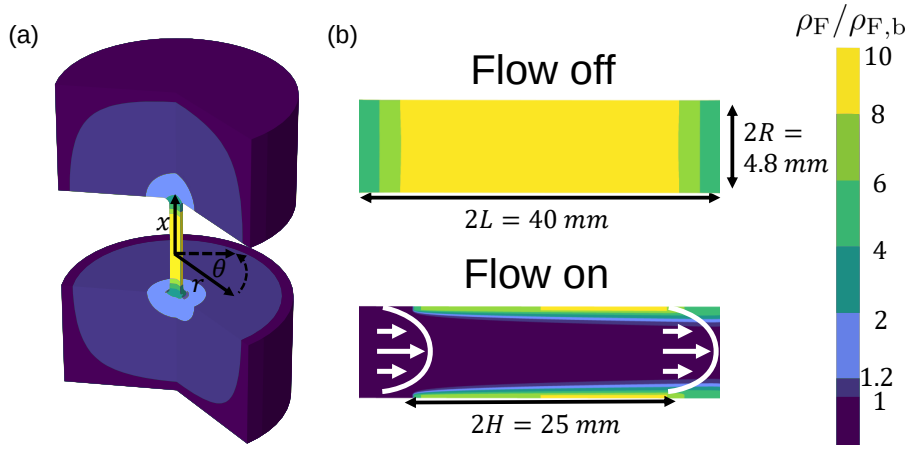

Figure 2.2: Channel geometry and numerical solutions to the reaction-diffusion-advection Eqs. (2.2)-2.6). Illustration of the flow channel as used for the numerical calculations in COMSOL with resulting concentration profiles. The center of the flow channel is at the origin $x = 0, r = 0$. The channel length and diameter are $2L \simeq 40$ mm and $2R \simeq 4.8$ mm, respectively, and the dissolving surface length is $2H = 25$ mm. The color represents the fluoride concentration. In (a) the result of the numerical calculations in the full three-dimensional model geometry can be seen in flow-off conditions. Panel (b) is a zoom-in on the channel under flow-off conditions (top) and flow-on conditions (bottom) at 1 mL min^{-1} in the positive x-direction as also indicated by the parabolic Poiseuille flow profile (white arrows). With flow, the concentration in the center of the channel essentially equals that in the reservoir. Nonetheless, a significant diffuse boundary layer remains at the dissolving surface, with a boundary layer thickness of $\delta \simeq 0.4$ mm. The thickness of the boundary layer scales as $\delta(x) \propto (x+H)^{1/3}$. The boundary layer, which is much smaller than the channel radius $\delta(x) \ll R$, reduces the effective advection rate by orders of magnitude as the effective flow rate is low in this boundary layer.

charging reaction Eq. (2.1a) cannot be a source of fluoride ions. To solve for $\sigma(x)$ we first need to obtain the surface fluoride concentration $\rho_F(x,R)$, which in turn requires solving for the fluid velocity $\mathbf{u}(x,r)$.

Diffusion-advection equation The profiles of the ionic concentrations, the pressure, and the fluid velocity follow from the diffusion-advection (Eq. (2.4)) for ionic transport and the incompressible Stokes (Eq. (2.5)) for the fluid velocity $\mathbf{u}$,

$$\partial_t \rho_i = \nabla \cdot (D\nabla\rho_i - \rho_i \mathbf{u}) = 0 \tag{2.4}$$

$$\partial_t \mathbf{u} = \eta\nabla^2\mathbf{u} - \nabla P = 0; \quad \nabla\cdot\mathbf{u} = 0. \tag{2.5}$$

Here D is the diffusion constant that is assumed to be equal for all ionic species.

It is computationally not feasible at the centimeter length scales of the experiment to resolve the electric double layers at the solid-liquid interface on the nm scale. Hence, we neglect a conduction term to Eq. (2.4) and a coupling to the Poisson equation that would be required to account for electrostatics. Given that the concentration profiles of sodium, hydrogen, and chloride ions have no sources and sinks and are not affected by conduction within this approximation, we can assume them to be spatially constant, with values set by the reservoir. Moreover, since $\partial_t \sigma = 0$ and $J_{\mathrm{Ca}} - 2J_{\mathrm{F}} = 0$, we can reduce the number of concentration profiles further by imposing local charge neutrality and hence setting $\rho_{\mathrm{F}} = 2\rho_{\mathrm{Ca}}$ in the simplest version of the theory that we focus on here in this Chapter. However, in the Appendix of this Chapter we go beyond the assumption of local charge neutrality and allow for electric double layers by solving a similar, but orders of magnitude smaller, system with a conduction term and the Poisson equation; we find that the non-electrostatic version of the theory captures the key physics.

To solve for the fluoride concentration, we seek solutions to Eqs. (2.4)-(2.5) that satisfy the following boundary conditions. Deep in the two reservoirs, we impose identical ionic bulk concentrations $\rho_{i,\mathrm{b}}$ for each species in the reservoir, and a pressure that differs by an imposed pressure drop ΔP. On the solid channel wall we apply no-slip boundary conditions for the flow velocity and vanishing normal fluxes for fluoride for $H < |x| < L$. On the dissolving wall, at $|x| < H$, we impose the dissolution and precipitation reaction (2.1b), resulting in $\mathbf{n} \cdot \nabla \rho_{\mathrm{F}}(x,R) = J_{\mathrm{F}}(x)/D$, where $J_{\mathrm{F}}(x)$ is the normal flux of fluoride ions into the solution given by

$$J_{\mathrm{F}}(x) = 2k_{\mathrm{dis}}\left(1 - \frac{k_{\mathrm{prec}}}{2k_{\mathrm{dis}}}\rho_{\mathrm{F}}^3(x,R)\right). \tag{2.6}$$

Here we introduced the surface normal $\mathbf{n}$ pointing into the solution, the dissolution rate-constant $\mathrm{k_{dis}}$ of the CaF_2 units, and the precipitation rate-constant $\mathrm{k_{prec}}$, in line with the reaction of Eq. (2.1b); the prefactor 2 is a stochiometric constant resulting from the fact that two F^- ions go into the solution when one CaF_2 unit dissolves. The ratio of the rate constants defines the saturation concentration $\rho_{\mathrm{F,sat}} = (2k_{\mathrm{dis}}/k_{\mathrm{prec}})^{1/3}$ upon which no further dissolution occurs. Note that the local concentrations govern the net precipitation rate at the surface, which couples to the flow through the advection term in Eq. (2.4), such that a flow-dependent surface charge is obtained if the dissolution and charging reactions share an ion; for CaF_2 the shared ion is F^-.

Boundary conditions Due to dissolution, the net flux of ions into the flow channel creates, even without flow, a reaction-diffusion equilibrium concentration profile that extends over the length of the channel and into the two reservoirs, as illustrated in Fig. 2.2(a). With flow, a lateral and a normal gradient of fluoride ions develop because the fluid flow increases the rate of transport out of the channel,

the more so on the central axis of the channel where the flow velocity is largest, as is evident from Fig. 2.2(b). In the Appendix of this Chapter we show that at the high flow rates applied in the experimental system the concentration profile is confined to the surface within the diffuse-boundary length $\delta(x) = (9DR(x+H)/(4\bar{u}))^{1/3}$ which at the channel centre has a length $\delta(0) \simeq 0.4$ mm and scales as $(x+H)^{1/3}$ with $x \in [-H,H]$, and here $\bar{u}$ is the average flow velocity. The radial concentration profile at the surface is well described by classical diffuse boundary layer theory as discussed in the Appendix. As the diffuse boundary layer is localized at the channel wall where the fluid velocity is low, advective transport is inefficient allowing for a surface concentration $\rho_{\mathrm{F}}(x,r)$ that deviates significantly from the bulk concentration $\rho_{\mathrm{b,F}}$ even at the high flow rates applied in the experimental system.

2.4 Concentration, surface charge and dissolution profiles

We have numerically calculated the fluoride concentration profiles and fit the experimental v-SFG results using experimental and literature values for the model parameters (Fig. 2.3). We used $k_{\mathrm{dis}} = 0.027\mu\mathrm{mol\,m^{-2}s^{-1}}$ [46, 47], $\rho_{\mathrm{F,sat}} = 10\rho_{\mathrm{F,b}} = 10\mu\mathrm{M}$, [48], $k_{\mathrm{ads}}/k_{\mathrm{des}} = 10\mu\mathrm{M}^{-1}$, and $\Gamma = 10\ \mathrm{nm}^{-2}$. The equilibrium constant $k_{\mathrm{ads}}/k_{\mathrm{des}}$ and the density of chargeable groups Γ are not directly reported in the literature. However, the combination chosen here is not only in agreement with the experimental equilibrium surface potential of about 70 mV (if the electric double layer is taken into account) [48–50], but is also in agreement with the observed magnitude of typical flow-induced changes of the zeta potential ($\simeq$ 15 mV) as reported in streaming potential measurements [43]. The dissolution rate constant k_{dis} is low and roughly corresponds to one monolayer of the surface dissolving every hour, as expected for a poorly soluble mineral [46, 47].

Surface-charge and -potential profiles Fig. 2.3(a) shows the comparison between the experimentally observed changes in v-SFG intensity as a function of flow rate and position and those found in our numerical calculations (in which we tune the pressure drop to fit the experimental flow rate). The overall increase in the v-SFG response with increasing flow rate and its decrease from the inlet to the outlet is very similar to the characteristics of the surface charge (Fig. 2.3(b)). The surface charge increases by 50-100% compared to no-flow conditions, and varies by 10-20% laterally. The corresponding change in the surface potential ψ_0 (as calculated by the Gouy-Chapman relation $\psi_0 = (2k_{\mathrm{B}}T/e)\sinh^{-1}(2\pi\sigma\lambda_{\mathrm{B}}\lambda_{\mathrm{D}})$) is significantly lower in this nonlinear screening regime where ψ_0 exceeds the thermal voltage of 25 mV, differing by only around 20% between the flow-on and flow-off states. Here $\lambda_{\mathrm{B}} = 0.7$ nm is the Bjerrum length of water at room tem-

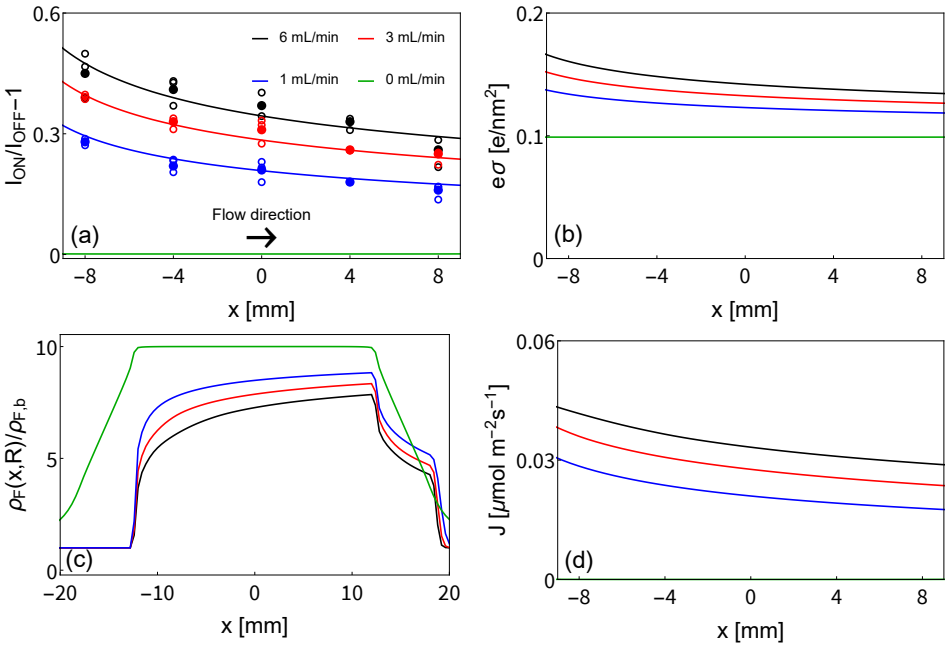

Figure 2.3: (a) Calculated (lines) and experimentally obtained (symbols) relative changes in the v-SFG intensity along the mineral surface for different flow rates. (b) Calculated surface charge along the mineral surface for different flow rates, showing enhancements under flow-on conditions by $\sim 50\%$ compared to flow-off conditions. (c) Calculated fluoride concentration at the surface $\rho_F(x,R)$ relative to the bulk along the mineral surface for several flow rates. (d) The calculated net dissolution rate $J(x)$ (Eq. (2.7)) along the mineral surface for different flow rates. Note the orders of magnitude increase of dissolution upon turning on the flow. Under flow-off conditions, the dissolution rate is a small fraction of the maximum dissolution rate $J = 10^{-5} k_{\rm dis}$ while during flow the net dissolution increases by several orders of magnitude, to approximately half the maximal dissolution rate $J \simeq k_{\rm dis}$. The x position is given as displacement from the center with values increasing in the direction of flow, indicated by the arrow in panel (a).

perature and $\lambda_D = 7$ nm the Debye length for a solution of 1 mM of NaCl and pH 3. Finally, to estimate the change in the SFG intensity, we use the approximation $(I_{\rm on} - I_{\rm off})/I_{\rm off} = (\psi_{0,\rm on}/\psi_{0,\rm off})^2 - 1$, as discussed in Supplementary Note 1 of [44], with $I_{\rm on}$ and $I_{\rm off}$ denoting the v-SFG intensity at flow-on and flow-off conditions.

The validity of the Gouy-Chapman relation is verified in the Appendix of this Chapter, where we show that the curvature of the channel wall on electrostatics can be neglected, which is expected as the Debye length is much shorter than the channel radius, $\lambda_D/R \ll 1$. This also justifies approximating the dissolving surface, which is a flat plate in the experiments, by a cylindrical channel wall in our numerical calculations. Similarly, the diffuse boundary layer and the electric

double layer do not affect each other as their thicknesses differ by orders of magnitude, $\lambda_D/\delta \simeq 10^{-4}$. The calculated interfacial fluoride concentration (Fig. 2.3(c)) decreases with increasing flow rate and increases from inlet to outlet. The reverse relation between fluoride concentration and surface charge stems from the Langmuir isotherm (Eq. (2.3)). Interestingly, although the fluoride concentration increases in the flow direction, Fig. 2.3(c) shows that the flow-induced dilution ensures that the concentration is lower throughout the channel than in the no-flow state. The concentration at the boundary of the dissolving area, at $x = -H$, is equal to the bulk concentration $\rho_{F,sat}$ in flow-on conditions, beyond which it rises rapidly and then slowly reaches a maximum at $x = H$. This rapid increase of the fluoride concentration at $x = -H$ is due to the locally low precipitation rate compared to upstream locations near $x = H$.

Concentration- and dissolution-profiles In the no-flow state, the fluoride concentration in the center corresponds to the saturation concentration $\rho_{F,sat}$. Without a precipitation reaction, the concentration would even be orders of magnitude larger. In our calculations that describe the experiment, the flow-induced change in fluoride concentration is on the order of $\sim 30\%$ of the saturation concentration ($\rho_{F,sat} = 10\mu M$), as is evident from Fig. 2.3(c). In an absolute sense, this change of concentration is orders of magnitude lower than the background ionic strength (~ 2 mM). While the change in F^- concentration is sufficient to affect the surface charge, it is negligible for the total ionic strength that governs the screening of the surface charge. Thus, we can conclude from our combined experiments and theory that the flow-induced changes in the v-SFG signal are connected to the surface charge itself rather than changes in charge screening.

Finally, we draw attention to Fig. 2.3(d), which reveals that the net dissolution rate also exhibits a gradient along the mineral surface and increases with flow rate. Similar to the position- and flow rate-dependent shift in surface charge, the position-dependent net dissolution rate is also a result of the heterogeneous concentration profile. More importantly, however, we can see that the dissolution rate increases by orders of magnitude from flow-off to flow-on conditions. In the flow-off state, the surface concentration is nearly equal to the saturation concentration $\rho_F(x,R) \simeq \rho_{F,sat}$, which causes the net dissolution rate in flow-off conditions to be small $J \simeq 10^{-5} k_{dis}$. As the fluoride concentration decreases in flow-on conditions, the net dissolution rate increases dramatically and almost reaches its maximal value $J \simeq 2k_{dis}$. The net dissolution rate thus increases by $\sim$5 orders of magnitude due to flows of $\sim$ mL min^{-1} (or shear rates 1.5-9 s^{-1}), from effectively 10^{-7} to 10^{-2} μmol m^{-2} s^{-1}.

2.5 Relevant length and timescales

To investigate the universal scaling behavior of the fluoride concentration with channel geometry, dissolution, and flow rate, we derive in the Appendix an analytic expression for the radially averaged fluoride concentration profile $\rho_F(x)$ in the thin channel limit $\delta \gg R$ (such that $\rho_F(x,R) = \rho_F(x)$) and with negligible precipitation $k_{dis} \gg k_{prec}$. While these two conditions are not met by the experimental system, we can extract key parameters controlling the dominant physics, the first of which is the Péclet number Pe$= (2\bar{u}L)/D$, where $\bar{u}$ is the channel-averaged fluid velocity, and the second being the dimensionless concentration difference $\Delta\rho_F/\rho_{b,F} = (k_{dis}L^2)/(DR\rho_{b,F})$ between the channel center and the reservoir under flow-off conditions. Here Pe captures the importance of advective transport relative to diffusive transport and $\Delta\rho_F$ is a measure for the dissolution rate. In Fig. 2.4(a), we plot our analytic expression of $\rho_F(x)/\rho_{F,b}$ for the geologically relevant case $\rho_{F,b} = 10^{-6}$ mol L^{-1} and $\Delta\rho_F = 3.6\rho_{F,b}$ for several values of Pe, yielding remarkable agreement with our numerically exact solution of Eqs. (2.4)-(2.5) for the long-channel limit.

Limiting concentration profiles Interestingly, the parabola-like low-Pe regime and the linear-like high-Pe regime of the graphs in Fig. 2.4(a) are borne out by the limiting cases of our analytic expression derived in the Appendix, which are given by

$$\rho_F(x) - \rho_{b,F} = \begin{cases} \Delta\rho_F\left(1 - \dfrac{x^2}{L^2}\right) & \text{if Pe} \ll 1, \\ \dfrac{4\Delta\rho_F}{\text{Pe}}\left(1 + \dfrac{x}{L}\right) & \text{if Pe} \gg 1. \end{cases} \tag{2.7}$$

This expression makes explicit that all excess fluoride gets washed out of the channel for Pe$\gg 1$, the more so at the inlet ($x = -L$) than at the outlet ($x = L$). In Fig. 2.3(b), we plot the fluoride concentration at the center of the channel ($x = 0$) in the full range of Pe, which reveals a diffusion-dominated (Pe$\ll 1$) and an advection-dominated (Pe$\gg 1$) regime with Pe-independent limiting fluoride concentrations; a significant dependence on Pe is only found in a rather narrow crossover regime at $1 <$Pe$< 10^2$. This narrow Pe regime could explain why previous authors did not observe a change in surface charge when the flow rate was varied [32, 35, 37, 45], as there is little flow dependency in the high Péclet regime (Pe$\gg 10^3$). Note that if the thin channel-condition $\delta(x) \gg R$ is not met (as is the case for the experiments) the Péclet number has to replaced by the Sherwood number Pe$^{1/3}<$Sh$<$Pe$^{2/3}$ as discussed in the last part of the Appendix. For the experimental conditions considered the Sherwood number lies between 40 and 1000 for Pe$\simeq 10^5$ just within the range where variation of concentration with flow should still be observable as shown in Fig. 2.4(b). As Sh grows much smaller than

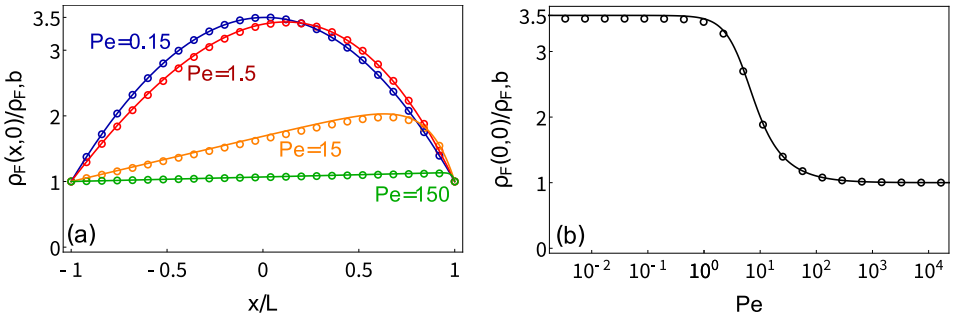

Figure 2.4: (a) Numerical (points) and analytic (solid lines) results for the radially averaged fluoride concentration profile in the channel as a function of the distance from the center for Péclet numbers ranging from Pe$= 0.31$ ($\bar{u} \simeq 1.9$ μm min^{-1}, blue) to 3100 (average flow velocity 1.9 cm min^{-1}, green). (b) Radially averaged concentration at the center of the channel as a function of the Péclet number, comparing analytic (solid lines) and numerical (symbols) results for geologically realistic values ($k_{\mathrm{dis}} = 10^{-5}$ μmol m^{-2} s^{-1}, $L = 1$ cm, $D = 1$nm^2 ns^{-1}, $\eta = 1$ mPa s). Note that the considered geometry has length $L = 1$ cm and radius $R = 0.1$ mm ensuring that the radius is much smaller than the boundary layer thickness, which is not the case for the experimental geometry.

the Péclet number, the transition between flow and no-flow states is broadened in the wide channel-limit $\delta(x) \ll R$.

Slow dissolution Having explained why the surface charge varies with the flow magnitude, the question remains how an almost insoluble mineral such as CaF_2 can give rise to a significant concentration difference ($\Delta\rho_{\mathrm{F}}/\rho_{\mathrm{b,F}} > 1$). This unexpected result can be understood by interpreting $\Delta\rho_{\mathrm{F}}/\rho_{\mathrm{b,F}}$ as a ratio of the diffusion timescale $\tau_{\mathrm{dif}} = L^2/D \simeq 10^5$ s, the time needed for a fluoride ion to diffuse from center to outlet, and the dissolution timescale $\tau_{\mathrm{dis}} = \rho_{\mathrm{F,b}} R/k_{\mathrm{dis}} \approx 10$ s which is the typical time dissolution needs to double the bulk concentration. While the typical time for the concentration to change by dissolution is slow, the timescale by which diffusion can smooth out this concentration change is even slower in the present case of a long macroscopic channel. As the slow dissolution is offset by the even longer diffusion time a significant concentration profile is expected ($\Delta\rho_{\mathrm{F}}/\rho_{\mathrm{F,b}} = \tau_{\mathrm{dif}}/\tau_{\mathrm{dis}} > 1$). Note that the dissolution time is determined by the surface-to-volume ratio of the channel and is hence linear in the radius R, while the diffusion time is quadratic in the channel length L. Thus the dimensionless concentration difference $\Delta\rho_{\mathrm{F}}$, which needs to be of order unity or larger for a flow-dependent surface charge and dissolution rate, is strongly dependent on both the absolute length L as well as the aspect ratio L/R of the channel. In fact for macroscopic channels with large aspect ratio $\Delta\rho_{\mathrm{F}}$ inevitably becomes so large that the assumption of a negligible precipitation reaction is invalidated. Moreover, the inverse scaling of $\Delta\rho_{\mathrm{F}}$ with the bulk fluoride concentration $\rho_{\mathrm{F,sat}}$ explains the ex-

perimental finding of Ref. (2.3) that there is no flow-dependent surface charge when an excess of fluoride is added.

2.6 Discussion

Our theoretical model combined with the v-SFG experiments of our collaborators can be transferred to other interfaces to determine the charging reaction mechanism and dissolution reaction mechanism. In the present case of calcium fluoride, the surface charging reaction (Eq. (2.1a)) is desorptive, which implies that a decrease in the fluoride concentration increases the surface charge. Meanwhile, the dissolution reaction (Eq. (2.1b)) is a source of reactive ions and hence increases the fluoride concentration. As flow brings the concentration closer to the reservoir's bulk concentration, the surface charge increases, more so at the inlet than at the outlet. The sign of the charges (i.e., whether an anion or cation is released) does not play a role in the surface charge's flow dependency. Interestingly, the combination of the surface being charged by desorption and dissolution being a source of ions partaking in this charging reaction is only one of several ways to establish a flow-dependent surface charge.

Chemistry-specific surface charge gradient For instance, a precipitating surface in contact with an oversaturated solution is a sink for the reactive ions. In this case, the concentration would increase upon flow, which for a desorptive charging mechanism would lead to a decrease, rather than an increase, in surface charge closer to the inlet. Another charging mechanism is the adsorption of a reactive ion, where the surface charge increases with increasing concentration of reactive ions. This causes the surface charge to increase upon flow when the surface is a sink and to decrease upon flow when the surface is a source of reactive ions. Note that whether the surface is a sink or a source of ions is not necessarily determined by whether the mineral is dissolving or precipitating. For instance, protons play a role in the charging of iron oxide surfaces and are consumed when iron oxide dissolves [51]. In this case, the surface is a sink below the saturation concentration and a source above saturation concentration. As protons are often consumed in dissolution and partake in the charging of metal oxides, we expect such counter-intuitive behavior to be relatively common.

We summarize the expected change in surface charge upon flow for different combinations of charging and dissolution reactions in Table 2.1. If either the dissolution or charging reaction is known, the other reaction mechanism can be established by inspecting the sign of the v-SFG change upon flow or the slope of the surface charge gradient. This could be useful for the study of other minerals, for instance, the notoriously complex surface chemistry of silica [39, 52–56].

Surface \ Charging	Desorptive	Adsorptive
Source	+	-
Sink	-	+

Table 2.1: Indication whether the surface charge increases (+) or decreases (-) upon flow. Column position indicates if the surface is a source or sink of reactive ions, row position indicates if the reactive ion desorbs or adsorbs to generate surface charge. The change of surface charge upon flow is always larger at the inlet than at the outlet.

Surface charge gradients in soil Next we discuss in what natural setting flow-dependent charge and dissolution could be relevant, considering a common geological system. While we have focused on the position-dependent surface charge, as this is a quantity indirectly measured by v-SFG, the dissolution flux of Eq. (2.6) also depends on the fluoride concentration. Therefore, our model directly and naturally implies that also the dissolution flux is flow- and position-dependent. This insight brings us to discuss the more general case of mineral dissolution in geological environments, particularly whether and where such a dissolution rate gradient can be expected. As already emphasized, the gradients of interfacial concentrations can only be significant if there is a sufficiently large relative concentration difference ($\Delta\rho_F/\rho_{F,b} \gg 1$) between the reservoir and the channel (or porous material) without flow. At first sight, this requires high dissolution rates.

However, also the geometry and the channel dimensions play a role, and we have seen that macroscopic and elongated channels are favorable for a large $\Delta\rho_F$. These conditions are met naturally in porous networks such as rocks and soils. In addition to the condition of a significant concentration difference, also a significant fluid velocity, or Péclet number, is required. Using our analytic results (Eq. 2.7), we estimate that in pores of centimeter lengths ($L = 10^{-2}$ m) and submillimeter widths ($R = 10^{-4}$ m) and for fluid velocities of $u = 10^{-5}$ m s^{-1} and dissolution rate constants that exceed ($k_{dis} = 10^{-11}$mol m^{-2} s^{-1}), there will be a significant surface charge gradient. We note that these dissolution rates are typical for silicate minerals[57, 58], and these flow rates are typical for water flow through soils [59, 60].

We compare numerical and analytic results for these parameter values at different flow rates in Fig. 2.4(b). The concentration profile changes dramatically from a no-flow state to a flow velocity of u =10^{-5} m s^{-1} corresponding to Pe$\approx 10^2$. In the case that the concentration in the pore becomes close to the saturation concentration ($\Delta\rho_F \simeq \rho_{F,sat}$), there will also be a flow rate and position-dependent dissolution rate. Such a flow-dependent dissolution rate has been suggested to explain commonly observed dependencies of dissolution rate with pore size [58]. Therefore, our findings can be expected to be of geological relevance. Additionally,

our approach of combining the model and position-resolved v-SFG experiments itself could be used to investigate charging and dissolution mechanisms, which are important for soil remediation [37] and industries such as froth flotation [34].

2.7 Conclusion

In conclusion, we explain why the surface charge and dissolution rate of calcium fluoride show macroscopic gradients along the interface when flow is applied. This was shown through experimental observations by our experimental collaborators using surface-specific v-SFG spectroscopy and full numerical calculations of reaction-diffusion-advection equations, including the interfacial chemistry at water-mineral interfaces. The observed gradient in the v-SFG response can be correlated to a gradient in the surface charge upon flow. A dissolution-diffusion-advection process can entirely explain such a gradient. The key physicochemical mechanism is captured by the coupling of a dissolution reaction with flow and surface charge. This dissolution reaction creates a steady-state concentration profile of fluoride ions, which depends on both position and flow rate. Both the surface charge and dissolution rate are influenced by the local fluoride concentration. Thus, dissolution both causes a position-dependent dissolution rate as well as a position-dependent surface charge when flow is applied.

Our reaction-diffusion-advection model can be generalized to arbitrary surface and dissolution reactions. Interfaces exhibiting both dissolution and charging in flowing water occur naturally in a wide variety of systems, and only minor confinement is needed to ensure that both surface charge and dissolution rate depend on position and flow rate. Thus, our finding of a flow-induced gradient in the dissolution reaction is expected to impact geological research of porous materials. Also, scientific disciplines that rely on the use of surface potentials, such as electrokinetics, microfluidics, and nanofluidics, or those involving measurements of surface potentials may be interested in its dependency on the position and flow rate.

2.8 Appendix

2.8.1 Flow-induced change in surface charge

One needs an interface-specific method to obtain a fundamental understanding of the events occurring at interfaces. At solid-water interfaces, vibrational Sum Frequency Generation (v-SFG) is a well-established method that is interface-specific and provides molecular information [30, 32, 41, 45, 61–70]. The interface-specificity of v-SFG results from the selection rule that inversion symmetry must be broken for a v-SFG signal to be generated. If the solid-liquid interface is charged, the resulting electric field aligns the dipole moments of the interfacial water molecules. Additionally, the electric field also polarizes the water molecules some nanometers into the solution. Since both phenomena break the symmetry, the strength of the observed v-SFG signal increases with the average polarization and orientation of the water molecules. Therefore, the v-SFG response is a measure of the electric field at the surface (see Supplementary Note 1 of [44] for details) [30, 32]. By Gauss' law, this field is connected to the surface charge and is directly related to the surface potential. Similar to Lis et al. [32] and Xi et al. [45], the flow experiments at the CaF_2-water interface were performed under acidic conditions, first at a single position in the channel. Fig. A2.1(a) illustrates this experiment. Fig. A2.1(b) shows two v-SFG spectra of the CaF_2-water interface for a 1 mM NaCl and 1 mM HCl (so pH 3) solution, once under flow-off and once under flow-on conditions. The measured signal is plotted vs. the wavenumber of the IR pulse being in resonance with the OH stretch vibration of water molecules. The flow-on (red) spectrum in Fig. A2.1(b) is $\sim 40\%$ higher in intensity compared to the flow-off (blue) spectrum in Fig. A2.1(b). This increase can be correlated to an increase in surface charge, see Supplementary Note of Ref. [44] for details. Thus, the experimental finding that flow increases the surface charge at the CaF_2-water interface under acidic conditions [32, 45] was reproduced by our experimental collaborators.

The signal intensity of the two spectra of Fig. A2.1(b) was calculated by integrating over the spectral area. The variation of this signal in time upon switching on and off the flow was resolved with a resolution of seconds, as shown in Fig. A2.1(c), where each black circle stems from one spectrum. The v-SFG response is constant in time before the liquid flow is switched on, which therefore represents a steady state. Upon applying flow the intensity changes, reaching another steady state with a higher v-SFG intensity within approximately 5 minutes. When the flow is turned off again, the initial steady state is restored but equilibration takes about 10 minutes. As explained in the previous section, the v-SFG response can be used as a measure for the surface charge. Thus, the flow-induced change in the v-SFG signal can be correlated to a reversible change in surface charge due to flow. These observation of reversible changes in the v-SFG

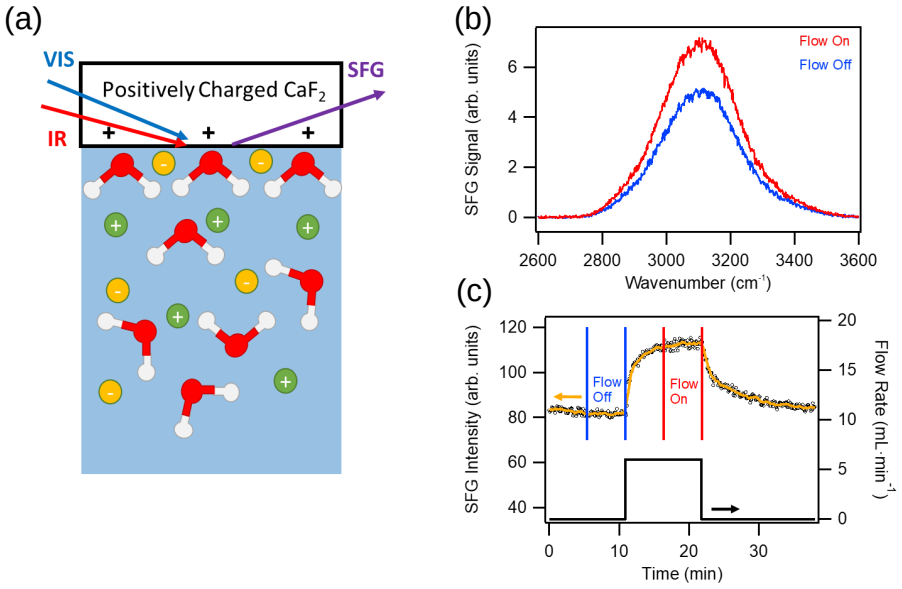

Figure A2.1: (a) Illustration of the measurement method employed our experimental collaborators. In vibrational sum frequency generation (v-SFG) spectroscopy, a visible (VIS) and infrared (IR) pulse overlap in space and time at the interface of interest, generating radiation at the sum of the frequencies (SFG). If an IR pulse is in resonance with the OH stretch vibration of water molecules, the obtained v-SFG spectra provide information on the orientation and polarization of interfacial water molecules. The illustration shows water molecules for the first few hydration layers as well as a schematic distribution of arbitrary ions (anions in yellow, cations in green). At the charged CaF_2-water interface, the orientation and polarization of the interfacial water molecules is determined by the surface charge. Thus, the v-SFG signal can be used as an indirect measure for the surface charge. (b) v-SFG spectra in arbitrary units (arb. units) in the OH stretch region of the CaF_2- water interface at pH 3 (1mM HCl and 1 mM NaCl) under flow-off conditions (blue) and flow-on conditions (red). (c) Time trace of integrated SFG spectra (black circles) at the CaF_2-aqueous solution interface at pH 3 (1mM HCl and 1 mM NaCl) with one flow on-off cycle (black curve). Each circle represents one spectrum, integrated between 2650 and 3600 cm^{-1}. The solid orange line is a ten-point moving average to guide the eye. The vertical blue and red lines highlight the steady-state regimes for flow-off and flow-on conditions. As the intensities are hardly changing over time, a steady-state can be assumed.

response and thus in surface charge due to liquid flow is consistent with the studies of Lis et al. [32] and Xi et al. [45]. In the theory section we explain why this surface charge increase upon flow occurs.

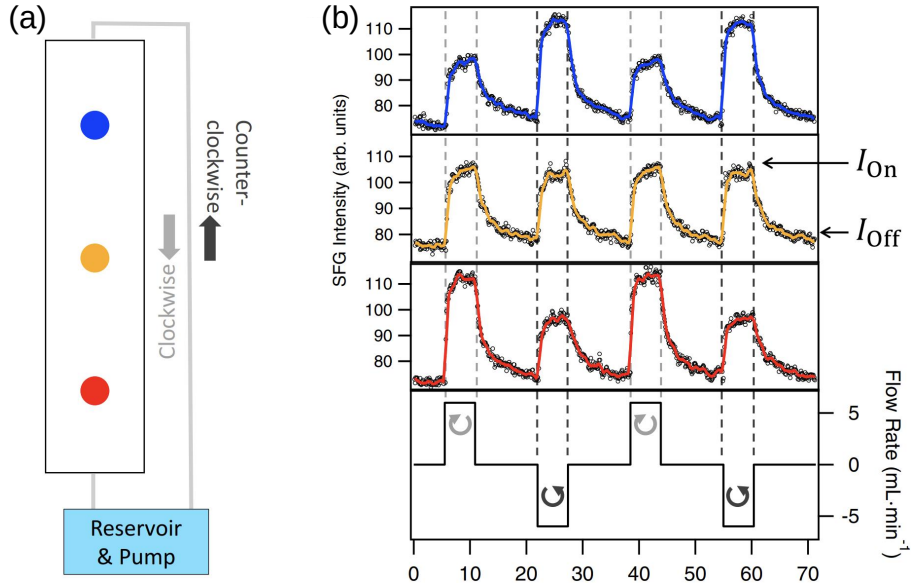

Figure A2.2: (a) Schematic representation of the flow set-up. The aqueous solution reservoir (100 mL of a 1 mM NaCl and HCl (pH 3) solution) is pumped via tubes and the flow cell using a peristaltic pump. The flow channel is 24.8 mm long, 4.3 mm deep, and 4.8 mm wide. The flow direction can be changed from clockwise to counterclockwise. The v-SFG spectra were recorded at three spots in the channel. One spot in the center (yellow) and two points separated by 8 mm from the center in the two directions of the flow channel (blue and red, respectively). (b) Time trace of integrated SFG spectra (black circles) at the interface of the solution and calcium fluoride for several flow on-off cycles (black curve). As indicated by the arrows and the different signs of the flow rate, different flow directions were employed. The colored solid lines are ten-point averages to guide the eye and highlighting at which spot in the flow channel the spectra were recorded. For the time trace measured at the center, the intensity levels of the spectra with (I_{on}) and without flow (I_{off}) are highlighted by arrows.

2.8.2 Flow-induced surface charge gradient

In order to gain an understanding of the interfacial events along the mineral surface upon flow, the changes in v-SFG response were measured at different positions along the flow channel. Another approach is to compare the change in v-SFG signal upon flow at one position, which is not the center of the flow cell, and reversing the flow direction, i.e. interchanging the role of the inlet and outlet as illustrated in Fig. A2.2(a). Following the second approach, time traces of the integrated v-SFG spectra at three different positions with flow on/off cycles in clockwise and counter-clockwise flow directions are shown in Fig. A2.2(b). First of all, it can be seen that the v-SFG response increases upon flow at every position. Additionally, we observe that at the center of the flow channel (orange spot and

trace in Fig. A2.2(b)) essentially identical changes of the v-SFG intensity for both flow directions are observed, which is fully consistent with the study of LIS et al. [32] which conducted measurements at the channel center. With the measurement at the channel center no additional spatial information is obtained as reversing the flow direction interchanges the center with itself due to the flow cell's symmetry.

In contrast measuring near the channel in- and outlet (8 mm from the center) the change in v-SFG intensity strongly depends on the flow direction. Under a clockwise flow direction (as depicted in Fig. A2.2(a)), the increase in the v-SFG intensity at the red position in Fig. A2.2 is substantially and reproducibly higher than when applying a counter-clockwise flow, while this response is inverted when measuring at the other side of the flow cell (blue spot and blue trace). The v-SFG change at the center of the channel (yellow) is in between the maximum and minimum difference at respectively the in- and outlet. Thus, we conclude that the increase in the v-SFG response upon flow decreases in the flow direction, such that the measurements show that along the mineral there is a flow-induced surface charge gradient in the flow direction as depicted in Fig. 2.1.

To further investigate the proposed gradient along the flow channel, we quantitatively compare the flow-induced changes at different positions along the centimeter-sized flow channel at a single flow rate. To do so, we focus on the relative increase of the v-SFG response under flow-on conditions (compared to flow-off) as a function of the distance from the center of the channel. Additionally, we study the influence of the flow rate. The relative increase in v-SFG intensity $(I_{\mathrm{ON}}/I_{\mathrm{OFF}} - 1)$ accounts for slight changes in the alignment that necessarily occur when changing the position of the flow cell. The position-dependent relative increase in intensity is determined by averaging the intensity in steady state, as indicated by the marked regimes in Fig. A2.1(c). The obtained data are shown in Fig. 2.1, where it is clearly shown that the intensity throughout the channel increases in the flow-on state, the more so at higher flow rates and closer to the inlet, with changes up to 45% at the inlet for the highest flow rate of 6 mL min^{-1} (shear rate $\sim 9\ \mathrm{s}^{-1}$) that we consider here. Note, however, that the intensity also increases significantly, by about 10%, at the outlet at the lowest flow rate of 1 mL min^{-1} (shear rate $\sim$ 1.5 s^{-1}). At these flow rates a laminar flow is expected as the Reynolds number is bounded between 5 and 25. Qualitatively similar surface gradients are found at all flow rates, with the intensity increasing with flow rate. To the best of our knowledge, other spectroscopic flow experiments conducted so far only varied the flow rate in ranges where no such dependency has been observed [32, 45].

2.8.3 Full Poisson-Nernst-Planck-Stokes calculations

Solving the Poisson-Nernst-Planck equations with a finite element analysis requires a mesh size significantly smaller than the Debye length ($\simeq$ 10 nm), while

in this Chapter we observed that the full centimeter sized experimental geometry has to be modeled to describe the experiments. As the use of many more than 10^7 mesh elements is computationally prohibitive, we have chosen to neglect the electrostatic Poisson equation and conduction terms in this Chapter. In this Appendix, we will show that the results of full small-scale Poisson-Nernst-Planck calculations are qualitatively similar while highlighting a few minor quantitative deviations.

Numerical model The set of equations that will be solved are the same as those in Eqs. (2.2), (2.4)-(2.6) in this Chapter, but with the addition of the Poisson equation for the electric potential ψ, a conduction term added to the diffusion-advection equation and an extra electrostatic boundary condition relating the total surface charge density $e\sigma$ to the electric field over the surface normal $\mathbf{n}$. For completeness, a body force term $e\sum_i z_i\rho_i\nabla\psi$, with z_i the ion valency, has to be added to the Stokes equation. As in the experimental system fluid and current can circulate, a natural electric boundary condition is that of a closed electric circuit, with two grounded equipotential reservoirs $\psi(\pm\infty = 0)$. Summarizing, the set of equations we consider in this section is thus given by

$$\nabla^2\psi = -\frac{e}{\varepsilon}\sum_i z_i\rho_i \tag{A2.1}$$

$$\partial_t\mathbf{u} = -\nabla P + \eta\nabla^2\mathbf{u} - e\nabla\psi\sum_i z_i\rho_i \tag{A2.2}$$

$$\partial_t\rho_i = D(\nabla\rho_i + \nabla\cdot(\frac{z_i e\nabla\psi}{k_\mathrm{B}T}\rho_i) - \mathbf{u}\cdot\nabla\rho \tag{A2.3}$$

$$\mathbf{n}\cdot\nabla\psi = -e\sigma/\varepsilon \tag{A2.4}$$

$$\psi(\pm\infty) = 0. \tag{A2.5}$$

In equilibrium this set of equations reverts back to regular Poisson-Boltzmann theory, that yields a diffuse layer of excess counter-ions, the electric double layer, near the charged surface. The decay length of the electric potential in this layer is the Debye length $\lambda_\mathrm{D} = (8\pi\lambda_\mathrm{B}\rho_\mathrm{b})^{-1/2}$, where $\lambda_\mathrm{B} = e^2/(4\pi\varepsilon k_\mathrm{B}T)$ is the Bjerrum length and ρ_b the bulk concentration of an added 1:1 electrolyte. The geometry is scaled down to a cylindrical channel with length $L = 5$ μm and radius $R = 0.15\mu m$ as to make resolution of the nm electric double layer feasible. The length of the dissolving, charged surface in the middle of the channel is H =2.5 μm. When including dissolution, a concentration profile of reactive ions $\rho_\mathrm{F}(x,r)$ forms, which breaks the translational invariance along the channel. When the Debye length is much smaller than the typical length over which the concentration profile $\bar{\rho}(x)$ varies $\lambda_\mathrm{D} \ll H$ we can use the lubrication layer approximation [71] which allows us to write the surface charge as $\sigma(x) = \Gamma(1 + k_\mathrm{ads}\rho_\mathrm{F}(x,0)\exp(e\psi_0(\sigma(x))/k_\mathrm{B}T)/k_\mathrm{des})^{-1}$, which is a self-consistency rela-

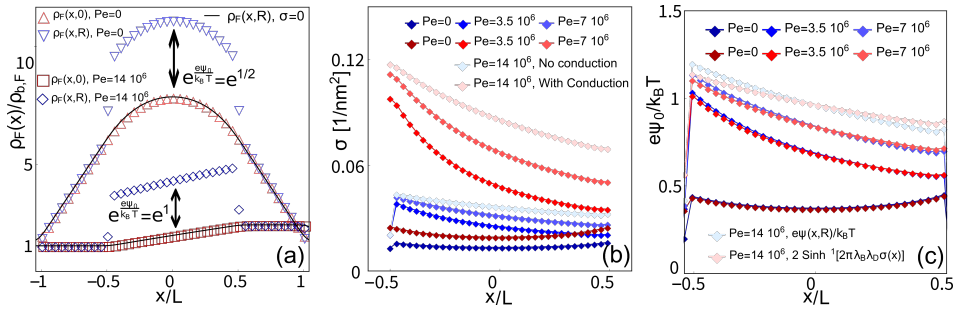

Figure A2.3: (a) The concentration on the central axis of the channel (red) and the concentration at the surface (blue) with a conduction term for the lowest and highest Péclet number investigated here, together with the corresponding profiles (gray) without conduction, which both overlap almost exactly with the red curves . The difference between the red and blue lines is due to electrostatic attraction between the surface and reactive ions, and can be accounted for by a Boltzmann factor $\exp(e\psi_0/k_BT)$. As the surface charge varies with flow rate the magnitude of this Boltzmann factor varies between 1.5 and 3. (b) Surface charge heterogeneity with conduction (orange) and without conduction (violet) for Péclet numbers 0, 1, 2 and 4 times $3.5\cdot10^6$ (dark to light). The large quantitative difference between flow on and off is due to electrostatic attraction shifting the Langmuir equilibrium, but qualitatively the trends are the same. (c) Comparison between the electrostatic potential directly extracted from the numerical calculations with conduction (gray) and the surface potential as calculated by the Gouy-Chapman (green) from the same calculation for Péclet numbers 0, 1, 2 and 4 times $3.5\cdot10^6$ (dark to light).

tion that requires a relation between the surface charge ψ_0 and surface charge σ. For this closure relation we use the well known Gouy-Chapman result derived for the surface potential of flat plates finding $e\psi_0/k_BT = 2\sinh^{-1}(2\pi\lambda_B\lambda_D\sigma(x))$, whose validity again depends on the validity of the lubrication layer approximation [71]. We compare the Gouy-Chapman surface potential with the numerically calculated surface potential in Fig. A2.3(c). Note that both the lubrication layer and Gouy-Chapman approximation work well at the considered μm length scales, and the quality of the approximations is expected to increase for the centimeter-sized experimental system .

Concentration profiles The resulting concentration profiles for Péclet numbers of one, two, and four times $3.5\cdot10^6$ can be seen in Fig. A2.3(a). These calculations were repeated without any charge on the dissolving surface, but with the same surface reaction. The concentration profile in the middle stays the same with and without the conduction term. The chief difference between these two concentration profiles is an increase of the concentration by a factor $\rho(x,R)/\rho(x,0) = \exp(e\psi_0/k_BT)$ at the charged surface due to electrostatic attraction. While this does not change any of the qualitative features of our model, namely a surface charge gradient induced by flow over a dissolving surface, it does affect the mag-

nitude of this effect as the adsorption is effectively rescaled by the Boltzmann weight $\exp(e\psi_0/k_BT)$. This can be seen in Fig. A2.3(b) where we plot the obtained surface charge with (blue) and without (red) electrostatic attraction between the charged ions and charged surface at the different flow rates; the system with electrostatic repulsion is much less sensitive to flow as the effective adsorption rate $k_{ads}\exp(e\psi_0/k_BT)$ is larger. However, as the adsorption rate is a parameter extracted from experiments to reproduce the equilibrium surface potential, this rescaling is already absorbed in the k_{ads} introduced in this Chapter. A feature not captured by the theory in this Chapter is that the effective adsorption rate $k_{ads}\exp(e\psi_0/k_BT)$ varies with surface potential and thus with flow.

Summarizing, the main conclusions from the numerical calculations with electrostatics included are that (i) the expression for equilibrated EDL's (Gouy-Chapman) is valid and hence non-equilibrium electrostatic phenomena can be neglected, and (ii) upon including electrostatic attraction between the charged surface and dissolved ions results qualitatively similar to those in this Chapter are found.

2.8.4 Analytic one-dimensional model

As analytically solving the two-dimensional dissolution-diffusion-flow problem defined by Eqs. (2.2)-(2.6) in this Chapter is intractable, we first convert the problem to an effective one-dimensional problem, which is analytically solvable.

Cross-sectional averaging We transform the two-dimensional diffusion- advection problem to a one-dimensional problem by radially integrating the diffusion-advection equation to obtain the average density $\bar{\rho}_F(x) = 2\pi/(\pi R^2(x))$ $\int_0^R \rho_F(x,r)rdr$. In the regions without dissolution, we then find

$$\partial_t \bar{\rho}_F = D\partial_x^2 \bar{\rho}_F - \partial_x \overline{u\rho}_F. \tag{A2.6}$$

Whereas the diffusive term is straightforwardly integrated, the calculation of the advective term is more complicated. This is because it results in a density-weighted velocity $\overline{u\rho} = 2\pi \int_0^R \mathrm{d}r ru(r)\rho(r,x)/\pi R^2$, which requires the knowledge of $\rho(x,r)$ which is exactly the quantity we aim to calculate. However, in the narrow-channel limit $\delta(x) \gg R$ the approximation $\rho(x,r) = \bar{\rho}(x)$ is valid as shown in Fig. 2.4, and the radially averaged diffusion-advection equation simply becomes:

$$\partial_t \bar{\rho}_F = D\partial_x^2 \bar{\rho}_F - \bar{u}_x \partial_x \bar{\rho}_F. \tag{A2.7}$$

In the opposite limit of a thin boundary layer ($\delta(x) \ll R$) the density-weighted velocity $\overline{u\rho}$ does not factorize as there is significant radial variation in the concentration profile $\rho(x,r)$. A qualitative approximation can be made in the limit of high Péclet (Pe$\gg$ 1) by replacing the average velocity $\bar{u}$ by the effective boundary transfer velocity $h \propto \bar{u}^{2/3}$ [72], as derived in the next section of the Appendix.

The boundary transfer velocity accounts for the density-weighing of the velocity and lowers the effective advection rate, as the concentration profile is localized at the channel wall where the velocity is low. The decrease of the effective velocity is given by a powerlaw $h \propto \bar{u}^{2/3}$ as the thickness of the boundary layer scales inversely with velocity.

Continuing here with the narrow channel limit $\delta(x) \gg R$, where $\overline{u\rho} = \bar{u}\bar{\rho}$, the integration of Eq. (A2.7) in the region with a dissolving surface (represented by the source term J in Eq. (2.6)) is straightforward and results in

$$\partial_t \bar{\rho}_{\mathrm{F}} \simeq D\partial_x^2 \bar{\rho}_{\mathrm{F}} - \bar{u}_x \partial_x \bar{\rho}_{\mathrm{F}} + \frac{4}{R}(k_{\mathrm{dis}} - k_{\mathrm{prec}}\rho_{\mathrm{b,F}}^3 - 3k_{\mathrm{prec}}\rho_{\mathrm{b,F}}^2(\bar{\rho}_{\mathrm{F}} - \rho_{\mathrm{b,F}})) \qquad \text{(A2.8)}$$

where the dissolution term was substituted for the radial concentration gradient at the boundary $J(x) = D\partial_r \rho(x,R)$ and two fluoride ions are released per dissolved CaF_2 unit. We linearized the precipitation in the density around $\bar{\rho}_{\mathrm{F}} = \rho_{\mathrm{b,F}}$ to ensure that the equation remains a linear, solvable differential equation.

Solving the one-dimensional problem In this Chapter we consider both regions with dissolution $|x| < H$ described by Eq. (A2.8) and regions without dissolution $H < |x| < L$ described by Eq. (A2.6). To describe the full concentration profile over the entire domain $|x| < L$ the solutions in the three different regions have to be connected by use of the proper boundary conditions. We label the solutions for the different regions as $\bar{\rho}_{\mathrm{F},i}$ with $i = 1,3$ respectively the solution within the region $H < -x < L$ and $H < -x < L$, and $i = 2$ the solution for the region in the dissolving with the dissolving surface $|x| < H$. Now the solutions can be connected by requiring the concentration profile to be continuous, giving $\bar{\rho}_{\mathrm{F},1}(-H) = \bar{\rho}_{\mathrm{F},2}(-H)$ and $\bar{\rho}_{\mathrm{F},2}(H) = \bar{\rho}_{\mathrm{F},3}(H)$. Having fixed four conditions of our three second order differential equations, the remaining two remaining boundary conditions are fixed by setting the concentration at the channel edges equal to the bulk concentration $\bar{\rho}_{\mathrm{F},1}(-L) = \bar{\rho}_{\mathrm{F},3}(L) = \rho_{\mathrm{b,F}}$. Hence Eqs.(A2.6)-(A2.8) with the six corresponding boundary conditions yield a set of three differential equations and two equalities that can be solved analytically. This method can be used to construct solutions for multiple reactive patches within complex geometries, as long as the radius $R(x)$ is continuous over the entire length. However, these solutions are not always legible or insightful and for the analytic solution we only consider the case where the entire channel is dissolving $L \simeq H$ while simultaneously neglecting precipitation, $k_{\mathrm{prec}} = 0$. The resulting expression is

$$\bar{\rho}_{\mathrm{F}}(x) = \rho_{\mathrm{b},F} + 2\frac{\Delta\rho}{\mathrm{Pe}}\left[\frac{2x}{L} + \left(1 + e^{\mathrm{Pe}} - 2e^{\frac{\mathrm{Pe}}{2}(1+\frac{x}{L})}\right)\left(\coth\left(\frac{\mathrm{Pe}}{2}\right) - 1\right)\right] \qquad \text{(A2.9)}$$

which in the limit of low and high Péclet number simplifies to Eq. (2.7) in this Chapter. Here $\Delta\rho/\rho_{\mathrm{b,F}} = k_{\mathrm{dis}}L^2/DR\rho_{\mathrm{b,F}}$ and Pe$= 2\bar{u}L/D$. It can be seen in

Fig. 2.4 of the main text that this analytic result matches numerical results in the narrow channel limit $\delta(x)/R \gg 1$.

2.8.5 Diffuse boundary layer

In this section we summarize the derivation of the diffuse boundary layer as presented in Ref. [73]. A diffuse boundary layer is the concentration profile that forms near a dissolving surface when lateral advection is so strong that there is not enough time for ions to fully spread radially by diffusion. This radial concentration profile diminishes the advective transfer rate as the concentration is high where the fluid velocity is low: near the surface.

Diffuse boundary layer theory Observing that at high Péclet numbers lateral diffusion can be neglected, the diffusion-advection equation can be written in stationary state as

$$\partial_t \rho_{\mathrm{F}} = D\nabla^2 \rho_{\mathrm{F}} - \mathbf{u}\cdot\nabla\rho \approx \frac{D}{r}\partial_r(r\partial_r\rho_{\mathrm{F}}) - u(r)\partial_x\rho_{\mathrm{F}} = 0. \tag{A2.10}$$

Now we consider a very long channel with a fully developed laminar flow profile with a laterally constant surface concentration $\rho(x,R) = \rho_{\mathrm{m}}$, for which the boundary conditions can be written as

$$\rho_{\mathrm{F}}(\pm\infty, r) = \rho_{\mathrm{b,F}}; \tag{A2.11a}$$
$$\rho_{\mathrm{F}}(x, R) = \rho_{\mathrm{m}}; \tag{A2.11b}$$
$$\partial_r\rho_{\mathrm{F}}(x, 0) = 0. \tag{A2.11c}$$

This is traditionally known as the Graetz problem [73–75]. The assumption of a constant surface concentration is not valid in the model considered in this Chapter. However, the present analysis is concerned with describing the concentration profile some distance from the surface. We will solve differential Eq. (A2.10) together with boundary conditions Eq. (2.8.5) using the Ansatz that the solution is self-similar, and that the concentration profile that depends on two variables can be described by a function of a single self-similar variable $\rho(x,r) = f(\eta)$. The existence of a self-similar solution is suggested because it is not possible to define a dimensionless lateral position using only the lateral position and velocity and hence the concentration should be reducible to a one parameter Eq. [76, 77]. Now

we define the dimensionless, self-similar, parameters

$$\eta = \frac{R-r}{\delta(x)} = (R-r)\left(\frac{4\bar{u}}{9DR(x+H)}\right)^{\frac{1}{3}}, \tag{A2.12a}$$

$$\zeta = \left(\frac{\delta(x)}{R}\right)^3 = \frac{9D(x+H)}{4\bar{u}R^2}, \tag{A2.12b}$$

$$\Theta = \frac{\rho-\rho_{\mathrm{m}}}{\rho_{\mathrm{b}}-\rho_{\mathrm{m}}}, \tag{A2.12c}$$

and using this we rewrite Eq. (2.8.5) to [73]

$$\frac{\partial^2\Theta}{\partial\eta^2} + 3\eta^2\frac{\partial\Theta}{\partial\eta} - 3\eta\zeta^{\frac{1}{3}}\frac{\partial\Theta}{\partial\zeta^{\frac{1}{3}}} = \frac{\partial\Theta}{\partial\eta}\left(\frac{3}{2}\eta^3\zeta^{\frac{1}{3}} + \frac{\zeta^{\frac{1}{3}}}{1-\eta^3\zeta^{\frac{1}{3}}}\right) - \frac{3}{2}\eta^2\zeta^{\frac{2}{3}}\frac{\partial\Theta}{\partial\zeta^{\frac{1}{3}}}. \tag{A2.13}$$

We find the dimensionless boundary conditions

$$\Theta(\eta=\infty) = 1, \tag{A2.14a}$$

$$\Theta(\eta=0\,) = 0. \tag{A2.14b}$$

The solution to Eq. (A2.13) can be expanded as $\Theta = \Theta_0(\eta) + \zeta^{\frac{1}{3}}\Theta_1(\eta) + \zeta^{\frac{2}{3}}\Theta_2(\eta) + \mathcal{O}(\zeta)$ where at high Péclet number we only consider the dominant zero-order term, also known as the Lévêque approximation

$$\frac{\mathrm{d}^2\Theta}{\mathrm{d}\eta^2} + 3\eta^2\frac{\mathrm{d}\Theta_0}{\mathrm{d}\eta} = 0. \tag{A2.15}$$

This approximation is equal to only considering the first order term of the velocity expansion [74] close to the channel boundary, and hence is valid in the limit of high Péclet number where $\delta(x) \ll R$. Solving for Θ_0 we find the Lévêque solution

$$\Theta_0 = C^{-1}\int_0^\eta e^{-s^3}\mathrm{d}s, \tag{A2.16a}$$

$$C = \int_0^\infty e^{-s^3}\mathrm{d}s = \Gamma(\frac{4}{3}) \simeq 0.9, \tag{A2.16b}$$

with Γ the Euler gamma function. Plotting the concentration profile in Fig. A2.4 as a function of the radial coordinate at $x = 0$ we find that the radial concentration profile is well approximated by the Lévêque solution. In Fig. A2.5 we plot the radial position $R-r$ at which the concentration satisfies $1.9 < \rho_{\mathrm{F}}(r)/\rho_{\mathrm{b,F}} < 2.1$ together with $\delta(x)$ as function of $(x+H)^{1/3}$. We find that the boundary layer thickness in our numerical calculations is linear in $(x+H)^{1/3}$ as expected. Thus, at $x = 0$ and a flow rate of 1 mL/min we find that the typical boundary layer thickness at which the radial concentration has decayed by 90% of its surface value is approximately $\delta(0) \simeq 0.4$ mm.

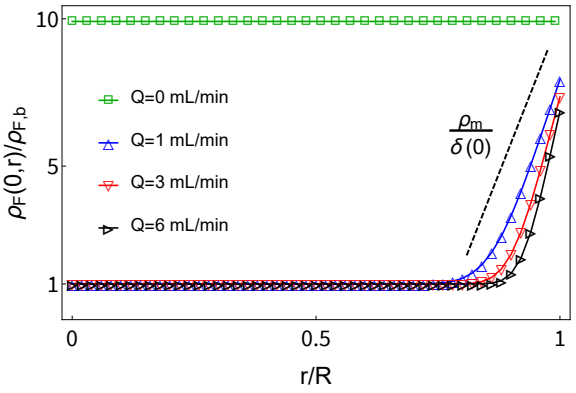

Figure A2.4: The concentration of reactive ions $\rho_{\mathrm{F}}(x,r)$ at $x=0$ with the dimensionless radial position r/R in units of the bulk concentration $\rho_{\mathrm{F},b}$ at different flow fluid fluxes $Q\in[0,6]$ mL/min. The data were obtained from full numerical calculations as described in this Chapter. It can be seen that close to the surface, the concentration profile is well described by a linear concentration profile with a slope $\rho_{\mathrm{m}}/\delta(0)$, where the diffuse boundary length $\delta(x)$ is both position and velocity dependent, and $\delta(0)\simeq 0.17R=0.4$ mm.

Surface concentration While the behavior of the concentration profile at some distance from the channel wall is thus correctly described by diffuse boundary layer theory, the near-surface ($R-r\ll\delta$) profile deviates significantly from the Lévêque solution as the assumption of a constant surface concentration is incompatible with the macroscopic concentration gradient, which is the object of interest in this Chapter. To estimate the influence of the diffuse boundary layer on the surface concentration we insert an approximation for the radial concentration profile into our analytic calculation as presented in this Appendix, which allows us to calculate $\rho_{\mathrm{m}}(x)=\rho(x,R)$. Note that while this combination of diffuse boundary layer theory and the radially integrated diffusion-advection equation does not result in a fully self-consistent theory, it allows us to estimate the change in surface concentration $\rho_{\mathrm{m}}(x)$ with regard to flow rate. This is not possible within regular diffuse-boundary layer theory as this surface concentration is an input parameter.

The fact that the diffuse boundary layer is localized near the channel wall where the velocity is low, implies that the effective velocity for the transport of ions is much lower than the channel-averaged velocity. To estimate the effect of the small boundary layer thickness we need an expression for $\rho_{\mathrm{F}}(x,r)$ such that the cross-sectional integral can be evaluated, as required for Eq. (A2.6). Inspecting the numerically obtained concentration profiles in Fig. A2.4 we see that $\rho_{\mathrm{F}}(x,r)$

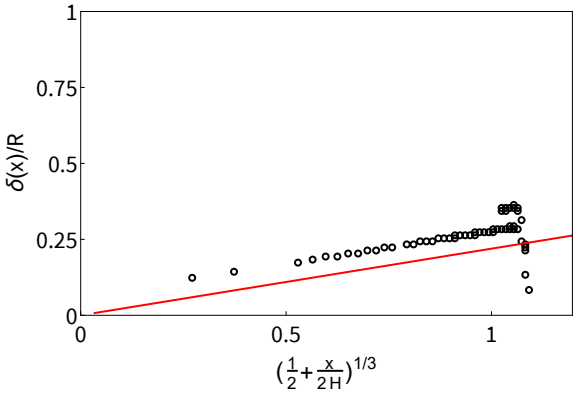

Figure A2.5: The radial position at which the concentration is between $1.9 < \rho_F/\rho_{F,b} < 2.1$ (data points) against the cube root of the lateral position $(1/2(1+x/H))^{1/3}$ for $Q = 1$mL/min confirming the cube root scaling as predicted by diffuse boundary layer theory, the red line is equal to $\delta(x)$ as given by Eq. (A2.19). At the edge of the dissolving surface $x = H$ where $(1/2+x/2H))^{1/3} = 1$ the boundary length falls off dramatically.

can be approximated by the simple form

$$\rho_F(r,x) - \rho_{b,F} = \begin{cases} 0, & \text{if} \quad r < R - \delta(x); \\ (\rho_m - \rho_{b,F})\left(\dfrac{r-R}{\delta(x)} + 1\right), & \text{if} \quad R - \delta(x) < r < R. \end{cases} \tag{A2.17}$$

With this approximation the divergence of the density weighted velocity $\overline{u\rho}$, as defined in Eq. (A2.6) becomes

$$\begin{aligned} \partial_x u\bar{\rho}_F = \partial_x\left(\frac{4\bar{u}}{3}\left(\frac{\delta(x)}{R}\right)^2(\rho_m - \rho_{b,F})\right) + \mathcal{O}\left(\left(\frac{\delta(x)}{R}\right)^3\right) \simeq \\ \partial_x \frac{4\bar{u}\delta(x)}{3R}\bar{\rho} \quad \text{if} \quad \rho_m \gg \rho_{b,F} \end{aligned} \tag{A2.18}$$

From this we can define the effective density weighted velocity h, also known as the boundary transfer velocity [75]. When the surface concentration is much larger than the bulk concentration ($\rho_m \gg \rho_b$), and the gradient in the surface concentration is larger than the gradient in the boundary thickness ($\rho_m^{-1}\partial_x\rho_m \gg \delta^{-1}\partial_x\delta$) then the boundary transfer velocity is simply given by $h = 4\bar{u}\delta/3R$. As seen from Eq. (A2.12a) the boundary thickness scales as $\delta \propto \bar{u}^{1/3}$ and hence the effective transfer velocity

$$h = \frac{4\bar{u}}{3}\frac{\delta}{R} \propto \bar{u}^{\frac{2}{3}} \tag{A2.19}$$

From this it can be straightforwardly seen that the Sherwood number Sh, which is the dimensionless number comparing the boundary transfer rate with the diffusion

rate, scales as $\mathrm{Sh} \propto \mathrm{Pe}^{2/3}$ [73, 75]. Comparing this result with the well-known Sherwood number for a channel wall kept at a constant concentration, in which case $\mathrm{Sh} \propto \mathrm{Pe}^{1/3}$, here we find that a simplified model for a dissolving channel allowing for a heterogeneous surface concentration $\rho_{\mathrm{m}}(x)$ produces an exponent of 2/3.

Summary The Sherwood number replacing the Péclet number and scaling $\mathrm{Sh} \propto \mathrm{Pe}^{\nu}$ with $\nu < 1$ captures an important aspect of the experiment, namely that the effective advection rate over the boundary layer is much lower than the channel-averaged advection rate. This causes the sharp transition between the flow and no-flow concentrations seen in Figure 2.4(b) of the main text to broaden significantly, allowing us to observe the transition between the no- and high-flow regimes. In the experiments of the main text $\mathrm{Pe} \approx 10^5$, and hence the Sherwood number $\mathrm{Sh} \in [40, 2000]$. As this is exactly the regime where the transition between the limiting cases of Eq. (2.7) is expected to occur, this explains why the charge varying with flow can be measured in the experiments. Another factor is the precipitation reaction which causes the net dissolution rate J to increase with flow, further opposing the concentration decrease upon an increase in flow rate. The scaling relation between surface concentration and flow rate in the case of a fully developed diffuse boundary layer is an order-of-magnitude estimation and we have not found a regime in which it is quantitatively accurate.

Chapter 3

Coulombic surface-ion interactions induce non-linear and chemistry-specific charging kinetics

Abstract

While important for many industrial applications, chemical reactions responsible for charging of solids in water are often poorly understood. We theoretically investigate the charging kinetics of solid-liquid interfaces, and find that the time-dependent equilibration of surface charge contains key information that can be exploited to reveal not only the reaction mechanism but also the valency of ions involved in the reactions. We construct a simple, polynomial, differential equation describing surface charging by combining chemical Langmuir kinetics and electrostatic Poisson-Boltzmann theory. Our results reveal a clear distinction between late-time (near-equilibrium) and short-time (far-from-equilibrium) relaxation, the ratio of which contains key information on surface chemistry. Interestingly for reactions involving two ions kinetics become similar to that of autocatalytic reactions.

This Chapter is based on the publication:

W.Q. Boon, M. Dijkstra, & R. van Roij, R., *Coulombic surface-ion interactions induce non-linear and chemistry-specific charging kinetics*, accepted by Physical Review Letters, arXiv preprint arXiv:2210.15426

There are paragraphs and figures that are taken or modified from the above-mentioned publication and its supporting information.

3.1 Introduction

Charged solid-liquid interfaces play a central role in a wide variety of industries such as food and coating production [78–80], mining [81–83], medicine [84–86], soil remediation [87–89] and even carbon capture [90]. With the advent of nanoscale fluidics one expects that charged surfaces become ever more important [91, 92]. In water and other polar solvents chemical reactions are a common mechanism by which surfaces obtain their charge. For ionic solids the de- or adsorption of a dissolved ionic compound is often preferred over the sorption of its own counterion [12, 13, 93]; for covalent solids such as polymers and metal oxides the acidic nature of surface groups ensures that the surface (de)protonates [12, 13, 94–96] in polar solvents and hence becomes charged.

However, for many processes of industrial and environmental importance relatively little is known about the surface chemistry [12, 13, 94] as the electrolytes in realistic applications contain a large variety of ions that can all undergo multiple reactions [12, 13, 97]. Due to experimental limitations the majority of studies investigating surface charging are performed at (quasi)-equilibrium conditions [12, 13]. Only recently, however, it has been shown that the kinetics of chemical surface reactions can strongly couple to electrokinetic fluid flows, thereby affecting the physical surface properties on macroscopic scales [13, 98–102]. Furthermore, with the recent advent of fast and surface specific non-linear spectroscopy the dynamic measurement of surface charge has become feasible [32, 43, 102–105]. In this context it has been explicitly stated that there is an urgent need for theoretical models to describe such experiments [106]. Traditionally, sorption kinetics is typically described by (pseudo)-first-order reactions [89, 107] that exhibit single-exponential relaxation towards equilibrium; the influence of a time-dependent surface charge is usually neglected entirely [106, 108, 109]. We are aware of one theoretical work [110] and associated review [111] that considers a surface charge that affects adsorption rate constants, which, however, does not consider the (chemistry-specific) non-linear dynamics induced by the electrostatic feedback as we do here.

Outline In this Chapter we present a theory for the charging dynamics of solid surfaces. We include the Coulombic ion-surface interactions and reveal an intricate dependence on the reaction mechanism and the valency of the reactive ions already present in a mean-field description. The Coulomb interactions not only affect the time constant of the late-time exponential decay of the surface charge towards equilibrium after an ion concentration (or pH) shock, but they also induce strongly nonlinear dynamics at early times far from equilibrium. Combined with the present-day capability to experimentally measure the time-dependent surface charge density, our theory forms a first step to unveil the surface chemistry

of technologically important but ill-understood materials [13, 106], such as silica [97, 112] and graphene [113], and of processes such as the clean-up of radioactive and heavy metals [87, 93, 114, 115].

3.2 Theoretical model

Interfaces, for instance silica in in water, commonly charge either by desorption of ionic species from neutral surface groups or by adsorption of ionic species onto neutral surfaces. While the exact charging mechanism of the silica-water interface is complex, there is support for charging by desorption of protons at high pH and adsorption of protons at low pH [97, 112, 116, 117],

$$\mathrm{SiOH}_{(\mathrm{s})} \underset{k_\mathrm{a}\rho}{\overset{k_\mathrm{d}}{\rightleftharpoons}} \mathrm{SiO}^-_{(\mathrm{s})} + \mathrm{H}^+_{(\mathrm{aq})}, \tag{3.1a}$$

$$\mathrm{SiOH}_{(\mathrm{s})} + \mathrm{H}^+_{(\mathrm{aq})} \underset{k_\mathrm{d}}{\overset{k_\mathrm{a}\rho}{\rightleftharpoons}} \mathrm{SiOH_2}^+_{(\mathrm{s})}, \tag{3.1b}$$

where $\mathrm{SiOH}_{(\mathrm{s})}$ is a neutral silanol group that is covalently bound to the (solid) glass and where $\mathrm{SiO}^-_{(\mathrm{s})}$ and $\mathrm{SiOH_2}^+_{(\mathrm{s})}$ denote a silanol group with a proton desorbed or adsorbed in Eqs. (3.1a) and (3.1b), respectively. Here ρ denotes the aqueous proton concentration at the solid surface, and the dissociation and association rate k_d and k_a will be discussed below for the charging kinetics of a single desorptive and a single adsorptive reaction, not only for monovalent reactive ions as in Eqs. (3.1a) and (3.1b) but for general valency z. While adsorption isotherms of real materials can rarely be described by just a single charging reaction [93, 117], we show in the Appendix that charging by multiple reactions can actually be well-approximated by the single-reaction kinetics presented in this Chapter for a wide range of experimental conditions.

We consider a macroscopic surface with an areal density Γ of identical surface groups. A group can only be in either a neutral or a charged state. The charging is assumed to take place either by desorption (labeled by $-$) of a cation of charge ze, or by adsorption (labeled by $+$) of a cation of charge ze, with $z \geq 0$ and e the proton charge. The areal densities of charged and neutral groups are denoted by $\sigma_\pm > 0$ and $\Gamma - \sigma_\pm > 0$ respectively, and the surface charge density is given by $\pm ze\sigma_\pm$. Note that the charging dynamics is invariant under the sign of the reacting ions, and without loss of generality we can restrict attention to reactive cations of (strictly positive) valency z. Assuming the chargeable surface sites to be independent, we can describe the reaction kinetics in terms of the time-dependent surface density $\sigma_\pm(t) > 0$ which satisfies Langmuir kinetics described by [118]

$$\partial_t \sigma_- = k_\mathrm{d}(\Gamma - \sigma_-) - k_\mathrm{a}\sigma_-\rho(\sigma_-), \tag{3.2a}$$

$$\partial_t \sigma_+ = k_\mathrm{a}(\Gamma - \sigma_+)\rho(\sigma_+) - k_\mathrm{d}\sigma_+. \tag{3.2b}$$

Here k_d and k_a are the rate constants of the desorption and adsorption of the reactive ion, and $\rho(\sigma_\pm)$ is the volumetric concentration of reactive ions at the surface.

The equilibrium surface charge follows from $\partial_t \sigma_\pm = 0$ and is given by $\sigma_{\pm,\mathrm{eq}} = \Gamma(1+(k_\mathrm{a}\rho_\mathrm{eq}/k_\mathrm{d})^{\mp 1})^{-1}$, which reduces to an explicit "Langmuir isotherm" in the case that the equilibrium concentration of the reactive ions $\rho_\mathrm{eq} \equiv \rho(\sigma_{\pm,\mathrm{eq}})$ is a constant independent of $\sigma_{\pm,\mathrm{eq}}$. In general, however, this Langmuir isotherm is a self-consistency equation for $\sigma_{\pm,\mathrm{eq}}$ that requires an additional "closure" relation $\rho(\sigma_\pm)$ for an explicit equilibrium solution $\sigma_{\pm,\mathrm{eq}}$. Without (Coulombic) interactions between surface and ions, the local concentration $\rho(\sigma_\pm)$ of reactive species in the vicinity of the surface would be equal to the bulk concentration ρ_b of the reactive ions far from the surface (which is independent of $\sigma_\pm$), such that Eqs. (3.2a)-(3.2b) would be linear differential equations whose solution can be written as $s_\pm(t) = 1 + (s_\pm(0)-1)\exp[-(k_\mathrm{d}+k_\mathrm{a}\rho_\mathrm{b})t]$ with the dimensionless charge $s_\pm = \sigma_\pm/\sigma_{\pm,\mathrm{eq}}$ such that $s_{\pm,\mathrm{eq}} = 1$; here $s_\pm(0)-1$ is the integration constant and denotes the relative deviation from equilibrium at the initial time $t = 0$. Note that the condition $0 \leq \sigma_\pm(t) \leq \Gamma$ implies that $0 < s_\pm(0) < \Gamma/\sigma_{\pm,\mathrm{eq}}$, where the lower bound corresponds to an initially neutral surface whereas the upper bound can be as large as $\mathscr{O}(10-100)$, since typical equilibrium conditions have a charge occupancy of only a few percent of the total number of chargeable groups [119]. Thus from measurements of $\sigma_\pm(t)$ at various concentrations of reactive (dissolved) species both k_d and k_a could in this non-interacting case be determined.

3.3 Electrostatic surface-ion interaction

However, as the charged surface attracts or repels reactive ions, Eqs. (3.2a) and (3.2b) are complicated by a nontrivial relation $\rho(\sigma_\pm)$, which causes a charge-dependent decay rate and introduces deviations from purely single-exponential relaxation of $\sigma_\pm(t)$. In fact, an explicit function $\rho(\sigma_\pm)$ is needed to investigate and solve the dynamics, which we will develop here. We consider the planar and homogeneous chargeable solid surface discussed above in contact with a bulk solvent with permittivity ε and temperature T with a three-component $1:1:z$ electrolyte of bulk concentrations $\rho_\mathrm{s} : (\rho_\mathrm{s} - z\rho_\mathrm{b}) : \rho_\mathrm{b}$. For convenience we assume trace amounts of reactive ions and therefore set $\rho_\mathrm{b} \ll \rho_\mathrm{s}$, where ρ_s is the bulk salt concentration. We also assume the electrolyte volume to be macroscopically large such that ρ_b and ρ_s do not change due to surface charging. Furthermore we assume the charging timescale $\tau_\pm$, which remains to be derived, to be the slowest timescale of the system. Given that the typical timescale for electric double layer (EDL) equilibration is around $10^{-9}-10^{-6}$ s and that the (geometry and flow dependent) transport timescale for ions in stirred reactors can be as short as 10^{-4} s [120], we find a large window $\tau_\pm \gg 10^{-4}$ s for reactions to be well-described by

our (reaction-limited) theory [121]: for example phosphate desorption showing characteristic reaction timescales of hours [122].

The slow-reaction assumption allows us to describe the EDL within an equilibrium theory, for which we take the Gouy-Chapman solution of Poisson-Boltzmann (PB) theory for simplicity [10, 95]. Although PB theory is based on a mean-field assumption for a system of point ions, it is known that for all but the highest salt concentrations this theory is quite accurate for $1:1$ and even $1:2$ aqueous electrolytes [123], and we expect a similar accuracy for $1:1:z$ electrolytes in the limit $\rho_b \ll \rho_s$ of our interest. Within these assumptions the concentration of reactive ions at the surface is determined by a Boltzmann distribution $\rho(\sigma_\pm) = \rho_b \exp[-z\phi(\sigma_\pm)]$, where $k_B T\phi(\sigma_\pm)/e$ is the electric potential at the surface with a surface charge $\pm ze\sigma_\pm$, with k_B the Boltzmann constant. For desorptive charging the surface and ions have opposite charge and hence $z\phi(\sigma_-) < 0$, while for adsorptive charging ions and surface have the same sign yielding $z\phi(\sigma_+) > 0$. With this observation the Gouy-Chapman solution for a $1:1$ electrolyte, which is relevant here as $\rho_s \gg \rho_b$, gives $\phi(\sigma_\pm) = \pm 2\sinh^{-1}(z\sigma_\pm/\sigma^*)$ [10, 95], where $\sigma^* = (2\pi\lambda_B\lambda_D)^{-1}$ with $\lambda_B = e^2(4\pi\varepsilon k_B T)^{-1}$ the Bjerrum length of the solvent and $\lambda_D = (8\pi\lambda_B\rho_s)^{-\frac{1}{2}}$ the Debye screening length. Substituting the Gouy-Chapman potential in the Boltzmann factor yields

$$\rho(\sigma_\pm) = \rho_b \exp[-z\phi(\sigma_\pm)] = \rho_b \left(\frac{z\sigma_\pm}{\sigma^*} + \sqrt{1 + \left(\frac{z\sigma_\pm}{\sigma^*}\right)^2} \right)^{\mp 2z}, \qquad (3.3)$$

where the exponent is positive for desorptive charging and negative for adsorptive charging. Because Eq. (3.3) is reaction-mechanism dependent, explicit information on the charging mechanism can be deduced from the reaction kinetics as described by combining Eq. (3.3) with Eqs. (3.2a)-(3.2b).

3.4 Non-linear kinetics

In order to investigate the influence of the Coulombic ion-surface interactions on the charging dynamics, we numerically solve $\sigma_-(t)$ from the kinetic Langmuir-Gouy-Chapman Eqs. (3.2a) and (3.3). The symbols in Fig. 3.1(a) present the resulting relative deviations from equilibrium, $s_-(t) - 1$, for a desorptive reaction in the experimentally common case of low equilibrium saturation $\sigma_{-,eq} \ll \Gamma$, both for $s_-(t=0) = 2$ and 0.01 corresponding to a surface with double the charge compared to equilibrium and an initially almost uncharged surface, respectively, for equilibrium surface potentials of 50 mV ($|\phi_{eq}| = 2$, circles) and 100 mV ($|\phi_{eq}| = 4$, crosses) and for valencies $z = 0, 1, 2, 3$ indicated by the different colours. Fig. 3.1(a) shows that a desorptive surface that is overcharged ($s_- > 1$) decays to equilibrium faster than one that is undercharged ($s_- < 1$), the more so for larger

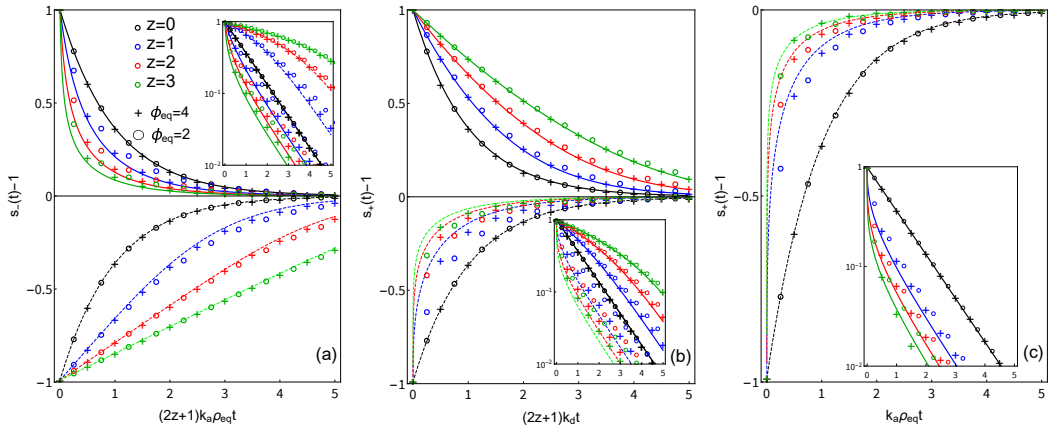

Figure 3.1: Time-dependent relative deviations $s_\pm(t)-1$ from the equilibrium charge density as follows from the kinetic Langmuir-Gouy-Chapman Equations (3.2a-3.3) for equilibrium zeta potentials $|\phi_{eq}|$ equal to 50 mV (cross) and 100 mV (circle) for valencies $z=0,1,2,3$ (colors), in (a) $s_-(t)$ for desorptive reactions when $\sigma_{-,eq}\ll\Gamma$, in (b) $s_+(t)$ for adsorptive reactions when $\sigma_{+,eq}\ll\Gamma$ and in (c) $s_+(t)$ for adsorptive reactions when $\sigma_{+,eq}\simeq\Gamma$. Insets denote semi-logarithmic representations of $|s_\pm(t)-1|$. The case for $\sigma_{-,eq}\simeq\Gamma$ (not shown) is trivial with single-exponential decay for all z.

valencies z. Interestingly, the sorption of uncharged species ($z=0$, black symbols) reveals perfect symmetry between the two cases as expected for first order kinetics, which is also manifest in the semi-logarithmic representation of $|s_-(t)-1|$ in the inset of Fig. 3.1(a) that shows a data collapse and a single-exponential decay for $z=0$. For $z\geq 1$ the inset reveals a non-exponential time dependence with an initially slower decay for undercharged surfaces and an initially faster decay for overcharged surfaces, the difference becoming more pronounced for higher valencies. Fig. 3.1(b) shows the deviation $s_+(t)-1$ from numerical solutions of Eqs. (3.2b)-(3.3) for an adsorptive charging reaction and the same low equilibrium areal density $\sigma_{+,eq}\ll\Gamma$ and the same surface potentials and valencies as in (a). Interestingly, for this reaction the relaxation of an initially undercharged surface to equilibrium is faster, rather than slower as we found for desorptive undercharged surfaces in (a). Hence the two mechanisms can be distinguished by inspecting a single time-trace of the surface charge.

We do not plot the dynamics of a desorptive surface that is saturated in equilibrium $\sigma_{-,eq}\simeq\Gamma$ (in which case $k_d\gg k_a\rho_{eq}$) as the equilibration (desorption) rate for such a surface $\partial_t s\simeq -k_d(s-1)$ is linear and equilibration occurs through trivial single-exponential decay. The lack of non-linearity for such a surface stems from the fact that the desorption process is unaffected by the electrostatic surface-ion interaction. However, as can be seen in Fig. 3.1(c) the dynamics of an adsorptively charged surface with a saturated charge density $\sigma_{+,eq}\simeq\Gamma$ is markedly non-linear.

As was the case in Fig. 3.1(b) we see that an undercharged surface equilibrates faster than a single-exponential. Clearly, these rather distinctive features of the time-dependent surface charge contain explicit information on not only the reaction mechanism but also the valency of reacting ions.

In Figs. 3.1(a)-(b) the dimensionless time on the horizontal axes contains a factor $(2z+1)$, which as we will show now, is convenient as it leads to a data collapse in the asymptotic nonlinear-screening regime $|\phi_{\rm eq}| \gg 1$ where $s_\pm(t)$ only depends on the valency, the reaction mechanism, and the initial charge state. To see why the near-equilibrium decay rate includes a factor $2z+1$ in Figs.3.1(a) and (b) but not (c) we simplify the Langmuir-Gouy-Chapman Eqs. (3.2a)-(3.2b) and (3.3) in the important and common case of large equilibrium surface potentials where $z\sigma/\sigma^* > 1$, say beyond 50 mV where $|\phi_{\rm eq}| \geq 2$. In this limit Eqs. (3.2a)-(3.2b) can be rewritten as a single polynomial (Chini [124]) differential equation

$$-\partial_t s_\pm = k_{\rm a}\rho_{\rm eq}\left(s_\pm^{1\mp 2z} - s_\pm^{-z\mp z}\right) + k_{\rm d}\left(s_\pm - s_\pm^{-z\mp z}\right), \tag{3.4}$$

for which a closed form solution can be obtained by separation of variables only for an adsorptively charged surface with $k_{\rm d} \gg k_{\rm a}\rho_{\rm eq}$ in which case $s_+^{2z+1}(t) = 1 + (s_+^{2z+1}(0) - 1)\exp[-(2z+1)k_{\rm d}t]$. Near-equilibrium, $s_\pm \simeq 1$, Eq. (3.4) simplifies to the linear differential equation $\partial_t s_\pm \simeq -(s_\pm - 1)/\tau_\pm$ with the near-equilibrium decay rate for desorptive and adsorptive charging given, respectively, by

$$\tau_-^{-1} = (2z+1)k_{\rm a}\rho_{\rm eq} + k_{\rm d}, \tag{3.5a}$$

$$\tau_+^{-1} = (2z+1)k_{\rm d} + k_{\rm a}\rho_{\rm eq}. \tag{3.5b}$$

As announced, this timescale $\tau_\pm$ shows that electrostatic attraction can alter the linear near-equilibrium decay rate by a factor $2z+1$ for $z \geq 1$ compared to the neutral case ($z = 0$) in the experimentally common regime $(k_{\rm a}\rho_{\rm eq}/k_{\rm d})^{\mp 1} \gg 1$ where $\sigma_{\pm,{\rm eq}} \ll \Gamma$. Molecular dynamics simulations such as those in Ref. [101, 125–127] will not capture this factor unless the entire electric double layer is resolved. As for the majority of surfaces the equilibrium charge is much lower than saturation, $\sigma_{\rm eq} \ll \Gamma$ [119], we expect the correction by a factor $(2z+1)$ to be common and we note in passing that the only other work accounting for Coulombic ion-surface interactions described in Ref. [110, 111] does not mention this factor.

As already observed in Fig. 3.1, our simple Eq. (3.4) shows that far-from-equilibrium the dynamics becomes non-linear and importantly the $\pm$ sign of the reaction mechanism breaks the near-equilibrium symmetry of dynamics with regard to a charge excess or a charge deficit. Desorptively charged surfaces which are overcharged, $s_- > 1$, will initially attract an excess of reactive ions to the

surface, thereby having an increased reaction rate compared to uncharged equilibration. Hence the equilibration for large overcharging is faster than expected from uncharged Langmuir kinetics. Conversely, an initially undercharged surface, $s_- < 1$, will have a shortage of reactive ions and thus equilibration will be slower. For adsorptively charged surfaces equilibration will be non-linear regardless of $\sigma_{\text{eq}}/\Gamma$ and here undercharging leads to a shortage of reactive ions compared to equilibrium and hence faster equilibration, as can be seen in Fig. (3.1b).

3.5 Autocatalytic kinetics

The rate changing during equilibration is reminiscent of autocatalytic reactions where the equilibration rate changes because a catalyst speeding up the reaction is produced simultaneously with a reaction product [41, 128, 129], and in the Appendix we demonstrate the similarity between Eq. (3.4) and autocatalytic kinetics. Such kinetics is interesting as its rich dynamics allows for limit cycles [130, 131] and pattern formation [131–133] and is associated with the origin of life [134, 135]. For surface charging the autocatalytic feedback is not established by a chemical reaction cycle but rather by the electrostatic interactions between the ions and the charged surface changing the reactant concentration over the course of a reaction. As the reaction rate $k_{\text{a}}\rho$ scales positively with concentration such electrostatic feedback is autocatalytic, and in the Appendix we make this similarity explicit. A characteristic feature of such autocatalytic reactions is an increasing decay rate up to a maximum and a corresponding inflection point in the time-dependent decay. Inspecting Eq. (3.4) we find for adsorptively charged surfaces saturated at equilibrium, $\sigma_{+,\text{eq}} \approx \Gamma$, a maximum decay rate and a corresponding inflection point at $s = 2z/(2z-1) > 1$ for $z > 1/2$, however this inflection point is not physically realizable as it is not possible to overcharge an already saturated surface.

Interestingly, for so-called ion displacement reactions in which ions are involved in both the forward- and the back-reaction, inflection points are easily physically realisable as there are now two ions attracted or repelled from the charged surface such that the Coulombic feedback is strengthened: inflection points are hence a smoking gun that multiple ions are involved in a charging reaction. An example of a two-ion reaction where all reacting ions are repelled from the charged surface is the calcium charging of silica [112] of Eq. (3.6a), while an example of a reaction where all the reacting ions are attracted to the charged surface is the

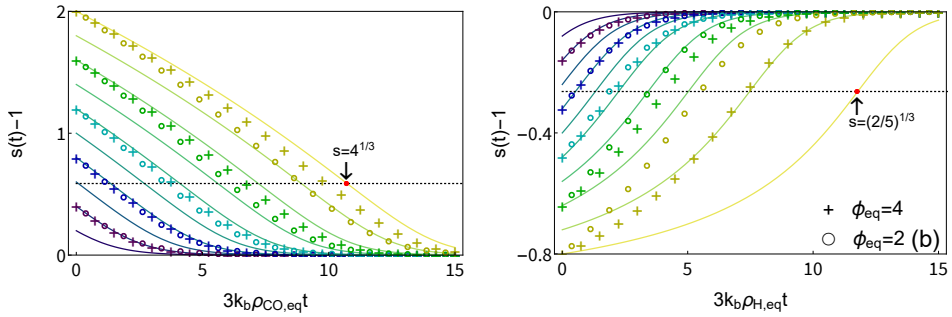

Figure 3.2: Time dependence of the relative deviation from the equilibrium charge density $s(t)-1$ for the autocatalytic ion displacement reaction Eq. (3.7a) and Eq. (3.7b) for 10 different initial conditions $s(0)$ in the experimentally common regime $\sigma_{\rm eq} \ll \Gamma$. Symbols are numerical solutions for the full Langmuir-Poisson-Boltzmann equation (Appendix) for $\phi_{\rm eq} = 2$ (open symbols) and $\phi_{\rm eq} = 4$ (crosses), for 5 initial conditions. Gray dashed line denotes the inflection point (top $s(t)-1 \simeq 0.6$, bottom $s(t)-1 \simeq -0.25$).

fluoride charging of the biomineral carbonato-apatite [136] of Eq. (3.6b),

$$\mathrm{SiOH_{(s)}} + \mathrm{Ca^{2+}_{(aq)}} \underset{k_{\rm b}\rho_{\rm H}}{\overset{k_{\rm f}\rho_{\rm Ca}}{\rightleftharpoons}} \mathrm{SiOCa^{+}_{(s)}} + \mathrm{H^{+}_{(aq)}}, \tag{3.6a}$$

$$\mathrm{XCO_{3\,(s)}} + \mathrm{F^{-}_{(aq)}} \underset{k_{\rm b}\rho_{\rm CO}}{\overset{k_{\rm f}\rho_{\rm F}}{\rightleftharpoons}} \mathrm{XF^{+}_{(s)}} + \mathrm{CO_3^{2-}_{(aq)}}, \tag{3.6b}$$

where $\mathrm{X} = \mathrm{Ca_{10}(PO_4)_6}$, $k_{\rm f}$ is the forward (charging) reaction rate, $k_{\rm b}$ is the backward (decharging) rate and ρ_i is the concentration of ion species i at the charged surface. In the Appendix we derive under the same Gouy-Chapman and large surface potential conditions of the main text that the charge equilibration for Eq. (3.6a) and Eq. (3.6b) are respectively described by

$$-\partial_t s = k_{\rm f}\rho_{\rm Ca,eq}(s^{-3} - s^{-4}) + k_{\rm b}\rho_{\rm H,eq}(s^{-1} - s^{-4}), \tag{3.7a}$$

$$-\partial_t s = k_{\rm f}\rho_{\rm F,eq}(s^{3} - s^{2}) \qquad + k_{\rm b}\rho_{\rm CO,eq}(s^{5} - s^{2}), \tag{3.7b}$$

with the resulting near-equilibrium decay constant $\tau = k_{\rm f}\rho_{i,\rm eq} + 3k_{\rm b}\rho_{j,\rm eq}$ for both reactions and here $\rho_{i,j}$ is the concentration of the forward and backward reacting ion respectively. Comparing Eqs. (3.7a)-(3.7b) to Eq. (3.4) we see that now the time evolution is given by the difference of two polynomials of (non-zero) unequal degree, ensuring that there is always a maximum in the decay rate and hence an inflection point. We find that reactions of the form (3.6b) have two physically realizable inflection points located at $s = 2/3$ (if $\sigma_{\rm eq} \simeq \Gamma$) and $s = (2/5)^{1/3} \simeq 0.75$ (if $\sigma_{\rm eq} \ll \Gamma$): the reaction (3.6a) has only one accessible inflection point $s = 4^{1/3} \simeq 1.6$ (if $\sigma_{\rm eq} \ll \Gamma$), while its second inflection point $s = 4/3$ is inaccessible for a saturated surface with $\sigma_{\rm eq} \simeq \Gamma$.

We plot the dynamics resulting from Eqs. (3.7a)-(3.7b) for a variety of starting conditions $s(0)$ in Fig. 3.2 in the experimentally common limit $\sigma_{\mathrm{eq}} \ll \Gamma$. In Fig. 3.2(a) excellent agreement between the asymptotic Eq. (3.7a) and full numerical results can be seen, while in Fig. 3.2(b) for large undercharging $s(0) < 0.2$ a discrepancy between Eq. (3.7b) and the full numeric solution is found. However in general Eq. (3.7a)-(3.7b) predict the location of the inflection point accurately for a range of common surface potentials $(k_{\mathrm{B}}T/e)|\phi_0| \in [50, 100]$ mV. For ion-displacement reactions of the form (3.6a) and (3.6b) involving ions with higher valencies but monovalent surface charge the inflection point will lie even closer to equilibrium. Thus surfaces that are initially undercharged by only $\simeq 25\%$ or overcharged by $\simeq 60\%$ will generally equilibrate along sigmoidal curves, which is a distinguishing feature that cannot be observed for the single-ion reactions Eqs. (3.1a)-(3.1b). Finally we note that ion-displacement reactions offer a simple explanation for the recently observed sigmoidal equilibration of the surface charge at an aqueous silica interface [41] using only a single charging-reaction of the form Eq. (3.6a) rather than the proposed autocatalytic dissolution cycle involving multiple steps.

3.6 Surface charging kinetics from pressure-jump experiments

While experimental investigations of surface charging kinetics are rare, several kinetic studies employing a pressure-jump technique exist [137, 138]. In such an experiment a mixture of colloidal particles and aqueous electrolytes is slowly pressurized to more than 1 MPa, thereby shifting the surface reactions at the colloidal surface to a high-pressure equilibrium. When this pressure is suddenly released, the solution pressure converges to atmospheric pressure in $\simeq 0.1$ ms. After this jump, the colloidal surface charge must revert from its high-pressure equilibrium to its atmospheric equilibrium. The change in surface charge is measured indirectly, by using the solution conductance as a proxy for the surface charge. While it is unclear what the exact relation between charge and conductance is, a linear relation is often assumed [138].

Of particular interest is a set of experiments where the adsorption of divalent transition metals such as Cu^{2+}, Pb^{2+}, Mn^{2+}, and Co^{2+} onto γ-alumina (Al_2O_3) particles is studied. Here the authors reject the simplest adsorption mechanism, for Cu^{2+} given by

$$\mathrm{AlOH}_{(\mathrm{s})} + \mathrm{Cu}^{2+}_{(\mathrm{aq})} \underset{k_{\mathrm{d}}}{\overset{k_{\mathrm{a}}\rho_{\searrow}}{\rightleftharpoons}} \mathrm{AlOHCu}^{2+}_{(\mathrm{s})}, \tag{3.8}$$

because this single-step reaction does not show single-exponential decay [137]. Their theoretical model used for analysis fixes the surface (zeta) potential, and

hence they find that multiple reactions are needed to explain the observed charge equilibration [137–139]. While their analysis is valid for fixed surface potential, for a potential varying with surface charge we actually expect deviations from single-exponential decay, as shown by Eq. (3.4). The Langmuir-Gouy-Chapman dynamics of the adsorptive reaction (3.8) with $z = 2$ for surface potentials larger than 50 mV is given by

$$-\partial_t s_+ = k_a \rho_{eq}\left(s_+^{-3} - s_+^{-4}\right) + k_d\left(s_+ - s_+^{-4}\right), \tag{3.9}$$

with ρ_{eq} here denoting the equilibrium Cu^{2+} concentration. To test whether the non-linear dynamics observed in the pressure-jump experiment are explained by Eq. (3.9), we extract the experimental data from the relevant pressure-jump experiment for copper adsorption (Fig. 1 in Ref. [137]). In this experiment it is found that the conductivity after the pressure jump decreases and reaches a constant value within 200 ms. In Fig. 3.3 we compare the experimental data (symbols) with equilibration expected from Eq. (3.9) (black line), where we assume the experimentally common case where $\sigma_{eq} \ll \Gamma$ and extract the reaction time $\tau_+ = (5k_d)^{-1} \simeq 27$ ms from the single-exponential, late time, relaxation (green line). As the final equilibrium charge density is not measured in a pressure-jump experiment we use the degree of undercharging $s(0) \simeq -0.6$ as a fit parameter, where we note that an undercharged surface naturally explains why conductivity decreases: during equilibration mobile copper ions are taken out of solution. It can be seen that the difference between the single exponential decay (green) and experimental data (symbols) is large, but that Eq. (3.9) (black) can naturally explain a large part of the deviation from single-exponential decay, without needing to introduce a second reaction with a different timescale.

While further analysis is required to reinstate reaction mechanism (3.8), our analysis shows the importance of taking Coulombic surface-ion interactions into account when considering kinetics. Not only do we show that non-linear decay is readily captured by our model, also the desorption time k_d^{-1} is five times slower than the late-time decay τ_+, in this divalent case. Furthermore, we have demonstrated that chemical information can easily be extracted from a single equilibration curve, even when the initial degree of undercharging is unknown.

3.7 Conclusion

In conclusion, in this Chapter we present a model for the non-linear dynamics of reaction-limited surface charging, combining Langmuir dynamics with Poisson-Boltzmann theory. The model captures how the screened electrostatic surface-ion interaction affects the reaction rate near and far from equilibrium in terms of a non-linear differential equation where the electrostatic interaction is described by only

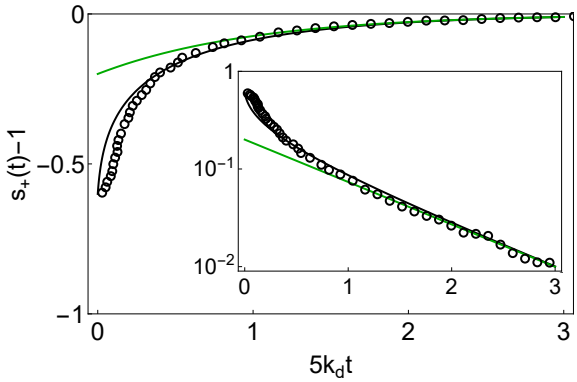

Figure 3.3: Comparison between experimental data from Fig. 1 of Ref. [137] (symbols), single exponential decay (green) and non-linear dynamics (black, Eq. (3.9) with initial degree of undercharging $s(0) - 1 = -0.6$. The reaction time $\tau_+ \simeq 27$ ms is fitted from the late time decay, yielding $k_\mathrm{d}^{-1} \simeq 135$ ms. Inset shows the same data in a semi-logarithmic representation.

using the charge valency of the reactive ion. The Coulombic ion-surface interaction leads to a charge-dependent decay rate, which can be used to gain information on the valency of reacting ions, initial charge, and reaction rate. De- and adsorptive reactions can be distinguished by inspecting whether far-from-equilibrium decay is slower or faster than near-equilibrium decay and we find pressure-jump experiments exhibit features of our model. Interestingly, an inflection point is characteristic for two-ion reactions and we note that such inflection points are also a characteristic feature of autocatalytic reactions. Hence the electrostatic ion-surface interaction can be seen as a catalytic feedback loop. Hence electrostatics offers a straightforward explanation for the recently measured autocatalytic charging of silica [41].

3.8 Appendix

3.8.1 Describing multiple reactions using single-reaction kinetics

The single-reaction (one-pKa) charging reaction presented in this Chapter is a simplified representation for many real liquid-solid interfaces, which often require multiple surface charging reactions for the reproduction of measured equilibrium Langmuir isotherms [13, 93, 97, 117]. In this Appendix we show that for a wide range of conditions a two-reaction model is well approximated by the single-reaction model presented in this Chapter.

Two reaction model For simplicity we will consider a two-reaction (two-pKa) system with two distinct surface-sites labeled $(\mathrm{SiOH})_1$ and $(\mathrm{SiOH})_2$, charged by similar desorptive surface reactions but with different as- and dis-sociation rates

$$(\mathrm{SiOH})_1 \underset{k_{\mathrm{a}1}\rho}{\overset{k_{\mathrm{d}1}}{\rightleftharpoons}} (\mathrm{SiO^-})_1 + \mathrm{H^+}_{(\mathrm{aq})}, \tag{A3.1a}$$

$$(\mathrm{SiOH})_2 \underset{k_{\mathrm{a}2}\rho}{\overset{k_{\mathrm{d}2}}{\rightleftharpoons}} (\mathrm{SiO^-})_2 + \mathrm{H^+}_{(\mathrm{aq})}, \tag{A3.1b}$$

and hence the sites have different equilibrium areal densities $\sigma_{\mathrm{eq},1} \neq \sigma_{\mathrm{eq},2}$ if the site densities Γ_i or equilibrium constants $K_i = k_{\mathrm{a},i}\rho/k_{\mathrm{d},i}$ are unequal. The Langmuir equation describing their charging kinetics is

$$\partial_t \sigma_1 = k_{\mathrm{d}1}(\Gamma_1 - \sigma_1) - k_{\mathrm{a}1}\rho(\sigma_{\mathrm{e}})\sigma_1, \tag{A3.2a}$$

$$\partial_t \sigma_2 = k_{\mathrm{d}2}(\Gamma_2 - \sigma_2) - k_{\mathrm{a}2}\rho(\sigma_{\mathrm{e}})\sigma_2, \tag{A3.2b}$$

with the resulting areal charge density $\sigma_{\mathrm{e}} = \sigma_1 + \sigma_2$ coupling the two reactions. As both reactions have the same reactive ion ($\mathrm{H^+}$) a concentration change $\Delta\rho$ at the surface would cause the equilibrium to shift for both reactions, and the equilibration kinetics resulting after this concentration shift would in principle need to be described by the two coupled non-linear differential equations (A3.2a) and (A3.2b) as they are coupled by the Gouy-Chapman "closure", given by Eq. (3.3) in the main text. However, here we show that if the two reactions have dissimilar equilibrium constants K_i or site densities Γ_i one of the two differential equations can almost always be neglected, as when the equilibrium constants differ so does the shift in equilibrium charge density $\Delta\sigma_i = \sigma_{\mathrm{eq},i}(\rho + \Delta\rho) - \sigma_{\mathrm{eq},i}(\rho)$ for a given concentration shock $\Delta\rho$.

When the difference in equilibrium charge densities of the two sites is very unequal (either $\Delta\sigma_1 \gg \Delta\sigma_2$ or $\Delta\sigma_1 \ll \Delta\sigma_2$) the change in surface charge can be described using a single reaction model (as $\partial_t\sigma_{\mathrm{e}} \simeq \partial_t\sigma_1$ or $\partial_t\sigma_{\mathrm{e}} \simeq \partial_t\sigma_2$). Solving

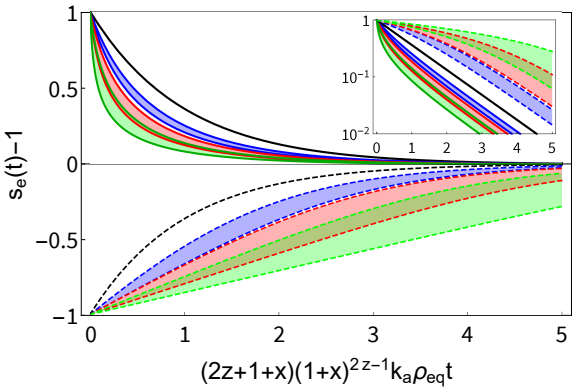

Figure A3.1: Replotting of Fig. 3.1(a) showing charge relaxation for ion valencies $z = 0,1,2,3$ (respectively black, blue, red, green) calculated with curves not originating from Eq. (3.4) in the main text but instead plotted using Eq. (A3.5) with dimensionless static background-charge $x \in [0,1]$. The outermost curves with $x = 0$ revert exactly to those described by Eq. (3.4) in the main text, while curves with $x = 1$ lie significantly closer to the black curve showing single-exponential relaxation, with intermediate x lying in the shaded region. Note that the near-equilibrium decay rate has changed from $(2z+1)k_a\rho_{eq}$ to $(z+1+x)(1+x)^{2z-1}k_a\rho_{eq}$ which for $z = 3$ and $x = 1$ yields a factor 32 difference in the near-equilibrium decay rate. In general however for small x the charging kinetics is well described by the single reaction of Eq. (3.4) in the main text.

for the coupled-Langmuir kinetics Eq. (3.3) in steady-state, $\partial_t \sigma_i = 0$, we find for $\sigma_{i,\mathrm{eq}} \ll \Gamma_i$ that the relative change in the equilibrium surface charge $\Delta\sigma_1/\Delta\sigma_2 \propto (\Gamma_1 K_1)/(\Gamma_2 K_2)$ while for nearly saturated surfaces with $\sigma_{\mathrm{eq}} \approx \Gamma$ the relative shift scales as $\Delta\sigma_1/\Delta\sigma_2 \propto (\Gamma_1 K_2)/(\Gamma_2 K_1)$. As long as $\Delta\sigma_1/\Delta\sigma_2$ deviates significantly from unity, the shift in one of the two equilibrium-densities can be neglected for the shift in the total charge density. To find an explicit maximum bound for which this approximation is valid we calculate the maximum concentration shock $\Delta\rho_{\mathrm{m}} \in \rho[-1,\infty]$ for which this approximation holds by solving for $\Delta\sigma_1/\Delta\sigma_2 = 1$. This has a trivial solution $\Delta\rho = 0$ when $\Gamma_1 = \Gamma_2$ and $K_1 = K_2$ and a non-trivial solution

$$\frac{\Delta\rho_{\mathrm{m}}}{\rho} = \frac{1}{K_1K_2\rho^2}\frac{\Gamma_1K_1\rho - \Gamma_2K_2\rho}{\Gamma_2(1+K_1\rho) - \Gamma_1(1+K_2\rho)} - \frac{\Gamma_1(2+K_2\rho) - \Gamma_2(2+K_1\rho)}{\Gamma_1(1+K_2\rho) - \Gamma_2(1+K_2\rho)}, \tag{A3.3}$$

which simplifies to $\Delta\rho_{\mathrm{m}}/\rho = (K_1K_2\rho^2)^{-1} - 1$ in the case that $\Gamma_1 \simeq \Gamma_2$. In general, the range of validity of Eq. (A3.3) is large when K_1 and K_2 are very unequal, except close to a concentration where $\rho^2 K_1 K_2 = 1$ where $\Delta\rho_{\mathrm{m}}$ tends to zero. Interestingly, in this case the charge density is exactly half-occupied $\sigma_e = (\Gamma_1+\Gamma_2)/2$, which is rare for most experimental conditions. For all other concentrations ρ a very large range $\Delta\rho_{\mathrm{m}}/\rho$ of concentration shocks remains over which a two-

reaction system essentially equilibrates through a single charging reaction. However, while the dynamics will be governed by a single reaction, there will be a static background charge due to which neither σ_1 nor $\sigma_2 \neq \sigma_e$ such that the single reaction is still not exactly equal to the single-reaction kinetics in the main text. That the deviation from the single-reaction kinetics in this Chapter due to this static background charge is minor will be shown in the next paragraph.

Static background charge As the total surface charge density (in units of the elementary charge) is given by $\sigma_e = \sigma_1 + \sigma_2$, the Gouy-Chapman relation (Eq. (3.3)) between the surface occupancy σ_1 and concentration ρ for two reactions now reads

$$\rho(\sigma_1) = \left(\frac{z(\sigma_1+\sigma_2)}{\sigma^*} + \sqrt{1+\left(\frac{z(\sigma_1+\sigma_2)}{\sigma^*}\right)^2} \right)^{2z}. \tag{A3.4}$$

As discussed in the previous section we will now assume that $\Delta\rho \ll \Delta\rho_m$ and without loss of generality we identify $\sigma_{eq,2}$ as the static-charge density ($\Delta\sigma_1/\Delta\sigma_2 \gg 1$) from which follows $\sigma_2 \simeq \sigma_{eq,2}(\rho) \simeq \sigma_{eq,2}(\rho+\Delta\rho) = \text{cnst}$. The non-dimensional change in total surface charge will then be $\partial_t s_e = \partial_t \sigma_e / \sigma_{eq,e} \simeq \partial_t \sigma_1 / \sigma_{eq,e}$ and when $\sigma_{eq,e} \gg \sigma^*$ by combining Eq. (A3.2a) and Eq. (A3.4) we find

$$-\partial_t s_e = k_{d1}(s_e - 1) + k_{a1}\rho_{eq}\left(s_e(s_e+x)^{2z} - (1+x)^{2z}\right), \tag{A3.5}$$

where the dimensionless static surface charge density $x = \sigma_{eq,2}/\sigma_{eq,e} \in [0,1]$ is the ratio of static charge $\sigma_{eq,2}(\rho+\Delta\rho)$ *after* the concentration shock. Interestingly, the near-equilibrium decay rate τ_- is altered from $(2z+1)k_a\rho_{eq}$ to $(2z+1+x)(1+x)^{2z-1}k_a\rho_{eq}$ and hence the deviation from uncharged Langmuir kinetics becomes even larger if the background surface charge is included. Clearly both the timescale and dynamics revert back to the single-reaction kinetics of Eq. (3.4) when $x \ll 1$. To check how much the dynamics is affected at intermediate x we replot Fig.3.1(a) but now with Eq. (A3.5) with $z = 0,1,2,3$ (black, blue, red, green) and $s = 1$ and $s = -0.99$ instead of Eq. (3.4). The resulting shaded regions in Fig. A3.1 represent curves with different $x \in [0,1]$. We observe that for increasing x the dynamics moves closer to single-exponential decay (black line), with this shift being more pronounced for increasing z. However, even for $x = 1$ there is no over-dramatic difference from the single-reaction kinetics as previously explored in this Chapter and in many cases a two-reaction system is well approximated by this single-reaction model. However one should be cautious when extracting the ion valency from dynamics around $x \simeq 1$ as here the dynamics closely resembles that of a single ion with $z-1$. We expect this may occur in processes such as the adsorption of heavy metal ions from ground water which occurs on pre-charged substrates [93]. Under these conditions surface charging can be readily described using Eq. (A3.5).

Summary To summarize, here we have shown that the one-pKa charging reaction is a valid approximation for more complex systems, involving multiple charging reactions, when (i) the ratio of the equilibrium constant K_1/K_2 is not close to unity and (ii) the concentration shock $\Delta\rho$ is constrained within a range $\Delta\rho_{\mathrm{m}}$ which we show to be generally large.

3.8.2 Similarity between surface charging and autocatalysis

Here we will show the similarity between classical autocatalytic kinetics and surface charging as described by Eq. (3.4). First we derive an approximate solution for this Chini differential Eq. (3.4), by expanding it up to second order around $s = 1$ obtaining a Bernoulli differential equation [140]. Solving this equation by standard methods we obtain

$$s_{\pm}(t) - 1 = \frac{(s_{\pm}(0)-1)e^{-t/\tau_{\pm}}}{1 \mp z\left(1-e^{-t/\tau_{\pm}}\right)\left(s_{\pm}(0) - 1 \pm \dfrac{s_{\pm}(0)-1}{(2z+1)(k_{\mathrm{d}}/k_{\mathrm{a}}\rho_{\mathrm{eq}})^{\pm 1}+1}\right)}, \tag{A3.6}$$

where $\tau_{\pm}$ is given by Eq. (3.5b). Our Eq. (A3.6) reverts to single exponential decay when $(s_{\pm}(0)-1)z \ll 1$, and is valid only as long as $\mp z(s_{\pm}(0)-1) \gg -1$. For most practical purposes Eq. (A3.6) is not of much use, however it is interesting to note that a similar solution exists for autocatalytic equations thereby substantiating the claim that surface charging is autocatalytic. To make this comparison explicit we consider the simplest possible autocatalytic reaction (Eq. (1a′) from Ref. [129]),

$$\mathrm{A}_{(\mathrm{aq})} + \mathrm{Y}_{(\mathrm{aq})} \underset{k_{\mathrm{b}}\rho_{\mathrm{Y}}^{q}}{\overset{k_{\mathrm{f}}\rho_{\mathrm{A}}\rho_{\mathrm{Y}}}{\rightleftharpoons}} q\ \mathrm{Y}_{(\mathrm{aq})} \tag{A3.7}$$

where the aqueous reactant $\mathrm{Y}_{(\mathrm{aq})}$ together with reactant $\mathrm{A}_{(\mathrm{aq})}$ produces q copies of itself. The reaction is autocatalytic when the autocatalytic order $q \geq 2$. When the concentration ρ_{A} is constant the production rate of $\mathrm{Y}_{(\mathrm{aq})}$ is given by the Chini differential equation

$$-\partial_t y = k_{\mathrm{f}}\rho_{\mathrm{A}}(y^q - y), \tag{A3.8}$$

with $y = \rho_{\mathrm{Y}}/\rho_{\mathrm{Y,eq}}$, which already shows similarities to Eq. (3.4). To obtain a solvable Bernoulli equation we expand Eq. (A3.8) up to second order around $y = 1$, which has the solution

$$y(t) - 1 = \frac{(y(0)-1)e^{-t/\tau_{\mathrm{y}}}}{1 - \dfrac{q}{2}(y(0)-1)(1-e^{-t/\tau_{\mathrm{y}}})}, \tag{A3.9}$$

with $\tau_{\mathrm{y}} = (q-1)k_{\mathrm{f}}\rho_{\mathrm{A}}$. While Eq. (A3.9) is already very similar to Eq. (A3.6), the similarity becomes even more apparent when comparing the autocatalytic dynamics to the dynamics of an adsorptively charged surface with $\sigma_{+,\mathrm{eq}} \ll \Gamma$ (where

$k_d \gg k_a \rho_{eq}$) in which case Eq. (A3.6) simplifies to

$$s_+(t) - 1 = \frac{(s_+(0)-1)e^{-t/\tau_+}}{1 - z(s_+(0)-1)(1-e^{-t/\tau_+})}. \tag{A3.10}$$

Comparing Eq. (A3.9) with Eq. (A3.10) we find the only difference is the definition of the timescale τ_i and that the ion-valency z replaces the autocatalytic order $q/2$. This correspondence between the ion valency z and autocatalytic order q supports the interpretation that the Coulombic ion-surface interactions acts autocatalytically.

3.8.3 Charging dynamics of ion displacement reactions

Here we will generalize the derivation of Eq. (3.4) from single-ion reactions to two-ion reaction also known as ion-displacement reactions, yielding Eq. (3.7b). We will consider a general form for the single-step ion-displacement reaction where an aqueous ion $A^{\mathcal{Z}_A}_{(aq)}$ displaces from the (uncharged) surface group $SB_{(s)}$ the ion $B^{\mathcal{Z}_B}_{(aq)}$, leaving a charged surface site $SA^{\mathcal{Z}_A-\mathcal{Z}_B}_{(s)}$ combining into the reaction

$$SB_{(s)} + A^{\mathcal{Z}_A}_{(aq)} \underset{k_b\rho_B}{\overset{k_f\rho_A}{\rightleftharpoons}} S^{\mathcal{Z}_A-\mathcal{Z}_B}_{(s)} + B^{\mathcal{Z}_B}_{(aq)}, \tag{A3.11}$$

where $\mathcal{Z}_A$ and $\mathcal{Z}_B$ are the valencies of ad- and desorbing ions A and B, respectively, which contrary to the ion-valency z is not strictly positive as the total charge difference between A and B is important. The resulting charge of the surface groups is given by $\mathcal{Z}_S = \mathcal{Z}_A - \mathcal{Z}_B$, such that the surface charge is $e\sigma\mathcal{Z}_S$. As in the Chapter, the charging dynamics will be described by Langmuir kinetics, which assumes identical and independent surface sites such that

$$\partial_t \sigma = k_A \rho_A(\sigma)(\Gamma - \sigma) - k_B \rho_B(\sigma)\sigma. \tag{A3.12}$$

Note that now both terms contain the non-trivial $\rho(\sigma)$ dependence, which allows for sigmoidal equilibration as discussed in this Chapter. For $\rho_i(\sigma)$ we use the Gouy-Chapman expression

$$\rho_i(\sigma) = \rho_{b,i}\left(\frac{z_S\sigma}{\sigma^*} + \sqrt{1+(\frac{z_S\sigma}{\sigma^*})^2}\right)^{\pm 2z_i}. \tag{A3.13}$$

The exponent for ρ_i is positive when $\mathcal{Z}_i\mathcal{Z}_S < 0$ and negative when $\mathcal{Z}_i\mathcal{Z}_S > 0$. When $\mathcal{Z}_i\mathcal{Z}_S = 0$ the dynamics revert to the single-ion charging reaction. In the high charge limit $|\phi_{eq}| > 2$ (when $z_S\sigma_{eq}/\sigma^* > 1$) we find

$$-\partial_t s = k_A \rho_{A,eq}(s^{1\pm 2z_A} - s^{\pm 2z_A}) + k_B \rho_{B,eq}\left(s^{1\pm 2z_B} - s^{\pm 2z_A}\right), \tag{A3.14}$$

where the $\pm$ sign in front of z_i is negative when $Z_i Z_S > 0$ and positive when $Z_i Z_S < 0$. Substituting $Z_A = +2$ and $Z_B = +1$ (hence $Z_S = +1$) we find Eq. (7a), while substituting $Z_A = -1$ and $Z_B = -2$ (hence $Z_S = +1$) yields Eq. (7b). Furthermore, for $Z_A = 0$ this equation reverts to desorptive charging and for $Z_B = 0$ this equation reverts to adsorptive charging. The presented derivation can be naturally extended to single-step reactions involving an arbitrary number of charged species.

Chapter 4

Pressure-sensitive ion conduction in a conical channel: optimal pressure and geometry

Abstract

We theoretically investigate the electric conductivity of a conical channel, which in accordance with recent experiments exhibits a strong nonlinear pressure dependence. This mechanosensitive diodic behavior stems from the pressure-sensitive build-up or depletion of salt in the pore. We find that optimal diodic behavior is achieved when the tip and base radii of the cone have a ratio of 0.22 and for a pressure drop where the fluid flow vanishes. This optimal pressure drop is proportional to the inverse square of the tip radius, explaining the dramatic mechanosensitivity observed in experiments.

This Chapter is based on the publication

W.Q. Boon, T. E. Veenstra, M. Dijkstra, M, & R. van Roij, (2022). *Pressure-sensitive ion conduction in a conical channel: optimal pressure and geometry*. Physics of Fluids, 34(10), 101701.

There are paragraphs and figures that are taken or modified from the above-mentioned publication and its supporting information. The co-authors gave their permission for the reproduction. The author contributions to this publication are as follows:

W.Q.B.: Conceptualization (equal); Formal analysis (equal); Investigation (equal); Visualization (lead); Writing - original draft (lead); Writing - review & editing (lead). T.E.V.: Data curation (lead); Formal analysis (equal); Investigation (equal); Visualization (supporting); Writing - original draft (supporting). M.D.: Funding acquisition (lead); Project administration (lead); Supervision (lead); Writing - review & editing (equal). R.v.R.: Funding acquisition (lead); Project administration (lead); Supervision (lead); Writing - review & editing (equal). W.Q.B. and T.E.V contributed equally.

4.1 Introduction

A fluidic channel allows for the simultaneous transport of solvent, charge, and dissolved salt when connected to two liquid electrolyte reservoirs at different pressures, voltages, salt concentrations, and/or temperatures. Such ionic transport is not only interesting from a fundamental point of view, but also for energy harvesting [141–144], desalination [145, 146] and microfluidic applications [33, 147]. In all these devices fluidic channels with dimensions in the nano- and micrometer regime are used [148–150], a size range where the influence of surface charge on transport becomes significant due to the relatively large surface-to-volume ratio. This surface charge is key to electrokinetic transduction phenomena such as the flow of electrolyte by an electric potential drop (electro-osmosis) or the electric (streaming) current induced by flow due to an applied pressure drop [40, 44, 151]. While these electrokinetic transduction phenomena have long been understood [152], at least in simple channel geometries, in conical pores exotic transport behavior such as electro-osmotic flow inversion [153–155] and current rectification [156–162] have been observed. Such non-linear transport behavior makes conical pores uniquely attractive for biochemical sensing [163–166] and neuromorphic applications [167–169].

Outline In this Chapter, we analyse the intricate case of a micron-sized cone-shaped channel exposed to a simultaneous pressure and electric potential drop (as depicted in Fig. 4.1) by means of the well-known Poisson-Nernst-Planck-Stokes equations (1.15)-(1.18). We will show that the ionic current in conical nanopores can be either strongly reduced or enhanced by a pressure difference and concomitant flow, resulting into an extremely mechano-sensitive ionic diode similar to those present in cell membranes [170, 171], which can also be used to optimize power generation [172]. Recent experiments revealed such a non-linear pressure-induced electric transport in conical pores even at micrometer length scales [173]. It was found that the electric current $I(\Delta P, \Delta\psi)$ due to an applied potential difference $\Delta\psi$ is very sensitively dependent on the applied pressure drop ΔP over the channel. Surprisingly, the observed pressure dependence of the electric conductance occurred at extremely low rather than high pressures. For conical pores it was already observed that, for $\Delta P = 0$, the response of the current I is asymmetric with regard to the sign of $\Delta\psi$ [156–162]. This so-called current rectification is typically attributed to concentration polarisation [156–162]. Here we will show that the flow (and hence pressure)-sensitive conductivity for $\Delta P \neq 0$ can also be understood by the concentration-polarisation, while others argue that novel mechanisms are needed such as a bulk space-charge [173] or a non-linear streaming current [172]. Such a flow sensitivity was previously noted in numerical calculations, which however ignored electro-osmotic flow [174]. Whether electro-osmotic flow

can [175–177] or cannot [178–180] be ignored is debated in the literature. We reconcile these two opposing views by showing that the importance of flow depends on Péclet number; in the small Péclet regime [175] flow can be ignored while in the large Péclet regime [178] it is important. In general for large micrometer channels [161, 162, 173, 181, 182] flow can be expected to be important, while in the theoretical description of such systems [183, 184] flow is often ignored.

4.2 Theoretical framework

We consider two reservoirs of an aqueous 1:1 electrolyte in the two half spaces $x < 0$ and $x > L$ connected by an axially-symmetric cone-shaped channel of length L as depicted in Fig. 4.1. Here x is the cartesian coordinate along the symmetry axis; the radial coordinate is r. The channel has a wide base radius $R_\mathrm{b} \ll L$ at $x = 0$ and a narrow tip radius $R_\mathrm{t} \leq R_\mathrm{b}$ at $x = L$. The radius of the channel for $x \in [0, L]$ reads $R(x) = R_\mathrm{b} - (x/L)(R_\mathrm{b} - R_\mathrm{t})$. The channel wall at $r = R(x)$ carries a uniform negative surface charge density $e\sigma$, with e the proton charge. The two reservoirs both contain an identical aqueous 1:1 electrolyte with viscosity η, ionic diffusion coefficient D, dielectric permittivity ε, and total ionic bulk concentration $2\rho_\mathrm{b}$. Thus, asymptotically far from the channel, at either side $|x|/L \gg 1$, the local cation concentration $\rho_+(x,r)$ and anion concentration $\rho_-(x,r)$ are both equal to ρ_b.

Inspired by the experiments of Ref. [173] we consider an applied pressure drop ΔP and a simultaneous electric potential drop $\Delta\psi$ across the channel. These steady driving forces give rise to a potential $\psi(x,r)$ and a pressure excess $P(x,r) - P_0$

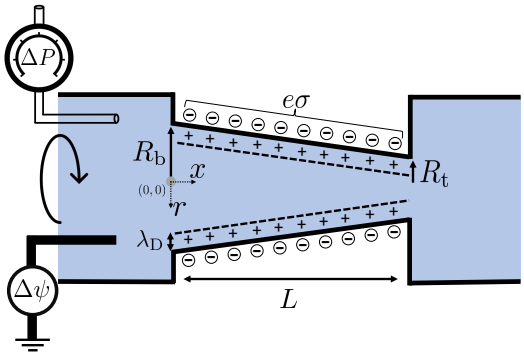

Figure 4.1: Schematic of an axially symmetric conical channel of length L, base radius R_b at $x = 0$, and tip radius $R_\mathrm{t} \leq R_\mathrm{b}$ at $x = L$. The channel connects two bulk 1:1 electrolytes in the half spaces $x < 0$ and $x > L$. The channel wall carries a negative surface charge density $e\sigma$ that induces an electric double layer of thickness λ_D, the Debye length. Volume, charge, and salt ions are transported through the channel by an applied potential drop $\Delta\psi$ and pressure drop ΔP.

which vanish in the bulk phase $x \gg L$ and are equal to $\Delta\psi$ and ΔP, respectively, for $x \ll -L$, where P_0 is an arbitrary reference pressure. They drive a fluid flow with velocity $\mathbf{u}(x,r)$ and ionic fluxes $\mathbf{j}_\pm(x,r)$, leading to nontrivial concentration profiles $\rho_\pm(x,r)$. In the Appendix we present the standard Poisson-Nernst-Planck-Stokes (PNPS) equations and the blocking and no-slip boundary conditions. Together with Gauss' law for the surface charge, they form a closed set for $\mathbf{u}$, ψ, $\mathbf{j}_\pm$, and $\rho_\pm$. Convenient linear combinations are the total salt concentration $\rho_s = \rho_+ + \rho_-$, the charge density $e\rho_e = e(\rho_+ - \rho_-)$, and the associated fluxes $\mathbf{j}_s = \mathbf{j}_+ + \mathbf{j}_-$ and $\mathbf{j}_e = \mathbf{j}_+ - \mathbf{j}_-$. In equilibrium, i.e. for vanishing ΔP and $\Delta\psi$, all fluxes vanish and the PNPS equations describe an Electric Double Layer (EDL) with an excess of cations and a depletion of anions close to $r = R(x)$ such that the negative surface charge is compensated [185]. The thickness of the EDL is given by the Debye length $\lambda_D = \sqrt{\varepsilon k_B T/2e^2\rho_b} = 10$ nm for the case $\rho_b = 1$mM that we consider.

Inspired by the experimental conditions of Ref. [173], the focus of this Chapter will be on the long-channel thin-EDL limit with $L \gg R_b \geq R_t \gg \lambda_D$ such that EDL-overlap does not play a role. This is in contrast to a large body of literature on non-linear transport in cone-shaped channels, where overlap of the EDL is a key ingredient for current rectification and diodic behavior [156–158]. We will show that the conical geometry combined with simultaneous pressure- and potential-induced transport leads to an x-independent volumetric flow rate $Q = 2\pi\hat{\mathbf{x}} \cdot \int_0^{R(x)} \mathbf{u}(x,r) r\mathrm{d}r$ and electric current $I = 2\pi e\hat{\mathbf{x}} \cdot \int_0^{R(x)} \mathbf{j}_e(x,r) r\mathrm{d}r$ that satisfy an Onsager-like relation

$$\begin{pmatrix} Q \\ I \end{pmatrix} = \frac{\pi R_b R_t}{L} \begin{pmatrix} \mathbb{L}_{11} & \mathbb{L}_{12} \\ \mathbb{L}_{21} & \mathbb{L}_{22}(\Delta P, \Delta\psi) \end{pmatrix} \begin{pmatrix} \Delta P \\ \Delta\psi \end{pmatrix}. \tag{4.1}$$

We set out to calculate all elements of the transport matrix $\mathbb{L}$ analytically, not only the permeability $\mathbb{L}_{11}$ and the electro-osmotic mobility $\mathbb{L}_{12} = \mathbb{L}_{21}$, but also the electric conductance $\mathbb{L}_{22}$ that, as we will see, strongly depends on the applied pressure-and voltage drop -in agreement with experiments [173]. This pressure sensitivity is due to highly nontrivial ion concentration profiles that vary on length scales of the channel dimensions, as follows from our analytic expression obtained from the PNPS equations. From this we will find that optimal current rectification requires not only a pressure drop $\Delta P^* = -\mathbb{L}_{12}\Delta\psi/\mathbb{L}_{11}$ (such that $Q = 0$) but also a universal optimal geometry with $R_t/R_b \simeq 0.22$.

4.3 Fluidic mobility

We solve the PNPS equations for a wide variety of system parameters and show illustrative examples for the standard parameter set inspired by Ref. [173] with

tip radius $R_t = 0.17\mu$m, channel length $L = 10\mu$m, base radius $R_b = 1.04\mu$m, viscosity $\eta = 1$ mPas, relative dielectric constant 80, ionic diffusion coefficient $D = 1$ nm^2/ns, and surface charge $e\sigma = -0.02e/$ nm^2, which gives at $\rho_b = 1$mM a zeta potential of $\psi_0 = -40$mV corresponding to a silica surface in contact with an aqueous 1:1 electrolyte [112]. In line with the Stokes equation we find $\mathbf{u}(x,r)$ to contain essentially two contributions. (i) A pressure drop on its own induces a Poiseuille-like flow that is directed towards the (virtual) vertex of the cone for $\Delta P > 0$, or away from it for $\Delta P < 0$ [186–188]. Its contribution $Q_P \equiv (\pi R_b R_t/L)\mathbb{L}_{11}\Delta P$ to Q is independent of x and can be obtained analytically [186–188] to yield $\mathbb{L}_{11} = R_b^2 R_t^2/8\eta\langle R^2\rangle$, where the angular brackets denote a lateral average $\langle R^2\rangle = \int_0^L R^2(x)\mathrm{d}x/L = (R_b^2 + R_t^2 + R_b R_t)/3$. The excellent agreement between the pressure-drop dependence of our linear expression for Q_P and our numerically obtained value of Q at $\Delta\psi = 0$ is shown in Fig. A4.1(a) of the Appendix. (ii) For our negative surface charge the potential drop $\Delta\psi$ on its own induces an electro-osmotic plug-like flow towards the tip of the cone for $\Delta\psi > 0$, or away from the tip for $\Delta\psi < 0$. We are not aware of an explicit expression in the literature for $\mathbb{L}_{12}$ that characterizes the electro-osmotic flow rate $Q_\psi \equiv (\pi R_b R_t/L)\mathbb{L}_{12}\Delta\psi$ in a conical pore. Here we derive an explicit expression for $\mathbb{L}_{12}$, which first requires an expression for the cross-sectional averaged electric field $-\partial_x\bar{\psi}(x)$. This averaged electric field has to be proportional to the inverse of the cross-section $\pi R^2(x)$ in order to be divergence free. The proportionality constant follows, in the long-channel limit, from the condition that $\int_0^L \partial_x\bar{\psi}(x)\mathrm{d}x = -\Delta\psi$. This yields

$$\partial_x\bar{\psi}(x) = -\frac{\Delta\psi}{L}\frac{R_b R_t}{R^2(x)}, \tag{4.2}$$

which compares well to the numerical results, as illustrated in Fig. (A4.2) in the Appendix. Using the standard electro-osmotic mobility $\mathbb{L}_{12} = -\varepsilon\psi_0/\eta$ for a cylinder [189], but now with our laterally varying electric field and radius, we obtain $Q_\psi = \pi R^2(x)(-\varepsilon\psi_0/\eta)\partial_x\bar{\psi}(x)$ which with Eq. (4.2) is independent of x and hence represents a valid divergence-free solution for the stationary state. In Fig. A4.1(b) of the Appendix we compare this expression for Q_ψ as a function of $\Delta\psi$ with numerical calculations. The agreement is good, although minor deviations on the order of $\sim 10\%$ are visible which we attribute to the approximate nature of our $\mathbb{L}_{12}$.

4.4 Non-linear conductance

With the permeability $\mathbb{L}_{11}$ and electro-osmotic mobility $\mathbb{L}_{12}$ established, we continue with the electric conductance $\mathbb{L}_{22}$, for which the total ion concentration $\rho_s(x,r)$ is expected to play a major role. In our numerical calculations we find weak radial variation of $\rho_s(x,r)$ outside the EDL-vicinity $r \simeq R(x)$, in agree-

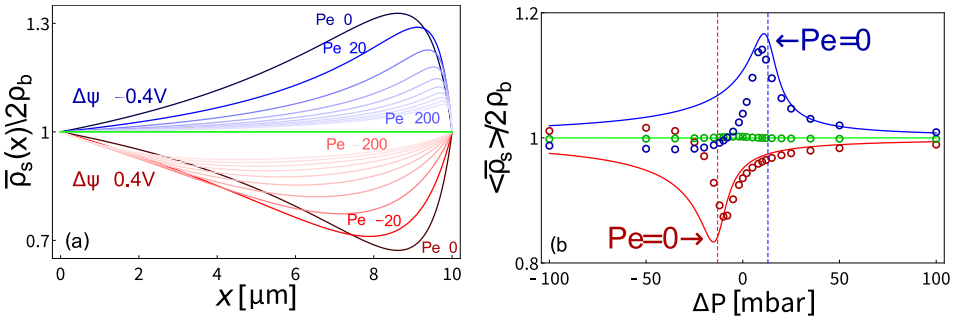

Figure 4.2: (a) Cross-sectional averaged salt concentration $\bar{\rho}_s(x)$ normalized by the bulk concentration $2\rho_b$ as a function of the lateral position x for our standard parameter set (see text). For potential drops $\Delta\psi = +0.4$V (red) and -0.4V (blue), for which $\Delta\rho = \mp 31$mM according to Eq. (4.5), the solid lines represent concentration profiles at Péclet numbers that vary between 0 and ∓ 200 in steps of 20. The green curve represents the case $\Delta\psi = 0$V at any Pe. (b) The normalized laterally averaged concentration $\langle\bar{\rho}_s\rangle/2\rho_b$ as a function of the pressure drop ΔP at potential drops $\Delta\psi = +0.4$V (red), -0.4V (blue), and 0V (green). Solid lines represent Eq. (4.4), data points are from numerical solutions to the full PNPS equations, which for $\Delta\psi = \pm 0.4$V show an extremum very close to $\Delta P^* = \mp 13$mbar from Eq. (4.6) where Pe=0, denoted by the vertical dashed lines.

ment with Ref. [174]. Hence within the thin-EDL limit this implies that the cross-sectional averaged concentration $\bar{\rho}_s(x)$ is a good proxy for the salt concentration at axial position x. If we now define the total salt flux as $J(x) = 2\pi\hat{\mathbf{x}} \cdot \int_0^{R(x)} \mathbf{j}_s(x,r) r dr$ we can insert the diffusive, conductive, and advective contributions of $\mathbf{j}_s$ as given by the PNPS equations in the Appendix to rewrite the stationarity condition $\partial_x J(x) = 0$ for $x \in [0, L]$ as

$$D\partial_x \left(\pi R^2(x) \partial_x \bar{\rho}_s(x) - 2\pi R(x) \sigma \frac{e\partial_x \bar{\psi}}{k_B T} \right) - Q\partial_x \bar{\rho}_s(x) = 0. \tag{4.3}$$

Here we use the radial independence of $\rho_s(x,r)$ and $\psi(x,r)$ in the thin-EDL limit as well as the slab-neutrality condition $2\pi \int_0^{R(x)} \rho_e(x,r) r dr = -2\pi R(x)\sigma$. The slab neutrality condition is an important difference with the analysis presented in Ref. [173], where it was suggested that a bulk space charge is of key importance for understanding the observed mechano-sensitivity of conical pores. For a given ΔP and $\Delta\psi$ we consider Q and $\partial_x \bar{\psi}(x)$ known from Eqs. (4.1) and (4.2), respectively, such that Eq. (4.3) is an ordinary second-order differential equation for $\bar{\rho}_s(x)$; together with its solutions presented below it constitutes the key result of this Chapter. An important role will be played by the conductive contribution $J_{cond}(x)$ to J given by $J_{cond}(x) = -2\pi D\sigma(e\Delta\psi/k_B T) R_b R_t / R(x) L$, which varies with x in a conical channel and thus acts as a source or sink term in Eq. (4.3) that sucks ions into the channel for $\Delta\psi < 0$ and pushes them out for $\Delta\psi > 0$. Given the long-channel limit of interest and the equal salinity of both reservoirs, we solve

Eq. (4.3) with boundary conditions $\bar{\rho}_s(0) = \bar{\rho}_s(L) = 2\rho_b$, resulting in

$$\bar{\rho}_s(x) - 2\rho_b = \frac{\Delta\rho}{\mathrm{Pe}}\left[\frac{x}{L}\frac{R_t}{R(x)} - \frac{\exp\left(\frac{x}{L}\frac{R_t^2}{R_b R(x)}\mathrm{Pe}\right) - 1}{\exp\left(\frac{R_t}{R_b}\mathrm{Pe}\right) - 1}\right] \tag{4.4}$$

$$= \begin{cases} \frac{\Delta\rho}{2}\frac{x}{L}\left(1-\frac{x}{L}\right)\frac{R_t^2}{R^2(x)} & \text{if } |\mathrm{Pe}| \ll \left(\frac{R_b}{R_t}\right)^2; \\ \frac{\Delta\rho}{2|\mathrm{Pe}|}\left(\frac{R_b}{R(x)}\left(1-\frac{x}{L}(1+\frac{R_t}{R_b})\right)\mp 1\right) & \text{if } \pm\mathrm{Pe} \gg \left(\frac{R_b}{R_t}\right)^2. \end{cases}$$

Here we not only introduced the tip Péclet number $\mathrm{Pe} \equiv QL/D\pi R_t^2$ with $Q(\Delta P, \Delta\psi)$ given by Eq. (4.1) but also a measure for the concentration inhomogeneity

$$\Delta\rho \equiv \frac{2(R_b - R_t)\sigma}{R_t^2}\frac{e\Delta\psi}{k_B T}, \tag{4.5}$$

thus $\Delta\rho = 0$ if $R_b = R_t$ and hence $\bar{\rho}_s(x) = 2\rho_b$ in this case.

Note that both Pe and $\Delta\rho$ have a sign, and that the dependence on the potential drop is not only accounted for by $\Delta\rho$ but also by Pe through the electro-osmotic contribution to Q, see Eq. (4.1). Clearly, Eq. (4.4) reveals concentration variations on length scales on the order of the full channel length $0 \le x \le L$, most prominently for smaller $|\mathrm{Pe}|$. Since the Péclet number quantifies the importance of flow, we can now reconcile the discrepancy between works which find electro-osmotic flow to be negligible [174] and others which find it to be important [178], as the former concerns a parameter set with small $\mathrm{Pe} \simeq 10^{-2}(R_b/R_t)^2$ and the latter with large $\mathrm{Pe} \simeq 3(R_b/R_t)^2$.

4.5 Optimal pressure

For $\Delta\psi = \pm 0.4$V, which for our standard parameter set gives $\Delta\rho = \mp 31$mM from Eq. (4.5), we plot the concentration profile $\bar{\rho}_s(x)$ of Eq. (4.4) in Fig. 4.2(a) for Péclet numbers between 0 and ∓ 200. In Fig. 4.2(b) we plot the salt concentration $\langle\bar{\rho}_s\rangle$ laterally averaged over the interval $x \in [0, L]$, which will play a key role in the electric conductivity $\mathbb{L}_{22}$, as a function of the imposed pressure drop ΔP for the three voltage drops $\Delta\psi = +0.4$V (red), 0V (green), and -0.4V (blue), as obtained numerically from solutions of the PNPS equations (symbols) and on the basis of a straightforward numerical integration of Eq. (4.4) (lines). The agreement, although not perfect, is very good especially for $\Delta P > 0$. Our Eq. (4.4) not only correctly predicts the increase/decrease compared to $2\rho_b$ for a negative/positive

potential drop but also the non-monotonic dependence on ΔP; the absolute difference with $2\rho_b$ is largest (and on the order of 30%) for $\Delta P \simeq \mp 10$mbar, which corresponds in both cases to $\mathrm{Pe} \simeq 0$. The two vertical dashed lines represent the pressure drop $\Delta P^* = -(\mathbb{L}_{12}/\mathbb{L}_{11})\Delta\psi$, where $Q = 0$ and hence $\mathrm{Pe} = 0$ on the basis of Eq. (4.1), such that the optimal concentration polarisation is to be expected. Collecting our earlier results we find the optimal pressure drop per voltage drop

$$\frac{\Delta P^*}{\Delta\psi} = \varepsilon\psi_0 \frac{8(R_b^2 + R_b R_t + R_t^2)}{3R_b^2 R_t^2} \overset{R_b \gg R_t}{\simeq} \frac{8\varepsilon\psi_0}{3R_t^2}, \tag{4.6}$$

which yields about -32mbar/V for our standard parameter set, and about -27 mbar/V for the extremely large tip-base ratios $R_b \gg R_t$ generated by the extrusion of a pipette in the experiments of Ref. [173] (if we assume $\psi_0 = -40$mV). Clearly, the inverse square scaling of ΔP^* with R_t is key to explaining the dramatic pressure sensitivity observed in the experiments [173]. In fact, our results suggest even more pressure sensitivity for larger conical channels, e.g. for $R_t = 10\mu$m we have ΔP^* in the microbar regime, which can already be exerted by the sound of passing traffic [190, 191]. For cases where $\Delta P \gg \Delta P^*$, concentration polarisation is washed out by the flow; variation of current with both pressure and voltage then closely follows Ohmic conduction.

Now that we have established that Eq. (4.4) gives a fair account of the salt concentration profile in the channel, we will use it to approximate $\mathbb{L}_{22}$. In the thin-EDL limit the total current I is dominated by the conductive component $-(De/k_BT)\rho_s(x,r)\partial_x\psi(x,r)$ of $\hat{\mathbf{x}}\cdot e\mathbf{j}_e(x,r)$ and cross-sectional integration of this current with Eq. (4.2) and the same thin-EDL limit as before yields $I_{\mathrm{cond}}(x) = (\pi R_b R_t/L)(e\Delta\psi/k_BT)eD\bar{\rho}_s(x)$, which manifestly depends on x on the basis of Eq. (4.4). In steady-state this lateral variation of the conductive current must be compensated by diffusive and advective currents and the resulting laterally-invariant current I can be obtained by treating the concentration profile $\bar{\rho}_s(x)$ as a collection of resistors in series [189], such that $\mathbb{L}_{22} = (De^2/k_BT)\langle\bar{\rho}_s\rangle$ which reveals that conductance is proportional to the laterally averaged salt concentration. For our standard parameter set we plot $\langle\bar{\rho}_s\rangle$ in Fig. 4.3(a) as a heat map in the $(\Delta\psi, \Delta P)$ plane, including a few iso-concentration contours. We clearly see the largest concentration variations, and hence the largest variations of $\mathbb{L}_{22}$, along the black line that represents $\Delta P = \Delta P^*$ of Eq. (4.6). In Fig. 4.3(b) we plot the ΔP-dependence of the electric current I (lines) as predicted from Eq. (4.1) for three voltage drops (± 0.4 V and zero), together with full numerical calculations (symbols) at the state points indicated by the color-matching symbols in (a) and Fig. 4.2(b). The overall agreement is quantitative at $\Delta\psi = 0$, which is fully in the linear-response regime, while the nonlinear gross features at $\Delta\psi = \pm 0.4$V, especially at $\Delta P \simeq \Delta P^* \simeq \mp 13$mbar, are accounted for with reasonable accuracy, the more so at the positive potential drop. In Fig. 4.3(c) we plot current-voltage

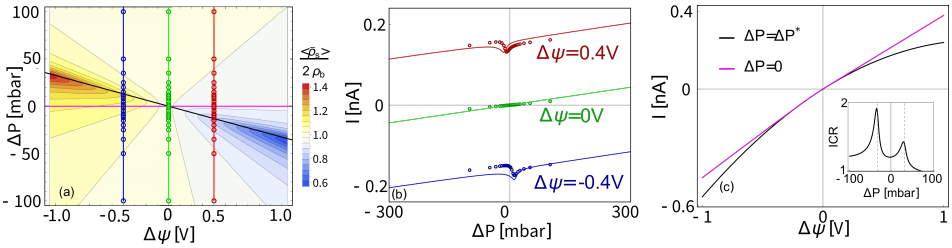

Figure 4.3: (a) Heat map of the laterally averaged salt concentration $\langle\bar{\rho}_s\rangle$ for the standard parameter set (see text) in the potential drop $\Delta\psi$ - pressure drop ΔP plane. (b) Current-pressure ($I-\Delta P$) relation for three fixed potential drops showing a minimum close to $\Delta P = \Delta P^*$ of Eq. (4.6). Symbols represent numerical solutions to the full PNPS equations at parameter combinations shown in (a), solid lines represent our analytic solution based on Eq. (4.1). (c) Current-voltage ($I-\Delta\psi$) relation for $\Delta P = 0$ (pink) and the optimal pressure drop $\Delta P = \Delta P^*$ (black, Eq. (4.6) which shows increased current rectification ICR compared to $\Delta P = 0$. The inset shows the pressure drop dependence of the ICR=$-I(-1\text{V})/I(1\text{V})$, which exhibits two maxima at $\Delta P = \pm\Delta P^*$.

relations at pressure drops $\Delta P = 0$ and $\Delta P = \Delta P^*$, using the same color coding as in (a). The degree of non-Ohmic behavior, characterised by the ionic current rectification ICR $= -I(-1V)/I(1V)$ is clearly larger at the optimal pressure drop ΔP^*, which is indeed borne out by the inset which shows the full ΔP dependence of ICR, revealing peaks at $\pm\Delta P^*$ shown as vertical lines.

4.6 Optimal geometry

Finally, using our explicit knowledge of $\langle\bar{\rho}_s\rangle$ and the full transport matrix of Eq. (4.1) we can explicitly search for an optimal cone geometry at which the deviation from Ohmic conductance is largest. Naively Eq. (4.5) suggests that for a large concentration profile the ideal tip-to-base ratio should be small ($R_t/R_b \ll 1$), however Eq. (4.4) shows that in this limit the concentration profile becomes localized near the tip resulting in a small channel-averaged concentration change. The ideal pore geometry balances the magnitude and spread of the concentration profile. An analytic expression for the difference between the laterally-averaged concentration $\langle\bar{\rho}_s\rangle$ and bulk concentration $2\rho_b$ is available in the limit $\mathrm{Pe} = 0$, where the concentration difference is largest, in which case $\langle\Delta\bar{\rho}_s\rangle = \langle\bar{\rho}_s\rangle - 2\rho_b$ is equal to

$$\langle\Delta\bar{\rho}_s\rangle = \frac{e\Delta\psi}{k_B T}\frac{\sigma}{R_t}\frac{\frac{R_t}{R_b}\left(2(\frac{R_t}{R_b}-1)-(1+\frac{R_t}{R_b})\log(\frac{R_t}{R_b})\right)}{(1-\frac{R_t}{R_b})^2}. \tag{4.7}$$

The prefactor $(e\Delta\psi/k_B T)(\sigma/R_t)$ is the tip Dukhin number times the dimension-

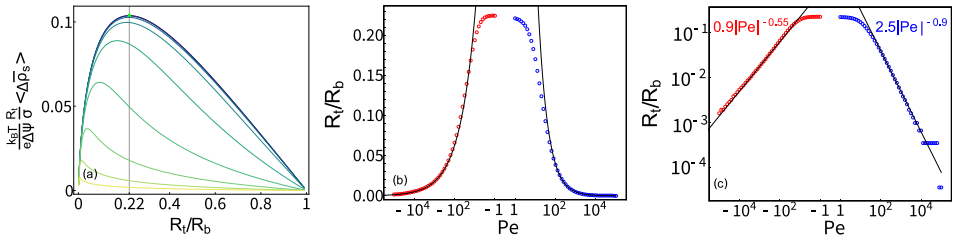

Figure 4.4: (a) Laterally averaged concentration $\langle\bar{\rho}_s\rangle$ normalized by $(\sigma/R_t)(e\Delta\psi/k_BT)$ for varying tip-base ratio R_t/R_b with the Péclet number between curves varying by $10^{1/2}$ with the yellow curve corresponding to Pe$= 10^3$ and blue curve with Pe$=10^{-1}$ closely matching Eq. (4.7). (b) Optimal tip-to-base ratio for varying Péclet in log-linear representation. Blue points denote optimal tip-to-base ratios for Pe$\in[10^{-1},10^5]$ and red points denote optima for Pe$\in[-10^{-1},-10^5]$, with optimal ratios $R_t/R_b \ll 1$ corresponding to Pe$\gg 1$. Black lines represent power-laws whose scaling is found was found in (c) by fitting the data in log-log representation. For large positive Pe the optimal tip-to-base ratio scales as $R_t/R_b \simeq 2.5|\text{Pe}|^{-0.9}$ while for large negative Pe it is well approximated by $R_t/R_b \simeq 0.9|\text{Pe}|^{-0.55}$.

less potential drop and bulk concentration, which diverges for vanishing tip radius, indicating that for the maximum non-Ohmic conductivity the tip size should be as small as possible. However as we assumed a thin-EDL limit from the very beginning this prediction only remains valid as long as $R_t \gg \lambda_D$. We estimate that optimization of non-linear current by minimization of the tip radius holds up to $R_t \approx 10\lambda_D$. It is easily checked that for fixed tip radius $\langle\Delta\bar{\rho}_s\rangle$ of Eq. (4.7) has a maximum at $R_t/R_b \simeq 0.22$, a geometry which hence optimizes diodic behavior.

At finite Pe no analytic expression for $\langle\Delta\bar{\rho}_s\rangle$ can be found, but its value can be straightforwardly calculated by numerical integration. In Fig. 4.4(a) we plot $[(k_BTR_t)/(e\Delta\psi\sigma)]\langle\Delta\bar{\rho}_s\rangle$ against R_t/R_b for Pe $\in[0,10^3]$. At Pe = 0 (blue line) the maximum laterally averaged concentration is found at a tip-to-base ratio $R_t/R_b \simeq 0.22$ (vertical line). As observed in Eq. (4.7) for non-zero Péclet number the ideal tip-to-base ratio (symbols) is always smaller than 0.22. Note that when no pressure drop ΔP^* is applied the Péclet number will scale with $\Delta\psi$ and the ideal pore geometry thus depends on the voltage operating range of a device. In Fig. 4.4(b) we plot the optimal tip-to-base ratio R_t/R_b against Péclet number on a linear-logarithmic scale. It can be seen that for small $|\text{Pe}| \leq 10$ the ideal ratio 0.22 holds, but for large Pe it decays algebraically to zero. In Fig. 4.4(c) we plot the same data as in (b) but now in a log-log representation to highlight the scaling in the Pe ≥ 100 regime. We find that the relation between optimal geometry and Pe is well described by a power law $b|\text{Pe}|^{-\nu}$ in this regime, with $b \simeq 2.5$, $\nu \simeq 0.9$ for positive and $b \simeq 0.9$, $\nu \simeq 0.55$ for negative Péclet; for all flow rates the ideal tip-to-base ratio is less than 0.22. Interestingly, the ideal pore geometry is independent of the channel length L, which follows from our Eq. (4.4) for $\bar{\rho}_s(x)$ that only depends on x/L, such that $\mathbb{L}_{22}$ (and in fact the whole matrix $\mathbb{L}$) is independent of

the channel length. Hence the concentration polarisation does not depend on the cone opening angle, which is surprising as most authors identify it as the key geometric parameter controlling pressure-sensitivity [173] and current rectification [176, 192].

Finally we note that while $\Delta\rho$ as defined by Eq. (4.5) is a measure for the concentration profile the ratio $\Delta\rho/\langle\Delta\bar{\rho}_s\rangle$ is large, which at zero flow is given by

$$\frac{\Delta\rho}{\langle\Delta\bar{\rho}_s\rangle} = \frac{2(R_t/R_b)^{-2}(1-\frac{R_t}{R_b})^3}{2\frac{R_t}{R_b}-2-(1+\frac{R_t}{R_b})\log(\frac{R_t}{R_b})}, \tag{4.8}$$

which for straight pores with $R_t \simeq R_b$ equals 12 and in the limit $R_t/R_b \ll 1$ is well approximated by $\Delta\rho/\langle\Delta\bar{\rho}_s\rangle \simeq 2R_b^2/R_t^2\log(R_b/R_t)$ which diverges for large base radii. Hence for conical pores in general $\Delta\rho \gg 12\langle\bar{\rho}_s\rangle$ and for our standard parameter set in the main text $\Delta\rho/\langle\Delta\bar{\rho}_s\rangle \simeq 100.9$ while for the optimal tip-to-base ratio $\Delta\rho/\langle\Delta\bar{\rho}_s\rangle \simeq 68.3$. In principle one could absorb the proportionality constant Eq. (4.8) in the definition of $\Delta\rho$, Eq. (4.5), to obtain a measure that accurately represents the laterally-averaged concentration profile $\langle\Delta\bar{\rho}_s\rangle$.

4.7 Conclusion

In conclusion, we provide a full microscopic understanding of the ultra-sensitive pressure- and voltage dependence of the electric conductivity of cone-shaped channels. We identify, and quantify, concentration polarisation due to geometric frustration which leads to a source term in Eq. (4.3), even in the thin-EDL case considered here. Moreover, we found an optimal channel geometry $R_t/R_b \simeq 0.22$ and an optimal operating pressure Eq. (4.6) for current rectification. These insights are important for further developments of mechanotronic [170, 171, 193] and biochemical [163–165] sensing as well as microfluidic [33, 147] and neuromorphic applications [167, 194].

4.8 Appendix

4.8.1 Derivation of transport coefficients

Here we will discuss the details and assumptions involved in the derivation of Eqs. (4.1)-(4.3) of the Chapter and the permeability $\mathbb{L}_{11}$, electro-osmotic mobility $\mathbb{L}_{12}$ and conductance $\mathbb{L}_{22}$ of the Onsager-like matrix starting from the Poisson-Nernst-Planck-Stokes PNPS equations (1.15)-(1.18) as derived in the Chapter 1. The analysis of the PNPS equations is greatly facilitated by the linear combinations given by the total local salt concentration $\rho_s = \rho_+ + \rho_-$, charge density $e\rho_e = e(\rho_+ - \rho_-)$, the ionic charge flux density $e\mathbf{j}_e = e(\mathbf{j}_+ - \mathbf{j}_-)$, and the salt flux density $\mathbf{j}_s = \mathbf{j}_+ + \mathbf{j}_-$ resulting in

$$\mathbf{j}_e = -D\big(\nabla\rho_e + \rho_s \frac{e\nabla\psi}{k_B T}\big) + \mathbf{u}\rho_e, \tag{A4.1}$$

$$\mathbf{j}_s = -D\big(\nabla\rho_s + \rho_e \frac{e\nabla\psi}{k_B T}\big) + \mathbf{u}\rho_s. \tag{A4.2}$$

Here we note that the conduction terms $\propto \nabla\psi$ are proportional to ρ_s for the electric flux and to ρ_e for the salt flux. This coupling will prove to be key to understanding the physics of the cone-shaped channel.

Salt current The hierarchy of length scales $L \gg R_b \geq R_t > \lambda_D$ serves as the starting point of our derivation. When the channel is much longer than the largest radius $L \gg R_b$ entrance-outlet edge effects to the conductance can be neglected, but we will consider such effects in Chapter 5. Additionally, in the long-channel limit all radial components of fluxes and gradients are expected to be much smaller than the corresponding lateral components. Combined with the thin-EDL limit $\lambda_D \ll R_t$, which is motivated by the experimental conditions in Ref. [173], this ensures that the local ion concentrations and the electric field are essentially equal to the cross-sectional averaged salt concentration and electric field, so $\rho_s(x,r) \simeq \bar{\rho}_s(x) = 2\pi \int_0^{R(x)} \rho_s(x,r) r\mathrm{d}r/\pi R^2(x)$ and $\partial_x\psi(x,r) \simeq \partial_x\bar{\psi}(x) = 2\pi \int_0^{R(x)} \partial_x\psi(x,r) r\mathrm{d}r/\pi R^2(x)$. Moreover, the thin-EDL limit does not only allow us to neglect the influence of channel curvature on the EDL, but also allows us to neglect the influence of salt adsorption [189] on the cross-sectional averaged salt concentration $\bar{\rho}_s(x)$. Hence by using the thin-EDL assumption we neglect the inhomogeneous advection of salt through the EDL. For Debye lengths orders of magnitude smaller than the pore radius we expect this assumption to be quite robust, however it will break down at extremely high surface potentials $e\psi_0/k_B T \gg 1$ as in this regime salt adsorption grows exponentially with ψ_0. In summary using the approximations $\rho_s(x,r) \simeq \bar{\rho}_s(x)$, $\partial_x\psi(x,r) \simeq \partial_x\bar{\psi}(x)$, $\lambda_D \ll R_t$ in conjunction with the observation from numerical calculations that $|\rho_e(r \ll R(x))| \ll |\sigma/R(x)|$ will readily result in Eq. (4.3) upon radially integrating Eq. (A4.2).

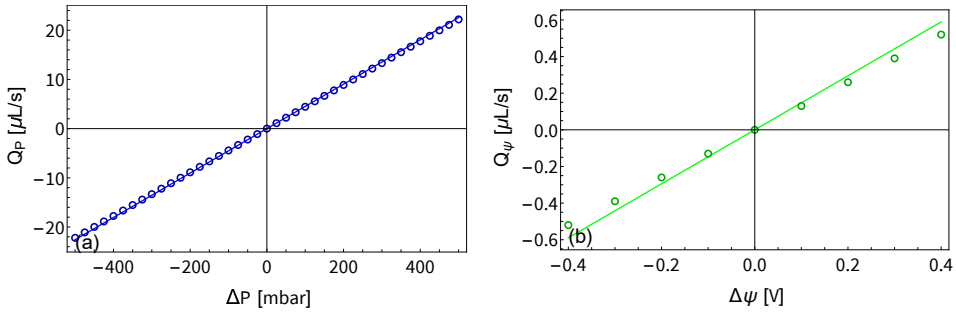

Figure A4.1: (a) Poiseuille-like fluid flux Q_P as a function of the pressure drop ΔP at vanishing potential drop $\Delta\psi = 0$ and (b) electro-osmotic potential driven fluid flux Q_ψ as a function of the potential drop $\Delta\psi$ at a vanishing pressure drop $\Delta P = 0$, both for our standard parameter set (see text) and obtained from numerical solution of the full PNPS equations (1.15)-(1.18) (symbols) and from $\mathbb{L}_{11}$ and $\mathbb{L}_{12}$ (lines), respectively. Both fluid fluxes are linear in their respective driving force. There is good agreement between analytic and numerical results for the pressure driven flow Q_P, however the analytic expression for the electro-osmotic flow Q_ψ overestimates the flow rate by $\sim 10\%$.

Fluid flow Before calculating the fluid flux Q, we have to verify that the linear response relation Eq. (4.1) in the Chapter is valid for flow, as in the literature there is experimental and numerical evidence that electro-osmotic flow can invert in conical pores under certain experimental conditions [153–155]. This would have a dramatic impact on the pressure sensitivity of the cone. However, as can be seen in Fig. A4.1 we find that in the experimental regime of Ref. [173] no flow inversions occur as Q is linear in both the pressure and potential drop. It should be noted that any non-linearity in the fluid flow $Q(\Delta P, \Delta\psi)$ will significantly change the current-pressure relation $I(\Delta P, \Delta\psi)$. Having verified that the flow Q is linear in their respective driving forces, it now remains to find expressions for first $\mathbb{L}_{11}$ and then $\mathbb{L}_{12}$. When the channel has a tip radius of zero and vanishing surface charge an expression for the fluid flux $Q_P = (\pi R_t R_b/L)\mathbb{L}_{11}\Delta P$ is known [186–188]. Modifying this solution by replacing the pore length L' of a channel with a tip radius of zero with our actual channel length $L = L'(R_b - R_t)/R_b$ (with $L' \geq L$) representative of a channel with the same opening angle $2\alpha = 2\tan^{-1}(R_b/L') = 2\tan^{-1}((R_b - R_t)/L)$ but now a non-zero tip radius, we find

$$Q_P(\Delta P) = \frac{\Delta P}{\eta} \frac{3\pi L^3 R_b^3 R_t^3 \alpha^4}{8(R_b - R_t)^4 (R_b^2 + R_b R_t + R_t^2)}, \tag{A4.3}$$

which for $R_b - R_t \ll L$ reduces to $\mathbb{L}_{11}$ in the Chapter. The agreement between this expression for the pressure-driven fluid flux Q_P (solid line) and the numerically obtained flow (symbols) is remarkable and can be seen in Fig. A4.1(a).

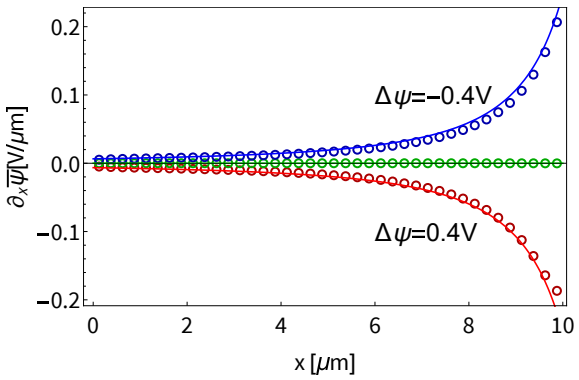

Figure A4.2: The electric field $-\partial_x\bar{\psi}(x)$ for our standard parameter set with pressure drop $\Delta P = 0$ as a function of the lateral position x for $\Delta\psi = \pm 0.4$V and 0 volt (green) obtained from full numeric solutions of the PNPS equations(1.15)-(1.18) (symbols) and Eq. (4.2) (line) for our standard parameter set (see text). Good agreement between numeric and analytic results is found, which confirms the accuracy of Eq. (4.2).

Electro-osmotic flow We now continue with the calculation of the electro-osmotic flow Q_ψ which first requires an expression for the electric field $-\partial_x\bar{\psi}(x)$ given in the Chapter by Eq. (4.2). This equation is valid under two conditions, (i) no electric field lines permeate the channel wall, and (ii) the space charge outside of the EDL is negligible. The first condition ensures that all electric field lines remain in the channel and holds when the dielectric constant of the channel wall is much smaller than that of the solvent. The second condition ensures that the divergence of the electric field is zero $\nabla\cdot\nabla\psi(x,r) = 0$, for all r several Debye length away from the channel wall, ensuring that no new field lines appear. For straight channels this is a natural assumption, however in conical channels the lateral variation of the electric current $I(x)$ could in principle allow for the build-up of space charge. In our discussion of the numerical results we verify that the effect of this space charge is small and can largely be ignored in the parameter regime of our prime interest. When both condition (i) and (ii) are met the number of electric field lines remains constant over the channel length and the total lateral electric field through a radial slice multiplied by the area of the slice likewise has to be constant, $\pi R^2(x)\partial_x\bar{\psi}(x) =$ constant. Now the electric field as function of lateral position can be found by observing that over the length of the pore the total potential drop has to equal to $\Delta\psi = -\int_0^L \partial_x\bar{\psi}\mathrm{d}x$, resulting in Eq. (4.2) of the text. In Fig. A4.2 we compare $\partial_x\bar{\psi}$ of Eq. (4.2) (solid lines), with the numerically obtained function $\partial_x\psi(x, r = 0)$ along the symmetry axis in calculations for $\Delta P = 0$ (symbols) and find excellent agreement. In order to calculate $\mathbb{L}_{12}$ from the electric field we use the solution for the potential-driven flow through a cylindrical pore but now with position dependent radius and electric field $-\partial_x\bar{\psi}(x)\pi R^2(x)(\varepsilon\psi_0/\eta)$ [189] and observe that it is constant over the length of the pore as $\partial_x\bar{\psi} \propto 1/(\pi R^2(x))$.

Hence this Ansatz yields a bonafide divergence-free electro-osmotic flow given by

$$Q_\psi(\Delta\psi) = -\frac{\Delta\psi}{L}\pi R_\mathrm{t} R_\mathrm{b}\frac{\varepsilon\psi_0}{\eta}, \tag{A4.4}$$

where we neglected terms of order λ_D/R on the basis of the thin-EDL limit. In Fig. A4.1(b) it can be seen that there is a minor deviation of $\sim 10\%$ between Q_ψ obtained from numerical calculations and this analytic approximation. Implicitly the PNPS equations (1.15)-(1.18) allow for diffusio-osmotic fluid flow, driven by the concentration gradient $\partial_x\bar{\rho}_\mathrm{s}$. As the concentration profile and hence the gradient is a non-linear function of the potential drop, any diffusio-osmotic flow would manifest as a non-linear contribution to $Q_\psi(\Delta\psi)$. As no significant deviation from linearity is observed in our numerical results for $Q_\psi(\Delta\psi)$ we neglect diffusio-osmotic flow.

Comparison analytic and numerical salt concentrations Having found expressions for both $\partial_x\bar{\psi}$ and Q we can now straightforwardly solve Eq. (4.3), directly yielding Eq. (4.5) of the Chapter. We compare Eq. (4.4), solid lines) with the concentration from numerical calculations in Fig. A4.3 (symbols) for several ΔP and $\Delta\psi$. We see that while the agreement is not perfect both the non-monotonic ΔP trend and the overall shape of the concentration profile are captured rather reasonably. It can also be seen that the boundary condition used for analytic calculations ($\rho_\mathrm{s}(0) = \rho_\mathrm{s}(L) = 2\rho_\mathrm{b}$) are not fully representative of the numerical calculations, as the concentration profile extends a small distance out of the channel. This discrepancy is possible as in the numerical calculations we apply the boundary condition of bulk concentrations far away rather than at the channel edges. The description of the concentration profiles extending out of the in- and outlets of the conical pore would require a full description of the flow, electric field and currents at the edges of the cone which is not tractable analytically.

More significant than the deviating concentration at the tip and base is the sign change of the bulk-excess concentration profile when going from positive ΔP to $\Delta P \ll -50$mbar, a feature our analytic theory cannot explain. The deviation occurs at very negative Péclet number and represents a secondary non-linearity unrelated to the non-linearity reported in the Chapter. We speculate the non-linearity may be due to the inhomogeneous advection current $\partial_x I_\mathrm{adv} \propto \partial_x(2Q\sigma/R) \neq 0$ that can build up significant space-charge $\rho_\mathrm{e}(x,r)$ outside the EDL. To study this secondary non-linearity in full detail would require solving for $\partial_x I = 0$ and $\partial_x J = 0$ simultaneously. While striking, the difference in sign of the difference from the bulk concentration between our analytic and numeric concentration around Pe$\ll -1$ has little influence on the current I, as the concentration deviation is an order of magnitude smaller than the concentration change around Pe = 0. In summary we identify three major sources of error (i) our analytic expression underestimates

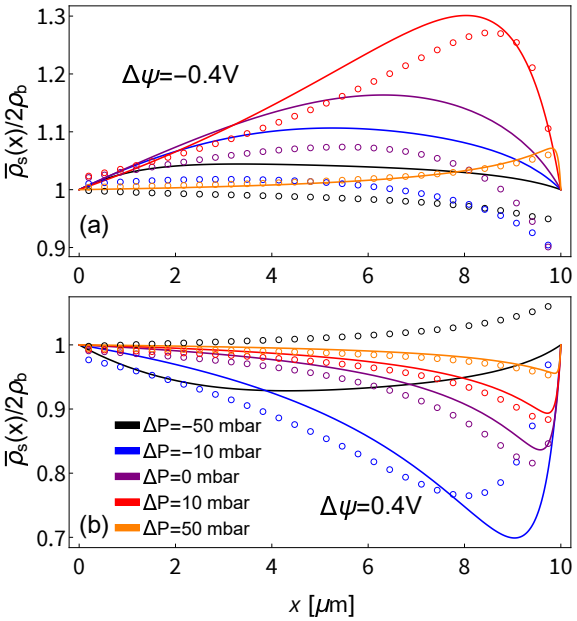

Figure A4.3: Cross-sectional averaged concentration profile $\bar{\rho}_s(x)$ over the full channel length from numerical calculations of the full PNPS equations (symbols) compared to curves plotted with Eq. (4.5) for our standard parameter set (see Chapter), potential drop $\Delta\psi = -0.4$V (a) and $\Delta\psi = 0.4$V (b) and varying pressure drop ΔP. Numeric and analytic results agree for positive ΔP but deviate for increasing negative ΔP. Concentration profiles are largest for $\Delta P = \mp 10$ mbar which is rather close to $\Delta P^* = \mp 13$ mbar, where fluid flow vanishes.

electro-osmotic flow Q_ψ by about 10%, (ii) imposing bulk concentrations on the channel edges $\bar{\rho}_s(0) = \bar{\rho}_s(L) = 2\rho_b$ implicitly neglects edge effects, and (iii) neglecting minor secondary non-linearities, which are probably related to the lateral variation of the current $I(x)$ that are to be compensated by a (small) space charge distribution $\bar{\rho}_e(x)$. A final limitation of our theory is that for large negative $\Delta\rho$ the theory allows for $\bar{\rho}_s(x)$ to become locally negative, which is clearly unphysical. This unphysical result can emerge because the Debye length increases when the concentration decreases, eventually invalidating our starting assumption $\lambda_D \ll R$. Care should thus be taken not to use the theory in this regime, with a negative conductance a hallmark that the range of validity has been exceeded. Throughout we restrict attention to concentration profiles that deviate less than about 30% from the bulk concentration, which also allows for equating the relative change of the channel conductance to (the negative of) the change of the relative channel resistance.

Electrical conductance To calculate the last matrix element $\mathbb{L}_{22}$ we radially integrate Eq. (5.2), resulting in a diffusive, conductive and advective current. In

our discussion of numerical results we show that the diffusive current is negligible, which is consistent with the assumption of a negligible space charge outside the EDL, $\rho_e(r \ll R - \lambda_D, x) \approx 0$. This leaves two components of the current to be calculated $I = I_{cond} + I_{adv}$ whose ratio scale as $I_{adv}/I_{cond} \propto \lambda_D/R$ allowing us to neglect the advective component to $\mathbb{L}_{22}$ when $\lambda_D/R \ll 1$. Now the total current due to a potential drop $\Delta\psi$ is straightforwardly found by integration of the conductive component $-(De/k_BT)\rho_s(x,r)\partial_x\psi(x,r)$ in Eq. (A4.1) and by using $\rho_s(r,x) \simeq \bar{\rho}_s(x)$ and $\psi(r,x) \simeq \bar{\psi}(x)$ we find

$$I_{cond}(x) = eD\frac{e\Delta\psi}{k_BT}\frac{\pi R_t R_b}{L}\bar{\rho}_s(x), \tag{A4.5}$$

which is inhomogeneous for any non-constant $\bar{\rho}_s(x)$. This inhomogeneity will lead to formation of a space charge ρ_e outside the EDL. However, in our discussion of numerical results we will show that this space charge is small. By treating the concentration profile as a collection of resistors in series[189] we can obtain the ultimate, laterally constant current. From this it follows that $\bar{\rho}_s(x)$ in Eq. (A4.5) should be replaced by the inverse average $L/\int_0^L(\bar{\rho}_s(x)^{-1})\mathrm{d}x$ which is close to the lateral average $\langle\bar{\rho}_s\rangle$ as long as $|\log(\bar{\rho}_s(x)/(2\rho_b)| < 1$. The error of this approximation diverges when $\bar{\rho}_s(x)/2\rho_b$ approaches zero. As we restrict our attention to concentration profiles that deviate less than about 30% from the bulk concentration, this approximation is very reasonable.

Having already calculated $\mathbb{L}_{12}$ for the electro-osmotic flow Q_ψ we can invoke Onsager's reciprocal relation, which states that $\mathbb{L}_{21} = \mathbb{L}_{12}$[3, 8, 9], to find the fully advective pressure-driven current and obtaining the full current

$$I(\Delta\psi, \Delta P) = \frac{\pi R_t R_b}{L}\left(\frac{e^2 D\Delta\psi}{k_BT}\langle\bar{\rho}_s\rangle - \Delta P\frac{\varepsilon\psi_0}{\eta}\right). \tag{A4.6}$$

Full Onsager-like matrix Finally, combining $\mathbb{L}_{11}$, $\mathbb{L}_{12}$ and $\mathbb{L}_{22}$ our ultimate expression for the Onsager-like matrix Eq. (4.1) reads

$$\frac{\pi R_b R_t}{L}\begin{pmatrix} \frac{R_b^2 R_t^2}{8\eta\langle R^2\rangle} & \frac{-\varepsilon\psi_0}{\eta} \\ -\frac{\varepsilon\psi_0}{\eta} & \frac{e^2 D}{k_BT}\langle\bar{\rho}_s\rangle \end{pmatrix}\begin{pmatrix}\Delta P \\ \Delta\psi\end{pmatrix} = \begin{pmatrix} Q \\ I\end{pmatrix}. \tag{A4.7}$$

4.8.2 Discussion of the numerical results

Here we will discuss the numerical results of the full PNPS equations (1.15)-(1.18) in depth and show that the effect of the space charge outside the EDL on the current I can be neglected. In Fig. A4.4 we plot our numerical solutions of the pressure excess electric current $I_P = I(\Delta P, \Delta\psi) - I(0, \Delta\psi)$ as a function of the

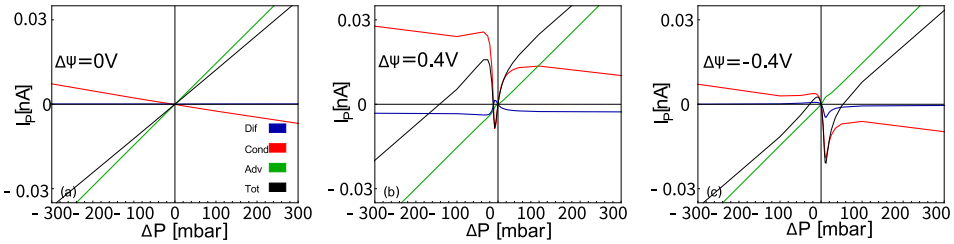

Figure A4.4: Total pressure excess diffusive, conductive, advection and net electric current (respectively Dif, Cond, Adv and $I_{\rm P}$) at $x = 0.9L$ from numerical solutions of the full PNPS equations (1.15)-(1.18) as function of the pressure drop ΔP offset by the current at $\Delta P = 0$ for our standard set of parameters in the Chapter. For (a) where $\Delta\psi = 0$ the current is linear in ΔP and dominated by the advective current. For (b) and (c), where respectively $\Delta\psi = +0.4$V and $\Delta\psi = -0.4$V, the current is non-linear for low pressure drops ($|\Delta P|$ <50 mbar) and here conductive current dominates the non-linear pressure-current relation, with diffusive and advective components only marginally contributing. At large pressures the net current is again dominated by the advective, streaming current, current which follows the same linear trend found for $\Delta\psi = 0$.

pressure drop ΔP for our standard parameter set and (a) $\Delta\psi = 0$, (b) $\Delta\psi = +0.4$V, and (c) $\Delta\psi = -0.4$V. When no potential drop is applied we find that the electric current is linear in the pressure drop and dominated by advection, as can be seen in Fig. A4.4(a) where we plot $I_{\rm P}(\Delta P, \Delta\psi)$, split into its diffusive, conductive and advective components. When the pressure drop is applied in conjunction with a potential drop we find that the pressure-excess current is strongly non-linear, as can be seen Fig. A4.4(b) and (c). A minimum in the total current is found at $\Delta P = \mp 10$ mbar for $\Delta\psi = \pm 0.4$V in Fig. A4.4(b) and (c), and near the minimum the conductive current dominates over the advective and diffusive currents. For pressure drops larger than $|\Delta P|$ >100 mbar the advective current $I_{\rm P}$ dominates and follows the linear relation observed for $\Delta\psi = 0$ shown in Fig. A4.4(a). The non-linearities in (b) and (c) are mainly due to the conductive component $-(De/k_BT)\rho_{\rm s}(x,r)\partial_x\psi(x,r)$ of the electric current Eq. (5.2) which depends not only on the salt concentration $\rho_{\rm s}(x,r)$ but also the electric field $-\nabla\psi(x,r)$. Inspecting Fig. A4.5, where we plot the ΔP-dependence of the current, the salt concentration, and the electric field at $x = 0.9L$ all normalized by their values at vanishing pressure drop, we indeed find that both the salt concentration $\bar{\rho}_{\rm s}$ as well as the electric field $-\partial_x\bar{\psi}$ vary with ΔP. However, we find that the variation of the electric field is ~ 5 times smaller than the change of concentration with pressure, and actually opposes the non-linearity of the conduction current for $\Delta\psi = -0.4$V.

As the change in electric field actually counter-acts the non-linearity observed in the electric current we conclude that the ΔP dependency of $\partial_x\bar{\psi}$ cannot be the dominant driving force behind the non-linear current $I(\Delta P)$. This suggests that the

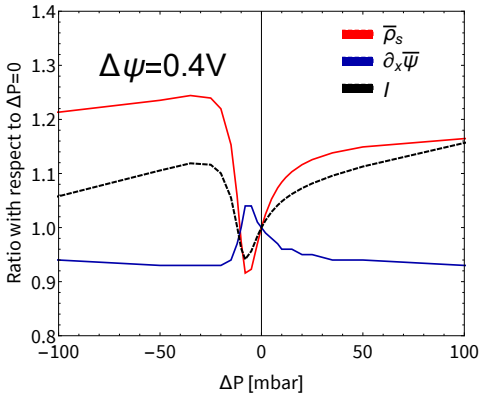

Figure A4.5: Pressure drop dependence of the cross-sectional averaged electric field $\partial_x\bar{\psi}$, salt concentration $\bar{\rho}_s$, and total current I, all normalized with their respective values at $\Delta P = 0$, at lateral position $x = 0.9L$ and for a potential $\Delta\psi = 0.4$V, as obtained from numerical solutions of the full PNPS equations (1.15)-(1.18) for our standard parameter set (see Chapter). The relative deviations from unity are much larger for the salt concentration and the current than for the electric field; in fact the current correlates well with the salt concentration and even anti-correlates with the electric field.

non-linear current I can be essentially understood by considering the dependency of the salt density ρ_s on $\Delta\psi$ and ΔP, with the space charge density ρ_e outside of the EDL only contributing minutely to the non-linearity both through diffusive I_{dif} and advective I_{adv} currents as well as pressure dependent electric field $-\partial_x\bar{\psi}$. Hence Fig. A4.5 shows that dependency of space charge ρ_e on ΔP only leads to negligible variation in the magnitude of diffusive and advective current I_{dif} and I_{adv} as seen in Fig. A4.4(b) and (c). The conclusion that space charge is negligible is based on an empirical observation of numerical results, so we cannot rule out that there are regimes in which space charge does dominate the non-linear current. However, as we have chosen a set of parameters to reproduce the experimental set-up of Ref. [173] we can conclude that for this specific set of experiments space charge is negligible and not of key importance to the non-linear current $I(\Delta P)$.

Chapter 5

Ion current rectification and long-range interference in conical silicon micropores

Abstract

Fluidic devices exhibiting ion current rectification (ICR), or ionic diodes, are of broad interest for applications including desalination, energy harvesting, and sensing, amongst others. For such applications a large conductance is desirable which can be achieved by simultaneously using thin membranes and wide pores. In this Chapter we explain the ionic current rectification observed in micron sized conical channels in a thin silicon membrane with pore diameters comparable to the membrane thickness but both much larger than the electrolyte screening length. We show that for these pores the entrance resistance is not only key to Ohmic conductance around 0 V, but also for understanding rectification. The only fit parameter in this theory is the membrane surface potential, for which we find that it is voltage dependent and its value is excessively large compared to literature. From this we infer that surface charge outside the pore strongly contributes to both the observed Ohmic conductance and rectification, albeit by a different extent. Our collaborators experimentally verified this hypothesis in a small array of pores and find that ICR vanishes due to pore-pore interactions mediated through the membrane surface, while Ohmic conductance around 0 V remains unaffected. We find that the pore-pore interaction for ICR is set by a long-ranged decay of the concentration which explains the surprising finding that the ICR vanishes for even a sparsely populated array with a pore-pore spacing as large as 7 μm.

This Chapter is based on the publication

M. Aarts, W.Q. Boon, B. Cuénod, M. Dijkstra, R. van Roij, & E. Alarcon-Llado (2022). *Ion current rectification and long-range interference in conical silicon micropores*, ACS Applied Materials & Interfaces.

There are paragraphs and figures that are taken or modified from the above-mentioned publication and its supporting information. The experimental work was performed by M.A., B.C. and E.A. at AMOLF in Amsterdam. The co-authors gave their permission for the reproduction. The author contributions to this publication are as follows:

M.A. and W.Q.B. contributed equally to this work.

5.1 Introduction

Ionic transport near solid-liquid interfaces can differ drastically from that in bulk due to Coulombic interactions with the surface [195]. Such interface effects can be used to tailor nanofluidic devices [91], finding applications in desalination [196, 197], ionic circuitry [198, 199], bio-chemical sensing [200–204], energy harvesting [205, 206] and neuromorphic signalling [207–209]. A particularly useful element for directional control of ionic currents is a current rectifier [144, 164, 165, 202], also known as a diode. In fact, the phenomenon of ion current rectification (ICR), allowing for unidirectional charge transport, has been observed and extensively studied in nanochannels [159, 160, 168, 210].

The ICR originates from an asymmetry in the ionic current along the length of the channel, due to a varying relative contribution to the ionic current of the charge-selective electric double layer (EDL) that screens the charge on the channel walls. Typically, ICR is demonstrated in nanoscale conical channels, where EDL overlap occurs on the narrow end of the channel [159, 160]. In general, the ICR mechanism for a geometrically asymmetric, or tapered, channel can be understood by considering that the relative contribution of the salt current through the EDL to the total current is smaller at the wide opening than at the narrow opening [211, 212]. This results in an asymmetry of the transference (i.e. the partial current due to either ionic species). Considering a channel with a negative surface charge on its wall, resulting in an EDL with excess positive ionic charge, an electric field directed towards the narrow end leads to more ions leaving the small opening than entering the large opening (before steady state is reached), resulting in depletion of ions inside the channel, and a suppressed conductance [184]. The opposite is true for an oppositely directed electric field, resulting in accumulation of charge carriers and enhanced conductance. More broadly, the required asymmetry in transference can be introduced not only by geometry, but also by a variation of e.g. charge or concentration [184, 211, 213].

For application purposes regarding larger scale porous membranes, a low electric resistance of the channel is desirable to mitigate Ohmic losses. Two intuitive ways to construct a channel with low resistance are by making (i) larger openings [184] or (ii) shorter channels [177, 214]. Considering the accumulation/depletion mechanism described above, recent theoretical work (Chapter 4) predicts that ICR can also occur in wide channels without overlapping electric double layers, as long as a substantial part of the ionic current is due to surface conductance [161, 162, 183, 184, 215, 216]. In fact, ICR in mesoscopic channels [173] and chemically modified micronsized systems have recently been observed [162, 217, 218]. For thin membranes with short channels on the other hand, it has become clear that the applied potential partially drops outside the channel, rather than fully over the channel itself [177, 219–222]. These extended entrance effects

give rise to an edge, or access, resistance and become relevant for the behavior of a fluidic pore with a channel length of the order of the diameter, which can either positively contribute to ICR or interfere destructively in arrays of pores [222–224]. As of now, however, such pore-pore interactions are still poorly understood.

Outline In this Chapter we consider conical, i.e. geometrically asymmetric, fluidic micropores in thin (2 μm) crystalline silicon membranes, with base and tip radii of $R_b \approx 1.5$ μm and $R_t \approx 0.5$ μm, respectively, such that even the smallest of these channel dimensions is larger than the typical electrolyte screening length by more than an order of magnitude. These pores exhibit ion current rectification, and we develop an analytical theory for the channel conductance in which the surface potential is the only fit parameter. We stress that the (Ohmic) channel conductance at low applied potentials and ICR are distinct phenomena and we find that we need a different surface potential to fit the experimental data to these two effects, with both surface potentials being very large, implying a very large surface charge. We interpret the value of these fitted surface potentials as non-physical, and rather attribute this excessively large charge to a contribution of conduction along the planar membrane surface outside the channel at the inlet and outlet of the pore unaccounted for in our model. By converting this required surface charge to an effective area, we estimate that this membrane surface conduction is relevant up to distances around the pore opening as large as 7.4 μm for Ohmic channel conductance, and 15.0 μm for ICR, implying that a larger area around the pore is required for ICR. This hypothesis is tested by our collaborators who fabricated a small array of pores with a 10 μm spacing ($\approx 10^6$ pores/cm^2). Indeed, they find that despite this low pore density the Ohmic conductance remains unaffected, but that the ICR vanishes for the array. Extended entrance effects at the micron scale therefore appear to play a significant role in the required asymmetry in ion transport through pores in thin membranes, which we attribute to the long-ranged decay of the electric field outside the pore. This electric field creates a concentration profile with a similar long-ranged, inverse-square with distance, decay into the bulk. This scale-free decay introduces long-ranged pore-pore interactions for thin pores, which become particularly relevant in array configurations typical for membranes.

5.2 Experimental observation

For the conductance measurements single micron-sized, straight or tapered, pores were fabricated by our experimental collaborators in 2 ± 0.5 μm thick crystalline silicon membranes using a focused ion beam (FIB). Conductance measurements were carried out by placing the membrane between two aqueous reservoirs containing KCl of equal bulk concentration (ρ_b), and applying a potential between the

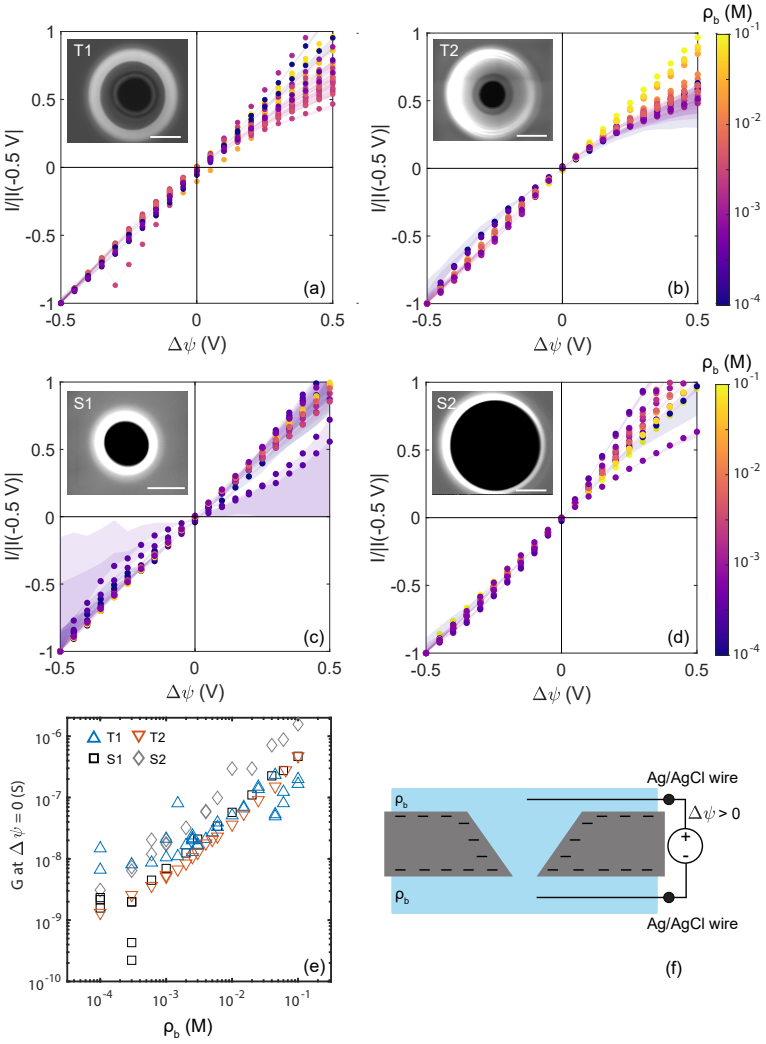

Figure 5.1: (a-d) Experimental current-voltage (I-V) curves, normalized at a potential drop of -0.5 V at various KCl concentrations $\rho_b \in [10^{-4} - 10^{-1}]$ M indicated by the colour scale. The shaded region indicate uncertainty in the measurement due to the leakage current obtained from an as-received membrane (SI-3 of Ref. [181]). Systematic current rectification is observed for tapered pores T1 and T2 with the conductivity at $+0.5$ V being lower than at -0.5 V. The inset shows scanning electron microscopy images of the tapered pores T1 (a) and T2 (b) and straight pores S1 (c) and S2 (d) after fabrication. The scalebars are 1 μm. (e) Conductance of the pores at 0 V as a function of KCl concentration ρ_b(M). (f) Schematic of the experimental setup where 2 aqueous reservoirs of equal KCl concentration are separated by the membrane with a single pore. The polarity of the potential is such that positive potentials indicate the anode being in the reservoir facing the large opening of the pore.

reservoirs using Ag/AgCl wire electrodes (Figure 5.1 (f)). Of note is the polarity of the applied potential, where positive potentials indicate the anode being in the reservoir facing the large opening of the pore.

The quasi-static current-voltage (I-V) curves were recorded between -0.5 V and 0.5 V, at different reservoir KCl bulk concentrations ρ_b ranging from 10^{-1} M to 10^{-4} M, for 4 membranes containing a single pore. The insets of Figure 5.1(a)-(d) show scanning electron microscopy (SEM) images directly after fabrication of the tapered pores T1 (base and tip radii $R_b \simeq 1.5\mu$m, $R_t \simeq 0.5\ \mu$m) and T2 ($R_b \simeq 1.5\mu$m, $R_t \simeq 0.4\ \mu$m) and two straight reference pores S1 ($R_b = R_t \simeq 0.6\ \mu$m) and S2 ($R_b = R_t \simeq 1.5\ \mu$m).

The corresponding I-V curves are shown as circles in Figure 5.1(a)-(d), where the colors label the salt concentration ρ_b. As the magnitude of the current response varies by several orders of magnitude over the salt concentration range, the current is normalized to the value at an applied potential of -0.5 V for visibility. The shaded regions indicate the possible contribution from leakage current through the membrane, averaged from measurements on an as-received membrane without a pore. Due to the range in magnitude of the measured currents, this is most relevant for the lowest concentrations and the smallest pore (S1). The conductance at 0 V as a function of concentration is shown in Figure 5.1(e). A linear decrease of the conductance with decreasing concentration is observed with the conductance saturating at $\rho_b < 1$ mM.

At the highest concentrations (yellow, ρ_b = 0.1 M), and therefore the smallest Debye length ($\lambda_D \simeq 1$ nm), all pores show a linear I-V response, consistent with bulk dominated transport. At lower concentrations, however, conductance through the tapered channels starts to show an assymetric conductance and hence ion current rectification. It should be noted that even at the lowest concentration, ρ_b = 0.1 mM, the electrolyte screening length $\lambda_D \simeq 30$ nm is much shorter than the smallest tip radius, so that the micropores are well outside the regime of EDL overlap. While some curves for the straight pores S1 and S2 show an erratic deviation from ideal symmetrical conductance, the tapered pores T1 and T2 show systematic modulation of rectification, where the conductance at positive potentials is smaller than that at negative potentials.

5.3 Theoretical framework

In the following, we present a model for the potential-dependent conductance of a tapered pore and obtain a closed-form expression that simultaneously describes Ohmic conductance and ion current rectification. Currently in the literature there are two, complementary, theories for current rectification without EDL overlap for pores with large aspect ratio. The theory by CENGIO [183] and POGGIOLI

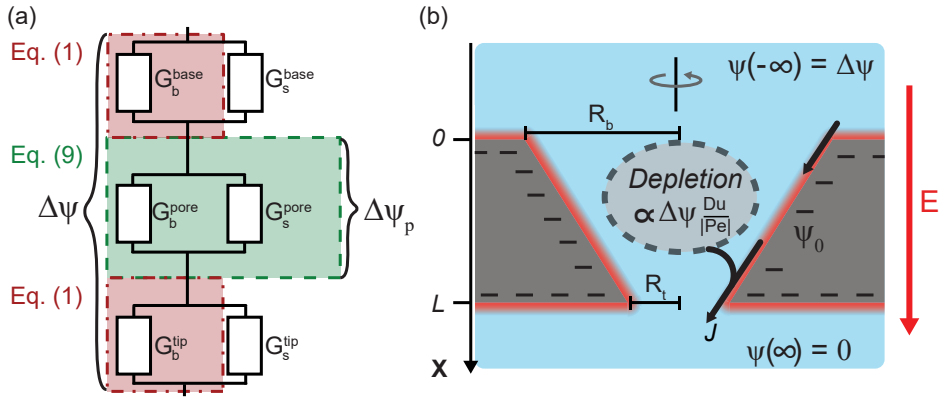

Figure 5.2: (a) Schematic equivalent circuit of a pore featuring bulk and surface conductance G_b^i and G_s^i respectively, at the base-, tip- and within the pore-region. The elements considered in our analytical model are highlighted, where part of the applied potential $\Delta\psi$ drops over the edge resistance (red dash-dotted region), as captured by Eq. (5.1). The conductance of the pore with the remaining potential $\Delta\psi_p$ (green dashed region) is described by Eq. (5.9). (b) Representation of the conical system under consideration with base and tip radii R_b and R_t, respectively, and an electric field $-\partial_x\psi = E$ pointed towards the tip. As outlined in the main text, the depletion of ions in the channel is proportional to the potential drop $\Delta\psi$ times the ratio of the Dukhin (Du) and Péclet (Pe) numbers as shown in Eq. (5.8a) and illustrated here for a channel wall with a negative surface charge resulting in depletion for a positive potential drop due to a salt flux J (black arrow) through the electric double layer (EDL) that increases towards the tip.

[184] describes ICR through the variation of the surface conductance over the pore length but neglects electro-osmotic flow, while the theory of Ref. [212] in Chapter 4 does account for this flow but fails at extremely low salt concentrations. Hence both theories are complementary rather than mutually exclusive: Refs. [183, 184] are valid at all concentrations while the theory of the previous Chapter is valid at all (low-Reynolds) flow rates. We will find that the experiments show characteristic flow-sensitive behavior, and therefore we build on the theory from Chapter 4. However, to describe the experiments either theory would need to be extended as the membranes thickness here is similar to the radius of the pores, and the theory therefore has to account for the electric edge resistance which is comparable to the pore resistance. There is a variety of theories available in the literature accounting for Ohmic edge resistance [91, 177, 219–221, 225], the most commonly used one by Hall [220] which we reproduce below as a special case. In this Chapter we will find that not only do edge resistances alter Ohmic conductance, they also significantly alter rectification. In the following section we extend the theory of the previous Chapter to account for edge effects.

Edge resistance The introduction of non-negligible edge resistances implies an equivalent electric circuit as illustrated in Figure 5.2(a), which not only considers bulk and surface contributions to the conductance inside the pore (G_b^{pore} and G_s^{pore}) in parallel [226, 227] but also two base- (G_b^{base} and G_s^{base}) and tip- (G_b^{tip} and G_s^{tip}) conductances. Only recently it has been shown that the charged surface outside of the membrane contributes to edge resistance [91, 219], but unfortunately our model is not able to explicitly account for the base- and tip surface conductances (G_s^{base} and G_s^{tip}, respectively) even though we will see these charged regions do contribute significantly to both experimental Ohmic conductance and ICR. Instead we implicitly account for the charge on the outside membrane through an "apparent" (large) surface charge within the pore, inflating the pore surface conductance G_s^{pore} and total conductance G. Hence our large "apparent" surface charge will account for outer-membrane conductance increasing the well-known bulk edge conductances as described by Hall [220].

These parallel edge surface and bulk conductances are in series with the pore resistances as depicted in Fig. 5.2(a), which for the present system parameters ensures that the potential drop over the pore $\Delta\psi_p$ is significantly smaller than the total bias $\Delta\psi$. This decreased potential drop does not only reduce the current through the pore but also lowers the electro-osmotic flow and concentration polarisation within the pore. To obtain $\Delta\psi_p$ we consider, in cylindrical (x,r,θ) coordinates, two bulk reservoirs in the half spaces $x<0$ and $x>L$ connected by an azimuthally-symmetric conical channel of length L as depicted in Figure 5.2(b) with base radius R_b at the inlet ($x=0$) and tip radius R_t at the outlet ($x=L$), such that the radius of the channel reads $R(x)=R_b-(x/L)(R_b-R_t)$ for $x\in[0,L]$. The potential drop over the inside of the pore can be calculated using two assumptions: (i) that the electric field at the tip (and base) decays as a monopole $-\nabla\psi \propto 1/(r^2+x^2)$ into the bulk far from the pore (as noted by Ref. [222]) and (ii) that the electric field within the pore is divergence-free, such that electroneutrality is obeyed. From these assumptions it follows that the pore-potential drop $\Delta\psi_p=-\int_0^L \partial_x\psi \mathrm{d}x$ is given by

$$\Delta\psi_p=\frac{\Delta\psi}{1+\dfrac{\pi}{4L}(R_b+R_t)}, \tag{5.1}$$

which we derive and verify in the Appendix.

We note that the edge resistance is negligible in the long-channel limit $L/R_b \gg 1$, as Eq. (5.1) reduces to $\Delta\psi_p \simeq \Delta\psi$ in this limit. In the geometry of our experiments the reduced potential $\Delta\psi_p$ given by Eq. (5.1) does not only effectively halve the electric current (as $L\approx R_b+R_t$ for the experimental geometries), but as noted it will also significantly influence current rectification. As Eq. (5.1) accounts for

the influence of bulk-edge resistance (red regions in Fig. 5.2(a)) for both the electric current and (electro-osmotic) flow and we use an effective surface charge σ as proxy for the surface-edge resistance G_s^{base} and G_s^{tip}, from now on our mathematical analysis will pertain only to the inner-pore region (green-shaded region in Fig. 5.2(a)) therewith following Ref. [212].

Poisson-Nernst-Planck-Stokes equations The electric potential difference over the pore $\Delta\psi_p$ does not only drive ion fluxes $\mathbf{j}_\pm(x,r)$ of the monovalent cations $(+)$ and anions $(-)$ but also a fluid flow with a velocity field $\mathbf{u}(x,r)$. The salt flux $\mathbf{j}_s = \mathbf{j}_+ + \mathbf{j}_-$ and electro-osmotic flow $\mathbf{u}$ will be key to understanding the electric current $\mathbf{j}_e = \mathbf{j}_+ - \mathbf{j}_-$. The resulting salt concentration $\rho_s(x,r) = \rho_+(x,r) + \rho_-(x,r)$ due to the inhomogeneous salt current is of key importance for current rectification, while the space-charge $e\rho_e(x,r) = e(\rho_+(x,r) - \rho_-(x,r))$ outside the electric double layer is of secondary importance as was shown in Chapter 4. The ionic fluxes and concentrations satisfy the Nernst-Planck equations (5.2)-(5.3) that describe diffusion, conduction, and advection, while the electric potential satisfies the Poisson equation (5.4) in terms of the electric space charge density $e\rho_e$. The fluid flow in the low-Reynolds number regime of interest here is given by the Stokes equation (5.5) that includes an electric body force $-e\rho_e\nabla\psi$, and the steady-state condition of interest leads to the condition of divergence-free fluxes (5.6), which all accumulates into

$$\mathbf{j}_e = -D\big(\nabla\rho_e + \rho_s\frac{e\nabla\psi}{k_BT}\big) + \mathbf{u}\rho_e; \tag{5.2}$$

$$\mathbf{j}_s = -D\big(\nabla\rho_s + \rho_e\frac{e\nabla\psi}{k_BT}\big) + \mathbf{u}\rho_s; \tag{5.3}$$

$$\nabla^2\psi = -\frac{e}{\varepsilon}\rho_e; \tag{5.4}$$

$$\eta\nabla^2\mathbf{u} - \nabla P - e\rho_e\nabla\psi = 0; \tag{5.5}$$

$$\nabla\cdot\mathbf{j}_\pm = 0, \quad \nabla\cdot\mathbf{u} = 0. \tag{5.6}$$

Here Eq. (5.2) shows explicitly that the salt concentration $\rho_s = \rho_+ + \rho_-$ determines the electric conductivity of the charge current $\mathbf{j}_e$. To obtain the pore conductance we consider both reservoirs with a dilute (monovalent) KCl solution of concentration ρ_b, viscosity $\eta = 1$ mPa s, a dielectric permittivity $\varepsilon = 80\varepsilon_0$, with ε_0 the permittivity of vacuum, and a fixed temperature $T = 298$ K, which is constant throughout the system. Deep into the bulk of the base-connected reservoir, $x \ll -L$, we impose that the K^+ and Cl^- concentrations $\rho_\pm = \rho_b$, $P = P_0$, $\psi = \Delta\psi$, and deep into the tip-connected reservoir, $x \gg 2L$, we impose $\rho_\pm = \rho_b$, $P = P_0$, and $\psi = 0$. Here the reference pressure $P_0 = 1$ atm. For K^+ and Cl^- we use equal diffusion coefficients $D = 1$ nm^2 ns^{-1}, which is somewhat smaller than the bulk diffusion constant at 20 °C and 0.1 M [228, 229]. Such a discrepancy between channel and bulk diffusion constants has been noted in Ref. [221].

In thermodynamic equilibrium with a vanishing potential drop between the reservoirs ($\Delta\psi = 0$) and vanishing fluxes, the PNPS equations (5.2)-(5.6) reduce to Poisson-Boltzmann theory that describes a diffuse layer of net ionic charge near the surface, known as the electric double layer (EDL) with typical thickness $\lambda_D = (8\pi\lambda_B\rho_b)^{-1/2}$, and Bjerrum length $\lambda_B = e^2/(4\pi\varepsilon k_B T) \simeq 0.7$ nm. Outside this layer all concentrations $\rho_\pm(x,r)$ are equal to ρ_b and there is no electric field, $-\nabla\psi(x,r) \simeq 0$. In equilibrium the surface charge density $e\sigma$ obeys the Gouy-Chapman equation, $2\pi\lambda_B\lambda_D\sigma = \sinh(e\psi_0/2k_BT)$ [185]. Here ψ_0 is the surface potential of the channel wall, which we will use as a fit parameter below, taken to be constant between all geometries and at all concentrations thereby implicitly accounting for a concentration-dependent surface charge $\sigma(\rho_b)$ due to a salt-concentration dependent surface-reaction [230, 231].

Concentration polarisation For non-vanishing applied potential drops ($\Delta\psi \neq 0$) not only an electric current $I = 2\pi e\hat{\mathbf{x}}\cdot\int_0^R \mathbf{j}_e r\mathrm{d}r$ (with $\hat{\mathbf{x}}$ the unit vector along the x-direction) and electro-osmotic flow $Q = 2\pi\hat{\mathbf{x}}\cdot\int_0^R \mathbf{u}(r)r\mathrm{d}r$ are driven through the pore, but also a salt current $J = 2\pi\hat{\mathbf{x}}\cdot\int_0^R \mathbf{j}_s(r)r\mathrm{d}r$ where the bulk-excess salt current is primarily a conductive current through the EDL. In steady-state this salt current must be laterally constant to prevent the build up of salt through the pore, $\pi R^2(x)\partial_t\bar{\rho}_s = -\partial_x J = 0$, where $\bar{\cdot\cdot\cdot} = (\pi R^2(x))^{-1}\int_0^{R(x)}\cdots r\mathrm{d}r$ denotes the cross-sectional average of the salt concentration. The condition of a divergence-free flux (Eq. (5.6)), which is necessary for a steady-state solution, leads to a differential equation for cross-sectionally averaged salt concentration for $x \in [0, L]$,

$$D\partial_x\left(\pi R^2\partial_x\bar{\rho}_s + 2\pi R\sigma\frac{e\partial_x\psi}{k_BT}\right) - Q\partial_x\bar{\rho}_s = 0, \tag{5.7}$$

with the electric field $-\partial_x\psi = (\Delta\psi_p/L)R_bR_t/R^2(x)$ [212] and the electro-osmotic flow in a conical channel $Q = -\Delta\psi_p(\pi R_tR_b/L)(\varepsilon\psi_0/\eta)$, (as derived in Chapter 4). In Eq. (5.7) the first term represents diffusion of salt through the bulk of the pore, the second term conduction of salt through the EDL, and the third term advection of salt through the bulk of the pore. In a cylinder with constant radius R this differential equation reduces to $D\partial_x^2\bar{\rho}_s - Q\partial_x\bar{\rho}_s = 0$, which with boundary conditions $\bar{\rho}_s(0) = \bar{\rho}_s(L) = 2\rho_b$ has the trivial solution of $\bar{\rho}_s = 2\rho_b$. Thus for straight pores no current rectification is expected. For a conical geometry, the laterally changing radius $R(x)$ causes lateral variation of conductive salt currents $D\partial_x(2\pi R(x)\sigma e\partial_x\psi(x)/k_BT) \neq 0$ which frustrates the formation of a constant J and acts as a non-zero source term. For a negative surface charge, as is typically the case for silica, this source term is negative for $\Delta\psi > 0$ and thus the salt concentration in the pore decreases. For $\Delta\psi < 0$ this source term is positive, and thus the salt concentration increases. Solving for the cross-sectional average concentration

profile $\bar{\rho}_s(x)$ leads to a non-trivial solution (see Chapter 4 with $\Delta P = 0$)

$$\bar{\rho}_s(x) - 2\rho_b = \frac{\Delta\rho}{\mathrm{Pe}}\left[\frac{x}{L}\frac{R_t}{R(x)} - \frac{\exp\left(\frac{x}{L}\frac{R_t^2}{R_b R(x)}\mathrm{Pe}\right) - 1}{\exp\left(\frac{R_t}{R_b}\mathrm{Pe}\right) - 1}\right] \tag{5.8a}$$

$$= \frac{\Delta\rho}{2|\mathrm{Pe}|}\left(\frac{R_b}{R(x)}\big(1 - \frac{x}{L}(1 + \frac{R_t}{R_b})\big) \mp 1\right) \quad \text{if } \pm\mathrm{Pe} \gg \left(\frac{R_b}{R_t}\right)^2, \tag{5.8b}$$

where the tip Péclet number $\mathrm{Pe} \equiv -\Delta\psi_p(R_b/R_t)(\varepsilon\psi_0/D\eta)$ and $\Delta\rho \equiv 4(e\Delta\psi_p/k_BT)\,\mathrm{Du}(R_b/R_t - 1)\rho_b$ is a measure for the concentration polarisation, with tip Dukhin number $\mathrm{Du} = \sigma/(2\rho_b R_t)$. Note that both Pe and Du carry a sign and the diode polarity stems from the sign of the Dukhin number.

Conductance Having obtained the salt-concentration $\bar{\rho}_s(x)$ in Eq. (5.8) the resulting pore conductance $G(\Delta\psi) = I(\Delta\psi)/\Delta\psi$ is calculated by cross-sectionally integrating Eq. (5.2) which results in

$$G(\Delta\psi) = G_b(\Delta\psi)\left(1 + \frac{4\langle\lambda_D\rangle}{R_b + R_t}\big(\cosh\big(\frac{e\psi_0}{2k_BT}\big) - 1\big)\right), \tag{5.9}$$

here $\langle\cdots\rangle = L^{-1}\int_0^L \cdots \mathrm{d}x$ denotes the lateral average, and the bulk channel conductance is given by $G_b(\Delta\psi) = 4\langle\bar{\rho}_s\rangle R_t R_b(e^2D/k_BT)/(4L/\pi + R_b + R_t)$. This bulk conductance also accounts for the in- and outlet resistance by incorporation of Eq. (5.1) and depends on $\Delta\psi$ through the potential dependence of $\langle\bar{\rho}_s\rangle$, which is obtained by numerical integration of Eq. (5.8). We note that Eq. (5.9) obtained from the PNPS equations (5.2)-(5.6) has precisely the form expected from the circuit depicted in Fig. 5.2(a): it consists of the sum of a bulk and surface (pore) conductance, $G = G_b + G_s$ (Fig. 5.2(a, green)), whereas the tip and base conductances (Fig.(5.2(a, red)) stand in series with the pore and lower the total conductance per Eq. (5.1). The surface conductance $G_s = 4G_b\langle\lambda_D\rangle/(R_b + R_t)\big(\cosh(e\psi_0)/(2k_BT) - 1\big)$ will vary with concentration through the dependence of the "channel-weighted" Debye length $\langle\lambda_D\rangle \simeq (4\pi\lambda_B\langle\bar{\rho}_s\rangle)^{-1/2}$. In principle we could include the advective (streaming current) contribution to Eq. (5.9), but its contribution to the surface conductance is proportional to $k_BT\,/$
$(4\pi\eta\lambda_B D(\cosh(e\psi_0/2k_BT) - 1)) \ll 10^{-2}$ for all our parameter sets and hence can be neglected [11].

Limiting conductance It is important to note that while the advective contribution to the electric current I can be neglected the advective contribution to the salt current J (Eq. (5.7)) is key to current rectification as for ICR the flow rate determines the characteristic voltage $\Delta\psi_c$, known as the knee voltage for diodes.

When $\Delta\psi_c \gg |\Delta\psi|$ conductance is Ohmic (G_0), while for $\pm\Delta\psi \gg \Delta\psi_c$ the limiting diode conductance ($G_\pm$) has been reached. From Eq. (5.8)b it can be seen that for large flow $|\mathrm{Pe}| \gg (R_b/R_t)^2$ the concentration profile $\bar{\rho}_s(x) - 2\rho_b \propto \Delta\rho/|\mathrm{Pe}|$ is potential independent and hence per Eq. (5.9) this limiting conductance $G_\pm$ has been reached. Hence the characteristic potential $\Delta\psi_c$ is set by the potential for which $\mathrm{Pe}=(R_b/R_t)^2$ yielding

$$\frac{e\Delta\psi_c}{k_B T} = w(R_b/R_t)[1 + (\pi/4L)(R_b + R_t)], \tag{5.10}$$

where $w = eD\eta/(k_B T\varepsilon|\psi_0|)$ is the (dimensionless) ratio of the ionic to electro-osmotic mobility that quantifies the competition between the rate by which conduction adds ions to the concentration profile $\bar{\rho}_s(x)$ and electro-osmotic flow removes them. Note that this ratio depends only on electrolyte properties and surface potential and it is not influenced by the geometry whatsoever, being constant ($w \simeq 0.3$) over all our geometries and concentrations. The term in the square brackets of Eq. (5.10) accounts for edge resistance and can be set to unity in the long-channel limit.

While Eq. (5.9) can be used to describe the conductance for arbitrary $\Delta\psi$ by straightforward numerical integration of Eq. (5.8a), a more convenient closed form for the limiting conductances $G_\pm$ can be found when neglecting the second (surface) term for the electric conductance $G(\Delta\psi)$ in Eq. (5.9). This approximation therefore neglects surface conductance entirely and subsequently integrating Eq. (5.8b) yields

$$\frac{G_{\pm,b}}{G_{0,b}} = 1 + 2w\mathrm{Du}\left[\frac{\log\left(R_b/R_t\right)}{R_b/R_t - 1} - \left(\frac{R_t}{R_b}\right)^{\frac{1\pm1}{2}}\right]. \tag{5.11}$$

As such, current rectification is defined by the ratio $G_-/G_+ = \mathrm{ICR}$ where, as before, $\mathrm{Du}=\sigma/(2\rho_b R_t)$ represents the ratio of salt transport in the EDL with respect to salt transport in the bulk. The bracketed term of Eq. (5.11) fully captures the effect of geometry on the concentration profile $\bar{\rho}_s(x)$. This last term is zero for $R_t = R_b$, positive for G_+ and negative for G_- and reflects the influence of geometry on diode polarity. Eq. (5.11) also straightforwardly gives a simple and convenient analytic expression for the ICR = G_-/G_+.

In the following sections we consider the small and large potential limits of Eq. (5.9) to interpret the experimental data by first considering the measured (Ohmic) conductance G_0 at small potential drops $|\Delta\psi| < \Delta\psi_c$ and then to describe ICR, which is given by the ratio of conductances G_-/G_+ in the limit of large positive (+) or negative (-) potential drops for $\pm\Delta\psi \gg \Delta\psi_c$.

5.4 Ohmic conductance

First we consider the Ohmic conductance, G_0, which is found at small potential drops $|\Delta\psi| < \Delta\psi_c$ (Eq. (5.10)). In this case the laterally averaged concentration equals the bulk concentration $\langle\bar{\rho}_s\rangle = 2\rho_b$. Hence G_0 is given by Eq. (5.9) where the bulk Ohmic conductance $G_{0,b} = 8R_tR_b(e^2D/k_BT)/(4L/\pi + R_b + R_t)\rho_b$ and the surface Ohmic conductance $G_{0,s}$ is determined by the equilibrium Debye length $\lambda_D = (8\pi\lambda_B\rho_b)^{-1/2}$. In this regime we find that Eq. (5.9) reduces to several well-known results depending on the geometry. The conductance of a long conical channel with negligible surface conductance is retrieved when $L \gg R_b > R_t \gg \lambda_D$ [212], the Hall conductance of a thin cylindrical pore with negligible surface conductance is retrieved when $L \simeq R_b = R_t \gg \lambda_D$ [220], and the conductance of a long cylindrical channel [11] is obtained when $L \gg R_b = R_t > \lambda_D$. Hence Eq. (5.9) extends these classical results to short pores with unequal tip and base radii.

Figure 5.3 shows the experimental Ohmic conductance obtained as $G_0 = (I(0.05\ \text{V}) - I(-0.05\ \text{V}))/0.1\ \text{V}$ together with our theoretical model Eq. (5.9) for all four channels T1, T2, S1 and S2, where we use $\psi_0 = -0.21$ V as it provides the closest match to the data for all concentrations and geometries. Note that the classical long-channel theory that neglects entrance resistance through Eq. (5.1) would overestimate the conductance by a factor of about two for our parameters, as the effective potential drop is nearly halved ($0.46 < \Delta\psi_p/\Delta\psi < 0.68$) in the experimental geometries. This reduction of the effective potential drop highlights the importance of edge resistances. It should be emphasized that the experimental conductance in Fig. 5.3 is normalized by the theoretical bulk conductance $G_{0,b}$ from Eq. (5.9), which is determined by both pore geometry and electrolyte properties. At high concentrations this representation highlights that the surface conductance is negligible, as the conductance in units of $G_{0,b}$ approaches unity and the experimental data for different geometries collapse into a single curve, showing that Eq. (5.9) properly accounts for the in- and outlet resistance at the highest concentration. Some of the deviation between experimental data and theory are attributed to morphological changes due to clogging over the course of the experiments (see for instance SEM image of T1 after the experiments in SI-5 of Ref. [181]).

At low concentrations, $\rho_b < 1$ mM, both the theoretical and experimental conductance rapidly increase as the concentration decreases, which is due to the surface conductance $G_{0,s}$ contribution increasing with the increasing Debye screening length. We observe that the concentration at which surface conductance becomes comparable to bulk conductance occurs when the tip Dukhin number approaches unity, $G_{0,s}/G_{0,b} \propto \text{Du} = \sigma/(2\rho_bR_t) \simeq 1$, which for both T1 and T2 occurs near $\rho_b \simeq 2$ mM for $\psi_0 = -0.21$ V. The experimental variation of conductance with concentration roughly scales as the inverse square of the concentration, in-

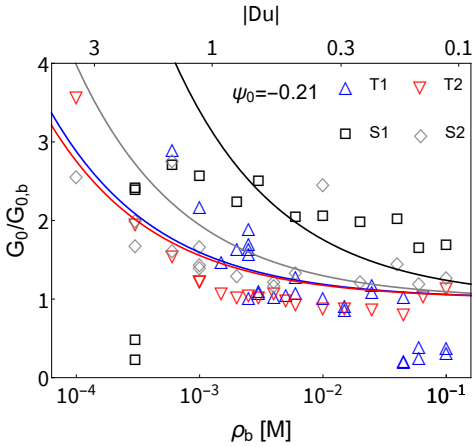

Figure 5.3: Ohmic conductance G_0 in units of the bulk conductance $G_{0,b}$ as a function of the bulk concentration ρ_b (lower axis) and Dukhin number Du$= \sigma/(2\rho_b R_t)$ (upper axis) with tip radius $R_t = 0.5$ μm representative for the tapered pores T1 and T2 and straight pores S1, but not for the straight pore S2 with radius $R_t = 1.5$ μm. The symbols denote the experimental measurements and the lines with corresponding colors are plotted using Eq. (5.9) with a large surface potential $\psi_0 = -0.21$ V (see text). As expected the conductance converges to the bulk conductance at high-concentration while it increases to triple the bulk conductance at low concentrations due to the contribution of surface conductance.

creasing by a factor of three when the concentration is decreased by a factor ten. This scaling can only be understood by using a concentration-independent ψ_0 as opposed to a concentration-independent surface charge density σ. With constant σ the Dukhin number scales as Du $\propto \rho_b^{-1}$ and introduces a surface conductance which varies by orders of magnitude in our concentration range, which is not observed. Instead, when using a constant ψ_0 the surface charge scales as $\sigma \propto 1/\lambda_D$ according to the Gouy-Chapman equation, in which case the proper scaling Du $= \sigma/(2\rho_b R_t) \propto \rho_b^{-1/2}$ is immediately obtained. The existence of a constant surface potential implies that a chemical reaction is responsible for the surface charge varying with salt concentration. However, while Fig. 5.3 indeed shows that the experimental conductance qualitatively follows the inverse square-root scaling, there is a minor quantitative deviation. We attribute this chiefly to charge-regulation beyond the constant-potential model of the silica-water interface [232], which could introduce variations in ψ_0 by a factor ~ 3 in the range $[10^{-1} - 10^{-4}]$ M for silica [112, 230, 231]. We have not included this concentration effect as there is no unanimous quantitative measurement of charge-regulation for silica [21, 112, 230–232] and as to prevent overfitting.

5.5 Ion current rectification

We now turn to large potential drops where $|\Delta\psi| \gg \Delta\psi_c$ (Eq. (5.10)) where we observe significant current rectification for tapered pores T1 and T2 and the conductance has converged to its limiting value $G_\pm$ (Eq. (5.11)). Current rectification in conical pores is well established to be due to the salt concentration in the pore changing with the applied potential [156–158, 212]. The dependence of the laterally averaged salt concentration $\langle\bar{\rho}_s\rangle$ on $\Delta\psi$ as in Eq. (5.8) in conjunction with our expression for the conductance Eq. (5.9) immediately result in a voltage-dependent conductance. In Fig. 5.4(a) we use Eq. (5.8) to plot the salt concentration profiles $\rho_s(x)/(2\rho_b)$ in the conical pore T1 for $\Delta\psi$ between -0.5 V and 0.5 V and a concentration $\rho_b = 6$ mM. It can be seen that for negative voltages there is a build-up of ions, while for positive voltage drops the pore becomes depleted.

This increase and decrease of the salt concentration, characteristic of the conical geometry, is highly dependent on the applied voltage, but converges to a limiting concentration profile for which inhomogeneous conduction is balanced by advection. These limiting concentration profiles can deviate up to 50% from the bulk concentration and in turn significantly modulate the voltage-dependent conductance as can be seen in Fig. 5.4(b). Here we compare $G(\Delta\psi)$ from Eq. (5.9) with the experimental conductance normalized by the experimental Ohmic conductance $G(\Delta\psi = 0)$. We observe two plateaus of high and low conductance for the theoretical curves at large negative and positive voltages for the tapered pores. The transition between the two regimes occurs at the borders of the shaded region $|\Delta\psi| \leq \Delta\psi_c \simeq 0.05$ V beyond which the conductance quickly converges to the limiting conductance $G_\pm$. See SI-7 of Ref. [181] for more plots at different concentrations for comparison, which all show the same typical S-shaped curve with the exception for curves at $\rho_b < 1$ mM for which the experimental variation is larger due to leakage currents as discussed in Section 5.2.

In Fig. 5.4(c) we plot the experimental ICR against concentration and tip Dukhin number, together with results based on both Eq. (5.11) (solid) and the combination of Eq. (5.8a) and Eq. (5.9) (dashed) using a fitted surface potential $\psi_0 = -0.28$ V in both cases. Theoretical and experimental ICR obey the same inverse square root scaling $G_-/G_+ \propto \rho_b^{-1/2}$ as was also observed for Ohmic conductance, which is again due to the concentration dependence of Du at fixed surface potential ψ_0. Interestingly, we find that Eq. (5.11) is a good approximation for the combination of Eq. (5.8a) and Eq. (5.9). The unexpected quality of our approximation Eq. (5.11) is a result of a cancellation of errors: an increase of Ohmic conduction due to surface conductance decreases ICR while the variation of surface conductance with concentration increases ICR.

At low concentrations the inverse square root dependence of ICR breaks down

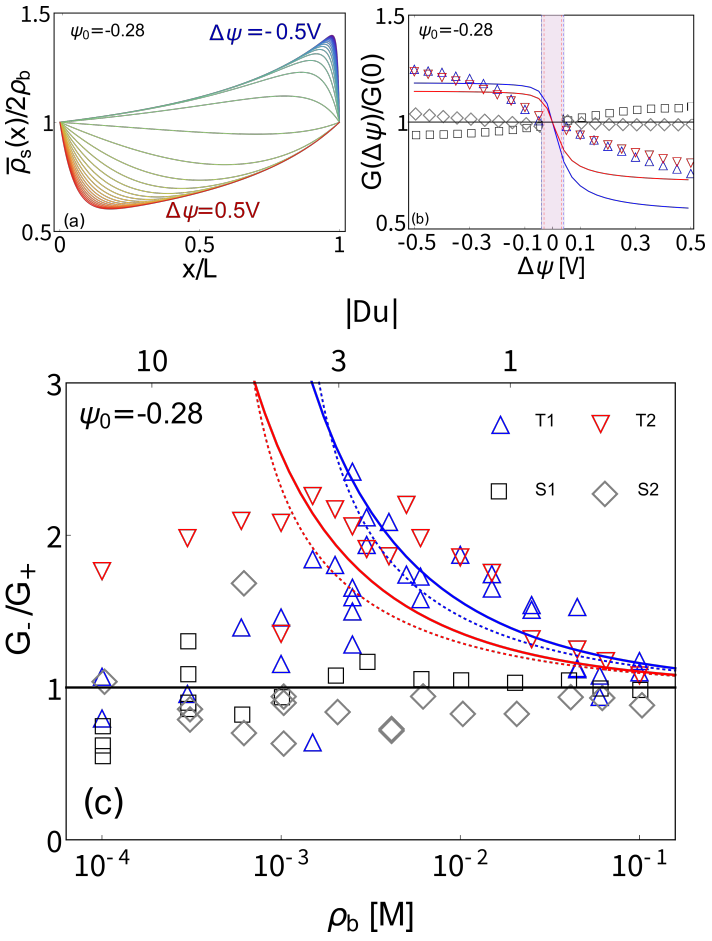

Figure 5.4: (a) Concentration profiles $\bar{\rho}_s(x)/2\rho_b$ for geometry T1 (see text) at a bulk concentration $\rho_b = 6$ mM as calculated by Eq. (5.8) for $\Delta\psi$ between -0.5 and 0.5 V with step-size of 0.03 V. Depletion occurs for positive potentials (red) while concentration increases at negative potentials (blue). (b) Conductance normalized by the conductance at $\Delta\psi = 0$ at varying potentials and the same concentration as in (a) where the different symbols represent the tapered (T1=blue,T2=red) and straight (S1=black,S2=gray) channels, and lines are plotted using the combination of Eq. (5.8a) and Eq. (5.9) both with a surface potential of $\psi_0 = -0.28$ V. Vertical lines demarcating shaded area are placed at the characteristic voltage $\Delta\psi_c \simeq \pm 0.05$ V with color corresponding to the respective geometry. Most variation of the experimental conductance occurs within the shaded region, after which the conductance converges to the limiting conductances $G_\pm$. (c) Current rectification given by the ratio G_-/G_+ which for experiments is taken as $G(\pm 0.5$ V) with varying concentration (lower axis) and Dukhin number for $R_t = 0.5$ μm (upper axis). Solid lines are plotted with our approximation Eq. (5.11) that neglects surface conductance and dotted lines are from the full solution using the combination of Eq. (5.8a) and Eq. (5.9) both using $\psi_0 = -0.28$ V. Peak experimental current rectification is reached near Du $\simeq$ 3 while solid lines grow monotonically with Du.

around $\rho_b \simeq 2$ mM, where the experimental ICR peaks while our theory predicts that ICR should keep increasing with decreasing concentration. Such a peak in ICR has been previously observed in long micrometer-channels [156, 177, 215] where it was assigned to the emergence of EDL overlapping at low-concentrations. In our work the concentration depletion in the pore allows for minor EDL overlap at the tip at large positive potential drops where the concentration in the tip approaches zero due to depletion and hence the Debye length diverges. Other theoretical works predict that in this case of overlapping double layers a peak in ICR at $1 <$Du< 10 [183, 184], which is attributed to salt transport in the EDL dominating the total salt transport, an effect that is not captured in our model. See SI-9 in Ref.[181] for the pore selectivity as defined in Ref. [183] for our tapered geometries with $\psi_0 = -0.21$ V and find a maximum near $\rho_b = 2$ mM, in line with the experiments.

5.6 Discussion of the large surface potential

Both conductance G_0 and current rectification G_-/G_+ are visually fitted using ψ_0 as the only fit parameter which we keep constant for all geometries and concentrations, yielding $\psi_0 = -0.21$ V for G_0 and $\psi_0 = -0.28$ V for G_-/G_+. However, the surface chemistry of the silica interface is well studied, and a much lower surface potential between -0.03 V and -0.1 V is expected in the experimental conditions of interest here [21]. While surface potentials may vary quite significantly between different measurement methods, protocols and even subsequent measurements [21], a discrepancy that exceeds 0.1 V is excessive. From the Gouy-Chapman equation we find that a pore with a surface potential between -0.21 and -0.28 V would contain approximately 15-60 times more charge than for a typical literature surface potential of -0.07 V. Such a large discrepancy cannot be explained by subtle experimental factors. Induced charge due to membrane capacitance may partly explain the large apparent charge at large applied potentials ($\Delta\psi$) [233]. However, previous work found that induced charge on 55 nm thick silicon membranes is comparable to the surface charge of silica [234]. As the membrane capacitance and therefore the induced charge scales with the inverse of membrane thickness, we expect the (material specific) influence of induced charge to be minor in the 2 μm thick membranes used here. Furthermore, the large apparent charge required to explain Ohmic conductance at $\Delta\psi \sim 0$, can not be justified by induced charge. We therefore assume that this deviation stems from our theoretical model not including all of the key physics.

In our analysis we exclude the charge on the planar membrane outside the pore, effectively neglecting an edge EDL conductance G_s^{base} and G_s^{tip} as depicted in Fig. 5.2(a). Other authors have noted that this region on the outside of the pore can contribute to both the Ohmic conductance [219, 221] and the current

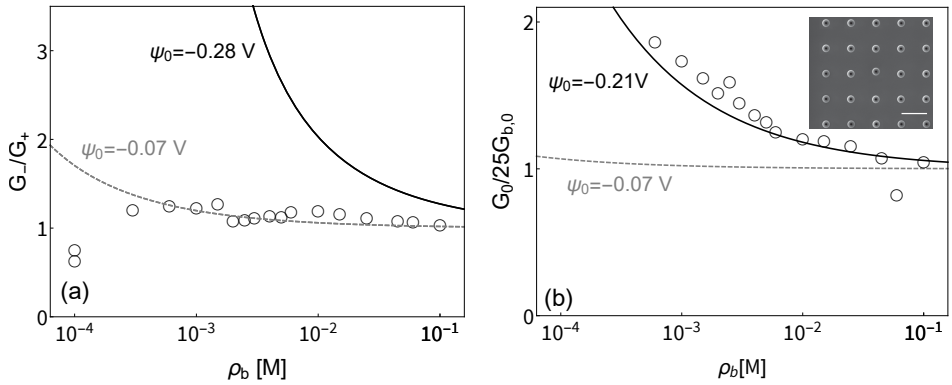

Figure 5.5: (a) Current rectification G_-/G_+ as function of concentration (lower axis) for an array of 25 pores. The symbols denote the experimental measurements and the lines are plotted using Eq. (5.11) using a surface potential of $\psi_0 = -0.28$ V (black, continuous) and $\psi_0 = -0.07$ V (gray, dashed). No current rectification is found in the experiment, in line with a pore with a surface potential of $\psi_0 = -0.07$ V. (b) Dimensionless Ohmic conductance G_0 in units of the bulk conductance $G_{0,\mathrm{b}}$ in the same representation as in Fig. 5.3 with lines plotted using Eq. (5.9). The measured conductance corresponds essentially to 25 times the conductance of a single pore with $\psi_0 = -0.21$ V. The inset of (b) shows an SEM image of the array directly after fabrication, the scale bar is 10 μm.

rectification [222, 223] for thin pores with $R_\mathrm{b}/L \leq 1$. The charge on the outside of the membrane not only increases the edge conductance as noted by [91, 219] but surprisingly can also induce excess ICR [222]. This excess ICR is due to a radial electric field driving an inhomogeneous salt current through the EDL ouside of the pore, leading to accumulation/depletion of salt in the reservoir as we demonstrate in the Appendix. While excess ICR and excess conductance both occur in the EDL outside of the pore, they are distinct phenomena whose scaling and characteristic length scales may differ qualitatively, explaining why the experimental G_0 and G_-/G_+ are better accounted for with two different surface potentials, $\psi_0 = -0.21$ V and $\psi_0 = -0.28$ V, respectively.

Considering that the charge on the outside of the membrane can contribute to both ICR and increased conductance we suggest to assign the excess charge from the large, fitted, surface potential ψ_0 to the charge located on the planar membrane outside of the pore. We estimate the charged surface area A_out outside the pore contributing to current rectification as $A_\mathrm{out} = A_\mathrm{pore}\big((\sigma_\mathrm{app}/\sigma_\mathrm{lit}) - 1\big)$, where A_out is the (circular) area outside of the pore contributing to entrance-surface conductance, A_pore is the surface area of the conical pore, $\sigma_\mathrm{app} = \sinh(\psi_0 e/2k_\mathrm{B}T)\ /(2\pi\lambda_\mathrm{B}\lambda_\mathrm{D})$ is the apparent (Gouy-Chapman) surface charge density resulting from the fitted surface potential (with $\psi_0 = -0.21$ V for Ohmic conductance and $\psi_0 = -0.28$ V for ICR) and $\sigma_\mathrm{lit} = \sinh(-0.07\ \mathrm{V}(e/2k_\mathrm{B}T))/(2\pi\lambda_\mathrm{B}\lambda_\mathrm{D})$ is the surface charge density as calculated from a literature surface potential of 0.07 V. With these values

we find that the outer-membrane EDL within a radius of about 15.0 μm from the pore center contributes to ICR, while a shorter radius of only 7.4 μm contributes to Ohmic conductance. This latter value closely corresponds to the Dukhin length $\sigma/(2\rho_b) \simeq 7$ μm at 10^{-4} M which was predicted by Refs. [91, 219] to set the length-scale for (Ohmic) outer-membrane surface conductance.

To verify this larger surface contribution of 15 μm for ICR we derive a solution for the concentration polarisation far from the pore in the Appendix, and find that the concentration profile in the bulk obeys a long-ranged inverse square law decay $\rho_s(x,r) \propto (r^2+x^2)^{-1}$ like the electric field with a prefactor proportional to the inverse aspect ratio R_b/L. This prefactor indicates that outer-membrane concentration polarisation only occurs for short pores, while the inverse square decay indicates that the concentration profile decays over lengths much larger than the pore radius. Both these observations support the hypothesis that surface charge far from the pore can contribute to current rectification for low-aspect ratio pores. Unfortunately we were unable to construct a theory simultaneously accounting for concentration polarisation in- and outside the pore, while numerical (COMSOL) calculations of the full PNPS Eqs.(5.2)-(5.6) proved unstable.

To experimentally test our hypothesis a 5×5 array of conical pores with dimensions $R_t \simeq 0.35$ μm, $R_b \simeq 1.4$ μm and $L \simeq 2$ μm with a spacing of 10 μm between the pore centers ($\approx 10^6$ pores/cm^2) was constructed by our collaborators. In Fig. 5.5(a) we show the ICR calculated with Eq. (5.11) using the literature surface potential $\psi_0 = -0.07$ V (dashed line) and the large surface potential obtained from the single pore fitted with $\psi_0 = -0.28$ V (solid line) together with the experimental data for the array (symbols). We observe that ICR is greatly reduced for the array, virtually disappearing over the whole concentration range. In contrast the Ohmic conductance of the array is essentially 25 times the single pore conductance given by Eq. (5.9) as shown in Fig. 5.5(b). Considering that the single pore results are based on the fitted value of ψ_0 = -0.21 V, the surface conductance therefore remains excessively large compared to that expected for a literature surface potential of $\psi_0 = -0.07$ V (solid line). In line with our hypothesis, these observations therefore surprisingly imply that the charge on the outside of the membrane contributes over a smaller range to conductance than to ICR, so that interference only occurs for the latter at this spacing.

5.7 Conclusion

To conclude, we have presented a theoretical analysis off ion current rectification (ICR) in tapered micropores connecting aqueous KCl solutions, leading to three main results.

(i) We analysed the ionic current rectification in conical micropores fabricated

in crystalline silicon membranes without further chemical modification at KCl concentrations where the (bulk) electrolyte screening length is much smaller than the pore size, and which is absent in straight cylindrical pores.

(ii) We derive an expression for the conductance of short conical pores accounting for both the EDL within the channel as well as the edge resistance at the tip and base of the pore. These edge resistances approximately halve the Ohmic conductance in the experimental geometries. Our expression (Eq. (5.9)) reverts to the Hall conductance in case of thin cylindric pores [220], to the conical conductance in case of long cones [212], and to the well-known conductance of straight cylinders with surface conductance for large aspect ratio channels [11]. We find an expression for the characteristic voltage at which current rectification occurs, $\Delta\psi_c \simeq 0.05$ V in our geometries, and find a new closed-form expression (Eq. (5.11)) for the limiting ICR at large potential drops. While, like other authors, we find that rectification scales with the Dukhin number, our expression contains two new dimensionless terms: the ratio w of the ionic and electro-osmotic (fluid) mobility and a term describing the influence on geometry which solely depends on the tip-to-base ratio. Using two different surface potentials ($\psi_0 = -0.21$ V for Ohmic conductance and $\psi_0 = -0.28$ V) our theory closely matches the experimental results for all but the lowest concentrations and largest potential drops. In this regime of extreme depletion minor EDL overlap occurs at the tip, invalidating the starting assumption of non-overlapping EDL's in our theory.

(iii) Finally, we discuss the physical interpretation of the surface potential ψ_0 which is our sole fit parameter. Our fitted surface potential is excessively large compared to literature values and should not be interpreted as the actual potential but rather as an apparent surface potential. This apparent potential is inflated by the contribution of charge on the outside of the membrane, a region explicitly excluded from our theoretical description. We estimate from the fitted ψ_0 that charge on the membrane surface within about 7.4 μm of the pore contributes to (Ohmic) conductance at low potentials and within 15.0 μm to ICR at larger potentials. We test this hypothesis by considering an array of 25 pores with a 10 μm separation of the pore centers ($\approx 10^6$ pores/cm^2) with no overlap of the low potential (Ohmic) interaction length and large overlap of the high potential (ICR) interaction length. While we observe no pore-pore interference for Ohmic conduction at low potentials, we indeed find that ICR vanishes in the array, in agreement with our hypothesis. The interaction length for Ohmic conduction is known to be set by the Dukhin length [91, 219] while for ICR we show that a long-ranged, inverse-square-distance decay determines the pore-pore interaction, in line with the experimental observations. For thin membranes this apparent contribution of the charge on the outside of the membrane to both surface conductance and ICR may be beneficial for single pores, however these contributions could be detrimental in densely packed arrays that would be desirable for applications. Further

investigation of the interaction length for outer-membrane conductance and ICR with different pore densities is therefore particularly relevant.

5.8 Appendix

5.8.1 Calculation of the electric field

In this section we will calculate the electric field $-\nabla\psi$ not only within the pore but also in both reservoirs. This analysis supposes that the space charge ρ_e outside the EDL is negligible, ensuring that the electric field is divergence free $\nabla^2\psi = 0$. We assume (i) that the electric field in the bulk reservoirs far from the pore $\sqrt{r^2+x^2} \gg R_b$ is isotropic and decays like an electric monopole by the inverse square law $\propto 1/(r^2+x^2)$ and, (ii) that no electric field permeates the channel walls. The far-from-pore assumption (i) breaks down in the near-pore region $r^2+x^2 \simeq R_b^2$ where the electric field diverges and therefore a characteristic cut-off length scale for this asymptotic decay has to be identified. Natural length scales would be the tip and base radii R_t and R_b near which the far-from-pore solution fails, but to obtain quantitative agreement with numerical calculations we have to multiply the base and tip radii by $\pi/4$. Choosing this factor will also reproduce the exact resistance for a cylindrical, 2D-pore as derived by Hall [220]. Following assumption (ii) the field inside the conical pore $0 < x < L$ scales as $\partial_x\psi \propto 1/(\pi R^2(x))$ as the total, radially integrated, lateral electric field has to be constant. Combining these expression we find the electric field over the centre axis $r = 0$ is given by

$$-\partial_x\psi(x, r=0) = \begin{cases} \dfrac{\alpha\pi^2}{4}\Delta\psi\left(\dfrac{\pi}{4}R_b - x\right)^{-2} & \text{if } x < 0; \\ \alpha\Delta\psi R^{-2}(x) & \text{if } 0 < x < L; \\ \dfrac{\alpha\pi^2}{4}\Delta\psi\left(x + \dfrac{\pi}{4}R_t - L\right)^{-2} & \text{if } x > L, \end{cases} \tag{A5.1}$$

where the constant length $\alpha = R_b R_t/(4L + \pi(R_b + R_t))$ can be found by requiring that the electric field is continuous at the pore edges, the total potential drop equals $\psi(-\infty) - \psi(\infty) = \Delta\psi$. The maximum electric field (at the tip) is equal to $\alpha\Delta\psi/R_t^2$. We have chosen to evaluate the electric field on the center line where the field is purely axial as to give an explicit expression for one of the vector components of $-\nabla\psi$. Furthermore we note that this component is of greatest interest as it is responsible for the axial currents through the pore. In Fig. A5.1 we compare the analytic expression of the electric field (Eq. (A5.1)) over the central axes and find good agreement with numerical results.

5.8.2 Inlet-outlet concentration polarisation

In this section we will construct a far-from-pore solution demonstrating concentration-polarisation in the bulk reservoir with $x < 0$ connected to the pore base. Instead of the cylindrical (x, r, θ) coordinates used in the main text it will be convenient to treat the problem in spherical (s, ϕ, θ) coordinates with $s^2 = x^2 + r^2$

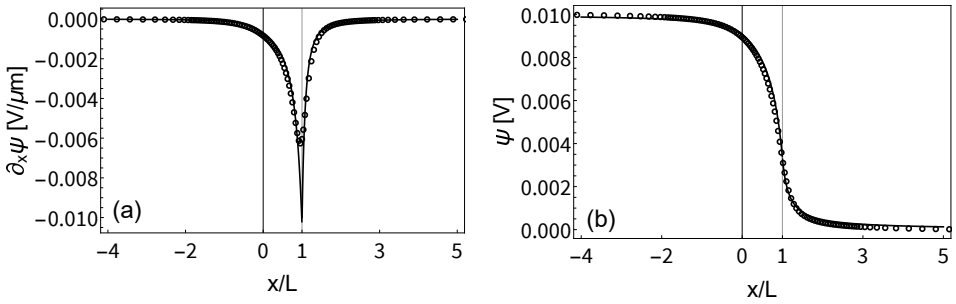

Figure A5.1: (a) Gradient of the electric potential $\partial_x\psi(x)$ and (b) electric potential $\psi(x)$ along the central axis $r = 0$ for the T1 geometry (see the main text) at a vanishing surface potential and $\rho_b = 1$ mM for $\Delta\psi = 0.01$ V with symbols from numerical calculations and lines resulting from Eq. (A5.1). This parameter set is representative for the experimental system at high concentrations, where surface conductance is negligible. The base and tip locations are at $x = 0$ and $x = L$ denoted by vertical lines. There is good agreement between numerical and analytic results.

and $\cos\phi = x/\sqrt{x^2+r^2}$. We consider fluxes far from the pore opening $s \gg L$ where the electric field Eq. (A5.1) simplifies to $\partial_s\psi \simeq -\alpha\pi^2\Delta\psi/(4s^2)$. The aim here is to calculate $\hat{\rho}_s(s)$, with $\cdot\hat{\cdot}\cdot = (2\pi s^2)^{-1}\int_0^{2\pi}\int_{\pi/2}^{\pi}\cdots s^2\sin(\phi)\mathrm{d}\phi\mathrm{d}\theta$ the average over a hemisphere centered on the origin extending in the bulk with radius s. The hemispherical average $\hat{\rho}_s(s)$ is not representative for the local concentration $\rho_s(s,\theta,\phi)$ which is expected to have a large ϕ dependence as the electric double layer is localized at $\phi = \pi/2$ and the far-from-pore Landau-Squire [77] solution for the fluid flow $\mathbf{u}(s,\phi)$ is much larger at $\phi = \pi$ than at $\phi = \pi/2$. Both these complicating factors will expectedly yield a concentration profile with larger deviations from bulk concentration near the membrane surface $\phi = \pi/2$ compared to $\phi = \pi$. Nevertheless our expression for $\hat{\rho}_s(s)$ can explain two experimental observations, (i) concentration-polarisation in the bulk reservoir is expected in the small-pore limit $L/R_b \simeq 1$ and (ii) the concentration profile extends long distances into the bulk, exhibiting long-ranged, inverse-square decay.

Inhomogeneous salt flux Integrating the radial component $j_{s,s}(s,\phi)$ of the salt flux to obtain the total salt flux $\hat{J}(s) = \int_0^{2\pi}\mathrm{d}\theta\int_{\pi/2}^{\pi}\mathrm{d}\phi\sin(\phi)s^2 j_{s,s}(s,\phi)$ and imposing the stationarity condition $\partial_s\hat{J} = 0$ we find a differential equation for the concentration $\hat{\rho}_s(s)$ averaged over a hemisphere,

$$D(2\pi\partial_s(s^2\partial_s\hat{\rho}) - \frac{\pi^3\alpha\sigma}{2s^2}\frac{e\Delta\psi}{k_BT}) + Q\partial_s\hat{\rho}_s = 0, \tag{A5.2}$$

with s denoting the radius of the hemisphere over which the concentration is averaged, α being defined below Eq. (A5.1) and where $\int_0^{2\pi}\mathrm{d}\theta\int_{\pi/2}^{\pi}\mathrm{d}\phi\sin(\phi)s^2\rho_e(s,\phi) = -2\pi s\sigma$ stems from hemispherical charge-neutrality. Furthermore we made the ap-

proximation that flow can be considered to be isotropic which combined with incompressibility yields $2\pi s^2 u_s(s) = -Q$, where the minus sign was added so that a radially inward flow in the bulk reservoir results in a positive Q following the convention in the main text. Solving Eq. (A5.2) for $\hat{\rho}_\mathrm{s}$ with bulk boundary conditions $\hat{\rho}_\mathrm{s}(\infty) = \partial_s \hat{\rho}_\mathrm{s}(\infty) = 0$ we find

$$\hat{\rho}_\mathrm{s}(s) - 2\rho_\mathrm{b} = \Delta\rho_\mathrm{res}\left(\exp\left(\frac{l_\mathrm{Pe}}{s}\right) - \frac{l_\mathrm{Pe}}{s} - 1\right) \overset{s\gg|l_\mathrm{Pe}|}{\simeq} \frac{\Delta\rho_\mathrm{res}}{2}\left(\frac{l_\mathrm{Pe}}{s}\right)^2, \tag{A5.3}$$

where the measure for the concentration profile extending into the reservoir is

$$\Delta\rho_\mathrm{res} = \frac{\pi\sigma}{4l_\mathrm{Pe}^2}\frac{e\Delta\psi}{k_\mathrm{B}T}\left[\frac{R_\mathrm{b}R_\mathrm{t}}{4L/\pi + R_\mathrm{b} + R_\mathrm{t}}\right], \tag{A5.4}$$

with the Péclet length $l_\mathrm{Pe} = Q/2\pi D$ signifying the distance from the origin at which advective and diffusive transport rates are equal. Note that Q and hence the Péclet length has a sign. The term in square brackets vanishes in the long-channel-limit as the electric-field in the bulk and correspondingly $\Delta\rho_\mathrm{res}$ go to zero in this limit, which shows that no pore-pore interactions are expected for long, thin pores.

While our solution was specifically derived for the base reservoir with $x < 0$ and $\phi \in [\pi/2, \pi]$, our solution Eq. (A5.3) is valid in the tip-connected reservoir with $x > L$ and $\phi \in [0, \pi/2]$ when interchanging $-\Delta\rho_\mathrm{res}$ for $\Delta\rho_\mathrm{res}$ and $-l_\mathrm{Pe}$ for l_Pe as the flow and electric field are anti-symmetric between tip- and base-connected reservoirs. Due to the anti-symmetry of the far-from-pore solutions the depletion in one reservoir leads to a compensating excess in the other reservoir for $s \gg |l_\mathrm{Pe}|$ (where the asymptotic decay is independent from l_Pe) and the only contribution to ICR is expected from the near-pore region. The unphysical divergence of the concentration profile near the pore for positive (inward) flows $s \ll l_\mathrm{Pe}$ prevents us from connecting the far-from-pore solution to the near-pore region. In this regime the large inward flow sweeps up the concentration profile and concentrates it in the near-pore region where the far-from-pore solution breaks down.

Discussion As the flow is always inwards for one of the two reservoirs there is no scenario where the far-from-pore solution can be used to describe the entire experimental system. We note that this focusing of the concentration profile near the base for positive flows also complicates numerical calculations: a significant effort was made to obtain numerical calculations from COMSOL, however no finite-element system could be created that was stable beyond a very narrow parameter regime. Our numerical calculations always showed reservoir concentration polarisation in some form. The near-pore solution is expected to very sensitively depend on all experimental length scales, including Péclet and Dukhin length. A "holistic" model describing the entire concentration profile extending

over both the reservoirs and pore would be desirable as it would allow for quantitative predictions without an "apparent" ψ_0 as fit parameter. This problem is left for future study.

English summary

It has only recently been discovered that when water flows along a mineral surface, the charge of that surface can change dramatically [32]. This finding led to considerable discussion and in **Chapter 2** we resolve this controversy by considering new experimental observations which show down-stream variation in the surface charge upon flow. Our calculations reveal that the flow-induced charge variation result from a delicate interplay between dissolution, charging, flow, and diffusion. We also show that both dissolution and charge gradients will alter mineral-liquid interfaces due to the flow of water seeping through soil.

For many materials the chemical reactions described in Chapter 2 are poorly understood. Recently, experimental techniques have become available that can probe the time-dependence of the charge on the solid-liquid interfaces at sub-second timescales and in **Chapter 3** we provide a theory to describe such experiments. Here we show that a single-time trace of the surface charge contains key information on not only the valency and the number of reacting ions, but also on the mechanism by which these ions react and that the nonlinear kinetics are similar to those of autocatalytic reactions. Reexamining several experiments in the literature we find they exhibit characteristic features of our model.

In **Chapter 4** we consider non-linear transport through conical pores, whose unique transport behaviour has made this geometry attractive for a variety applications. One such exotic phenomenon is the dramatic pressure sensitivity of the electric current through a pore, which was only recently demonstrated experimentally [173]. We describe this mechanosensitive diodic behavior theoretically, which requires disentangling the complex and subtle interplay of inhomogeneous ion and fluid fluxes which are all driven by a simultaneous pressure and voltage drop over the channel. We do not only find the optimal pressure drop for diodic behaviour, but also reveal the optimal geometry.

In **Chapter 5** we extend the theory of the Chapter 4 to describe experiments with ultra-short, micrometer, cones with large radii and short lengths. In line with our theory such conical pores exhibit significant current rectification. However, to quantitatively account for the observed conductance a very large surface potential is needed in our theoretical model, from which we infer that surface charge on the outside of the membrane contributes to rectification. We show that the entrance resistance of the thin pores is not only of key importance for the Ohmic conductance but also influences their diodic conductance.

Nederlandse samenvatting

Pas onlangs is ontdekt dat wanneer water langs een mineraal stroomt, de oppervlakte lading van het mineraal sterk verandert [32]. Deze bevinding heeft tot aanzienlijke discussies geleid en in **Hoofdstuk 2** lossen we deze controverse op door een nieuwe experimentele observatie uit te leggen. Onze berekeningen laten zien dat de door stroming geïnduceerde verandering van de lading op het oppervlakte het resultaat is van een subtiele wisselwerking tussen oplossing, oplading, stroming en diffusie. We laten ook zien dat gradienten van dissolutie en lading zich natuurlijk kunnen vormen wanneer water door de aarde sijpelt.

Er is vaak weinig bekend over de chemische reacties die verantwoordelijk zijn voor de lading op mineralen in water, zoals beschreven in Hoofdstuk 2. In **Hoofdstuk 3** laten we zien dat chemische informatie verkregen kan worden door de dynamiek van de oppervlakte lading te bestuderen. Zo is niet alleen de valentie en het aantal reactieve ionen te bepalen, maar ook het mechanisme waarmee deze ionen reageren. We laten zien dat de chemische kinetiek sterk lijkt op de kinetiek van autocatalytische reacties. We gebruiken onze theorie om enkele experimenten uit de literatuur opnieuw te interpreteren, en concluderen dat deze experimenten karakteristieken uit ons model vertonen.

In **Hoofdstuk 4** beschrijven we niet-lineair transport door kegelvormige kanalen, wiens unieke transport eigenschappen uitermate geschikt zijn voor een verscheidenheid aan toepassingen. Een voorbeeld van een bijzondere vorm van transport is de extreme drukgevoeligheid van elektriciteit door een kegelvormig kanaal [173]. We beschrijven de drukgevoeligheid van dit transport theoretisch, waarvoor we eerst de complexe en subtiele wisselwerking tussen inhomogene ionische en fluïde stromen moeten ontwarren. Uit onze analyse volgt niet alleen de optimale druk voor diodisch transport, maar ook de optimale geometrie voor het kegelvormige kanaal.

In **Hoofdstuk 5** gebruiken we de theorie van Hoofdstuk 4 om experimenten te beschrijven met korte kegelvormige kanalen, waarvan de radius en lengte beide ongeveer 1 micrometer zijn. Zulke kanalen vertonen significante rectificatie van de elektrische stroom, maar een kwantitatieve beschrijving van deze rectificatie vereist echter een onrealistisch hoog oppervlakte potentiaal. Hieruit concluderen we dat de lading op de buitenkant van het membraan sterk bijdraagt aan rectificatie. We laten zien dat de weerstand van de kanaal ingang niet alleen van belang is voor de Ohmische weerstand, maar ook het diodische gedrag beinvloedt.

Acknowledgments

First and foremost I would like to thank my promoter, RENÉ VAN ROIJ. You are an excellent teacher and not only took the time to train me as a researcher but also as a physicist. You had endless patience teaching me the precision and clarity required, skills that will stay with me for the foreseeable future. Your enthusiastic exclamation *"but that's PHYSICS!"* was often motivation to work through an evening. That your reaction was even more enthusiastic if your initial idea was disproven speaks to your relaxed and inquisitive nature. I am very grateful to have done my doctoral studies with you.

I would also like to thank my co-promoter MARJOLEIN DIJKSTRA. Over the last four years you were often the voice of reason, clearly setting priorities when I managed to convince René with some far-fetched proposal. You pushed every paper to be as good as it could possibly be, and it is certain that this thesis would be worse both scientifically and stylistically without your clear feedback. When things got rocky you always kept the PhD on course.

An endless source of motivation were all the students I had the privilege to work with: IMA, MARGOT, ELEONARA , TIM VEENSTRA, THIJS and TIM KAMSMA. Your motivation was contagious and your projects brought a wealth of knowledge into our group: IMA, your work on membranes gave us foresight on how pore-pore interactions could behave well before they were found in experiments. MARGOT, your independent study of neuronal transport taught us many concepts from scratch, and has been used as a departure point for further studies at the Herseninstitute. ELEONORA your thorough investigation of concentration-driven transport remains a useful warning to not naïvely extend any of our results to diffusio-osmosis. TIM VEENSTRA: it is hardly necessary to highlight your contributions as our work is already presented in this thesis. However I would like to note how pleasant it was to work with you. THIJS and TIM KAMSMA, you were an incredibly productive duo whose styles really complemented each other. Your projects are difficult to disentangle but their results actually inspired the majority of the current research in our group.

Similarly I would like to thank the experimentalists I was fortunate enough to work with. PATRICK, you ran beautiful and convincing experiments, which were actually clean enough to write theory for. You were open enough to accept some of my opinions on your experiments, but also discerning enough to tell me to come back with better arguments. I thoroughly enjoyed our productive discus-

sions and it is a shame we never got to meet for a beer. MARK we came a long way from what should have been a simple project. The back-and-forth between experimental data and theory turned out to be very productive and your question "*What does this parameter tell me?*" has become a golden rule. I would also like to thank the other experimental collaborators for their work: MISCHA BONN, ELLEN BACKUS from Mainz and BLAISE CUÉNOD, ESTHER ALARCÓN LLADÓ from Amsterdam. I would especially like to thank ESTHER for her intuitive explanations of sometimes esoteric theory.

Of all my other colleagues I would like to start with thanking BEN for showing me the ropes when I just started. My close colleagues PETER, JEROEN RODENBURG, CHENG, ALEXANDER and HAOLAN: I loved discussing science with you and your presence made any meeting great regardless of the content. The lunches with MEIKE, JEROEN ROBERTS, WILLIAM, ANOUAR, MIKAEL and all the others were always welcome breaks. I still believe we should install a gong to announce lunch time. JURRIAAN, JOREN, EMANUELE and PEDRO I hope you didn't notice but I secretly learned a lot of physics from you while pretending to know what we were discussing. I hope to continue learning more from everybody in the future.

All work and no play is not good and hereby I would like to thank my friends outside of academia: THOMAS ZWART for loud and memorable concerts , THIJS KIEBOOM and KOEN for the outlandish discussions. RAKESH, BERTJAN, THOMAS BLOM, JONAS, the TAPUIT ASSOCIATION, BOKSVERENIGING VERBON thanks for the weird adventures. Special shout-out to RAKESH for helping me design the thesis cover. Old friends JEF and JURRE: be afraid because now I am finished with my PhD you may actually see more of me.

Last but certainly not least I would like to thank those that are the foundation of my life: family. My parents ANDRIES and ANOUK: always there, always time. My best memories are at the dinner table, eating pancakes at 8 years old, omelettes at 16 and pimpelen at 24. My sister ANNA: you always impress me with your inexhaustible positive energy, which made you a great maid-of-honor. I would like to thank my parents-in-law WIL and BERNADET for being a second home for me, one where I chop and saw in the garden to my hearts content.

To SANNE: I am so immensely enjoying building a life together with you.

Voor Sanne, bij wie ik aard

About the author

Willem Quirin Boon was born 31st of May 1994 in Haarlem. He went to Stedelijk Gymnasium Haarlem, and became interested in science doing chemistry in his parents garage. He started his Bachelor in Chemistry in 2012 at Utrecht University where he worked on several projects, studying for example the energy transfer between lanthanide ions, and the co-evolution of protein pairs. During his Bachelor thesis he studied the spin-crossover transition of metal organic frameworks, under joint-supervision of Jun Tao and Andries Meijerink at the department of Chemistry in Xiamen. After graduating in 2016 he started the Master "Nanomaterials: Chemistry and Physics", including the Complex Systems graduate track. His Masters thesis at the Van 't Hoff laboratory with Ben Erné and Alex Silfhout was on the sedimentation of magnetic particles in strong magnetic field gradients. He graduated cum laude in 2018.

In 2018 he started as a PhD researcher at the Institute of Theoretical Physics under supervision of René van Roij and Marjolein Dijkstra, where he studied non-linear electrokinetic transport. The main results of his work, described in this thesis, have been presented at five (inter)national conferences and are all published in peer-reviewed scientific journals. During his PhD project, Willem supervised six student thesis projects and was a teaching assistant for several physics courses.

Bibliography

[1] C. Goupil, *Continuum theory and modeling of thermoelectric elements* (John Wiley & Sons, 2015).

[2] T. J. Seebeck, *Magnetische polarisation der metalle und erze durch temperatur-differenz* (W. Engelmann, 1822).

[3] L. Onsager, Physical review **37**, 405 (1931).

[4] D. J. Griffiths, "Introduction to electrodynamics," (2005).

[5] K. Huang, *Statistical mechanics* (John Wiley & Sons, 2008).

[6] K. S. Thorne and R. D. Blandford, *Modern classical physics: optics, fluids, plasmas, elasticity, relativity, and statistical physics* (Princeton University Press, 2017).

[7] G. D. Phillies, *Elementary lectures in statistical mechanics* (Springer Science & Business Media, 2000).

[8] H. B. G. Casimir, Reviews of Modern Physics **17**, 343 (1945).

[9] D. G. Miller, Chemical Reviews **60**, 15 (1960).

[10] C. Herrero and L. Joly, arXiv preprint arXiv:2105.00720 (2021).

[11] B. L. Werkhoven and R. van Roij, Soft Matter **16**, 1527 (2020).

[12] Y. Uematsu, Journal of Physics: Condensed Matter **33**, 423001 (2021).

[13] M. Borkovec, B. Jönsson, and G. J. Koper, in *Surface and Colloid Science* (Springer, 2001) pp. 99–339.

[14] B. S. Massey and J. Ward-Smith, *Mechanics of fluids* (Crc Press, 2018).

[15] M. J. Kadhim and M. I. Gamaj, Journal of Chemical Reviews **2**, 182 (2020).

[16] M. S. Kilic, M. Z. Bazant, and A. Ajdari, Physical review E **75**, 021503 (2007).

[17] Y. Avni, R. M. Adar, D. Andelman, and H. Orland, Physical Review Letters **128**, 098002 (2022).

[18] R. M. Adar, Y. Uematsu, S. Komura, and D. Andelman, Physical Review E **98**, 032604 (2018).

[19] L. Bocquet and J.-L. Barrat, Soft matter **3**, 685 (2007).

[20] A. T. Bui, F. L. Thiemann, A. Michaelides, and S. J. Cox, arXiv preprint arXiv:2210.14040 (2022).

[21] M. Kosmulski, *Chemical properties of material surfaces*, Vol. 102 (CRC press, 2001).

[22] L. Šamaj and E. Trizac, Physical Review E **100**, 042611 (2019).

[23] E. Mangaud and B. Rotenberg, The Journal of Chemical Physics **153**, 044125 (2020).

[24] K. Pongsangangan, T. Ludwig, H. Stoof, and L. Fritz, Physical Review B **106**, 205126 (2022).
[25] S. R. De Groot and P. Mazur, *Non-equilibrium thermodynamics* (Courier Corporation, 2013).
[26] J. Fair and J. Osterle, The Journal of Chemical Physics **54**, 3307 (1971).
[27] P. Peters, R. Van Roij, M. Z. Bazant, and P. Biesheuvel, Physical review E **93**, 053108 (2016).
[28] S. R. De Groot and P. Mazur, *Non-equilibrium thermodynamics* (Courier Corporation, 2013) chapter IV, paragraph 3, Eq. 53.
[29] A. T. Yeung, C.-n. Hsu, and R. M. Menon, Journal of Geotechnical Engineering **122**, 666 (1996).
[30] J. Schaefer, G. Gonella, M. Bonn, and E. H. Backus, Physical Chemistry Chemical Physics **19**, 16875 (2017).
[31] P. A. Covert and D. K. Hore, Annual Review of Physical Chemistry **67**, 233 (2016).
[32] D. Lis, E. H. Backus, J. Hunger, S. H. Parekh, and M. Bonn, Science **344**, 1138 (2014).
[33] X. Wang, C. Cheng, S. Wang, and S. Liu, Microfluidics and Nanofluidics **6**, 145 (2009).
[34] S. R. Rao, *Surface chemistry of froth flotation: Volume 1: Fundamentals* (Springer Science & Business Media, 2013).
[35] Á. V. Delgado, F. González-Caballero, R. Hunter, L. Koopal, and J. Lyklema, Journal of Colloid and Interface Science **309**, 194 (2007).
[36] S. Porada, R. Zhao, A. Van Der Wal, V. Presser, and P. Biesheuvel, Progress in Materials Science **58**, 1388 (2013).
[37] G. E. Brown Jr, A. L. Foster, and J. D. Ostergren, Proceedings of the National Academy of Sciences **96**, 3388 (1999).
[38] E. Saxegaard and G. Rølla, Caries Research **23**, 406 (1989).
[39] C. Lian, X. Kong, H. Liu, and J. Wu, Physical Chemistry Chemical Physics **21**, 6970 (2019).
[40] B. L. Werkhoven, J. C. Everts, S. Samin, and R. van Roij, Physical Review Letters **120**, 264502 (2018).
[41] J. Schaefer, E. H. G. Backus, and M. Bonn, Nat Commun **9**, 3316 (2018).
[42] Y. Xie, L. Fu, T. Niehaus, and L. Joly, Physical Review Letters **125**, 014501 (2020).
[43] J. Lützenkirchen, T. Scharnweber, T. Ho, A. Striolo, M. Sulpizi, and A. Abdelmonem, Journal of Colloid and Interface Science **529**, 294 (2018).
[44] P. Ober, W. Q. Boon, M. Dijkstra, E. H. Backus, R. van Roij, and M. Bonn, Nature Communications **12**, 1 (2021).
[45] Y. Xi, Q. Xiao, J. Du, X. Ye, X. Kong, Z. Chang, T. Li, H. Jin, J. Wang, and H. Lin, Advanced Materials Interfaces **7**, 1902046 (2020).

[46] S. M. Hamza and S. K. Hamdona, The Journal of Physical Chemistry **95**, 3149 (1991).

[47] S. M. Hamza and S. K. Hamdona, Journal of crystal growth **125**, 591 (1992).

[48] J. Miller, K. Fa, J. Calara, and V. Paruchuri, Colloids and Surfaces A: Physicochemical and Engineering Aspects **238**, 91 (2004).

[49] J. Miller and J. B. Hiskey, Journal of Colloid and Interface Science **41**, 567 (1972).

[50] S. Assemi, J. Nalaskowski, J. D. Miller, and W. P. Johnson, Langmuir **22**, 1403 (2006).

[51] A. Herbillon, in *Iron in soils and clay minerals* (Springer, 1988) pp. 251–266.

[52] B. A. Fleming, Journal of Colloid and Interface Science **110**, 40 (1986).

[53] P. V. Brady and J. V. Walther, Geochimica et Cosmochimica acta **53**, 2823 (1989).

[54] P. J. Scales, F. Grieser, T. W. Healy, L. R. White, and D. Y. Chan, Langmuir **8**, 965 (1992).

[55] S. H. Behrens and D. G. Grier, The Journal of Chemical Physics **115**, 6716 (2001).

[56] M. Wang and A. Revil, Journal of Colloid and Interface Science **343**, 381 (2010).

[57] S. L. Brantley, *Kinetics of water-rock interaction* (Springer, 2008) pp. 151–210.

[58] L. Li, C. I. Steefel, and L. Yang, Geochimica et Cosmochimica Acta **72**, 360 (2008).

[59] K. Beven and P. Germann, Water resources research **18**, 1311 (1982).

[60] K. Beven and P. Germann, Water resources research **49**, 3071 (2013).

[61] A. G. Lambert, P. B. Davies, and D. J. Neivandt, Applied Spectroscopy Reviews **40**, 103 (2005).

[62] M. Bonn, Y. Nagata, and E. H. Backus, Angewandte Chemie International Edition **54**, 5560 (2015).

[63] S. Azam, A. Darlington, and J. M. Gibbs-Davis, Journal of Physics: Condensed Matter **26**, 244107 (2014).

[64] M. S. Azam, C. N. Weeraman, and J. M. Gibbs-Davis, The Journal of Physical Chemistry Letters **3**, 1269 (2012).

[65] M. S. Azam, C. N. Weeraman, and J. M. Gibbs-Davis, The Journal of Physical Chemistry C **117**, 8840 (2013).

[66] A. M. Darlington and J. M. Gibbs-Davis, The Journal of Physical Chemistry C **119**, 16560 (2015).

[67] A. M. Darlington, T. A. Jarisz, E. L. DeWalt-Kerian, S. Roy, S. Kim, M. S. Azam, D. K. Hore, and J. M. Gibbs, The Journal of Physical Chemistry C **121**, 20229 (2017).

[68] E. L. DeWalt-Kerian, S. Kim, M. S. Azam, H. Zeng, Q. Liu, and J. M. Gibbs, The Journal of Physical Chemistry Letters **8**, 2855 (2017).

[69] B. Rehl, Z. Li, and J. M. Gibbs, Langmuir **34**, 4445 (2018).

[70] R. Khatib, E. H. Backus, M. Bonn, M.-J. Perez-Haro, M.-P. Gaigeot, and M. Sulpizi, Scientific reports **6**, 1 (2016).

[71] P. Malgaretti, M. Janssen, I. Pagonabarraga, and J. M. Rubi, The Journal of Chemical Physics **151**, 084902 (2019).

[72] R. B. Bird, W. E. Stewart, E. N. Lightfoot, and R. E. Meredith, Journal of The Electrochemical Society **108**, 78C (1961).

[73] J. Newman, Journal of Heat and Mass Transfer (1969).

[74] A. Belhocine and W. Z. Wan Omar, Revista científica , 6 (2018).

[75] R. B. Bird, W. Stewart, and E. Lightfoot, *Transport phenomena, Revised Se* (John Wiley & Sons, New York, 2006).

[76] G. I. Barenblatt, G. I. Barenblatt, and B. G. Isaakovich, *Scaling, self-similarity, and intermediate asymptotics: dimensional analysis and intermediate asymptotics* (Cambridge University Press, 1996).

[77] L. D. Landau and E. M. Lifshitz, *Fluid Mechanics: Landau and Lifshitz: Course of Theoretical Physics, Volume 6*, Vol. 6 (Elsevier, 2013).

[78] M. S. Nair, M. Tomar, S. Punia, W. Kukula-Koch, and M. Kumar, International Journal of Biological Macromolecules (2020).

[79] S. Croll, Progress in Organic Coatings **44**, 131 (2002).

[80] M. C. Karlsson, Z. Abbas, R. Bordes, Y. Cao, A. Larsson, A. Rolland, P. Taylor, and B.-M. Steenari, Progress in Organic Coatings **125**, 279 (2018).

[81] C. D. Anderson, P. R. Taylor, and C. G. Anderson, in *Inter. Miner. Processing Congress Proceedings* (2016) pp. 1–15.

[82] M. Fuerstenau, D. Rice, P. Somasundaran, and D. Fuerstenau, Inst. Min. Metall. Trans **74**, 381 (1965).

[83] S. R. Rao, *Surface chemistry of froth flotation: Volume 1: Fundamentals* (Springer Science & Business Media, 2013).

[84] W. Zheng, Y. Jia, W. Chen, G. Wang, X. Guo, and X. Jiang, ACS Applied Materials & Interfaces **9**, 21181 (2017).

[85] A. Dhall, S. Islam, M. Park, Y. Zhang, A. Kim, and G. Hwang, ACS Applied Materials & Interfaces **13**, 40379 (2021).

[86] Z. Leonenko, M. Rodenstein, J. Döhner, L. M. Eng, and M. Amrein, Langmuir **22**, 10135 (2006).

[87] J. Brown, G. E., A. L. Foster, and J. D. Ostergren, Proc Natl Acad Sci U S A **96**, 3388 (1999).

[88] M. Kleber, I. C. Bourg, E. K. Coward, C. M. Hansel, S. C. Myneni, and N. Nunan, Nature Reviews Earth & Environment **2**, 402 (2021).

[89] Y. S. Ho, J. Ng, and G. McKay, Separation and purification methods **29**, 189 (2000).

[90] S. Ringe, E. L. Clark, J. Resasco, A. Walton, B. Seger, A. T. Bell, and K. Chan, Energy & Environmental Science **12**, 3001 (2019).

[91] L. Bocquet, Nature Materials **19**, 254 (2020).

[92] S. Faucher, N. Aluru, M. Z. Bazant, D. Blankschtein, A. H. Brozena, J. Cumings, J. Pedro de Souza, M. Elimelech, R. Epsztein, J. T. Fourkas, *et al.*, The Journal of Physical Chemistry C **123**, 21309 (2019).

[93] M. Kosmulski, *Chemical properties of material surfaces*, Vol. 102 (CRC press, 2001).

[94] M. Kosmulski, *Chemical properties of material surfaces*, Vol. 102 (CRC press, 2001) p. 590.

[95] V. Tandon, S. K. Bhagavatula, W. C. Nelson, and B. J. Kirby, Electrophoresis **29**, 1092 (2008).

[96] E. J. W. Verwey and J. T. G. Overbeek, Journal of Colloid Science **10**, 224 (1955).

[97] T. Hiemstra, W. H. Van Riemsdijk, and G. Bolt, Journal of Colloid and Interface Science **133**, 91 (1989).

[98] A. T. Celebi, M. Barisik, and A. Beskok, Microfluidics and Nanofluidics **22**, 7 (2018).

[99] T. Mouterde and L. Bocquet, Eur Phys J E Soft Matter **41**, 148 (2018).

[100] B. Werkhoven, J. C. Everts, S. Samin, and R. van Roij, Physical Review Letters **120**, 264502 (2018).

[101] M. F. Döpke, F. W. van der Meij, B. Coasne, and R. Hartkamp, Physical Review Letters **128**, 056001 (2022).

[102] P. Ober, W. Q. Boon, M. Dijkstra, E. H. Backus, R. van Roij, and M. Bonn, Nature Communications **12**, 1 (2021).

[103] G. Gonella, C. Lütgebaucks, A. G. De Beer, and S. Roke, The Journal of Physical Chemistry C **120**, 9165 (2016).

[104] M. Hayashi, Y. J. Shiu, K. K. Liang, S. H. Lin, and Y. R. Shen, J Phys Chem A **111**, 9062 (2007).

[105] Z. Zhang, L. Piatkowski, H. J. Bakker, and M. Bonn, Nature Chemistry **3**, 888 (2011).

[106] M. Kosmulski, *Chemical properties of material surfaces*, Vol. 102 (CRC press, 2001) p. 531.

[107] W. Rudzinski and W. Plazinski, The Journal of Physical Chemistry B **110**, 16514 (2006).

[108] D. D. Do, *Adsorption analysis: equilibria and kinetics*, Vol. 2 (Imperial college press London, 1998).

[109] S. Sen Gupta and K. G. Bhattacharyya, Adv Colloid Interface Sci **162**, 39 (2011).
[110] L. K. Koopal and M. J. Avena, Colloids and Surfaces A: Physicochemical and Engineering Aspects **192**, 93 (2001).
[111] L. Koopal, W. Tan, and M. Avena, Colloids and Surfaces A: Physicochemical and Engineering Aspects **577**, 709 (2019).
[112] R. K. Iler, *The colloid chemistry of silica and silicates*, Vol. 80 (LWW, 1955) p. 666.
[113] B. Grosjean, C. Pean, A. Siria, L. Bocquet, R. Vuilleumier, and M. L. Bocquet, J Phys Chem Lett **7**, 4695 (2016).
[114] J. Febrianto, A. N. Kosasih, J. Sunarso, Y.-H. Ju, N. Indraswati, and S. Ismadji, Journal of Hazardous Materials **162**, 616 (2009).
[115] P. Venema, T. Hiemstra, and W. H. van Riemsdijk, Journal of Colloid and Interface Science **192**, 94 (1997).
[116] J. Westall and H. Hohl, Advances in Colloid and Interface Science **12**, 265 (1980).
[117] W. Van Riemsdijk, J. De Wit, L. Koopal, and G. Bolt, Journal of Colloid and Interface Science **116**, 511 (1987).
[118] I. Langmuir, Journal of the American Chemical society **40**, 1361 (1918).
[119] M. Kosmulski, *Chemical properties of material surfaces*, Vol. 102 (CRC press, 2001) p. 582, 582.
[120] M. J. Avena and L. K. Koopal, Environmental Science & Technology **33**, 2739 (1999).
[121] W. Rudzinski and W. Plazinski, Applied Surface Science **253**, 5827 (2007).
[122] L. Krumina, J. P. Kenney, J. S. Loring, and P. Persson, Chemical Geology **427**, 54 (2016).
[123] D. Ebeling, D. van den Ende, and F. Mugele, Nanotechnology **22**, 305706 (2011).
[124] E. Cheb-Terrab and T. Kolokolnikov, arXiv preprint math-ph/0007023 (2000).
[125] T. Mahadevan and S. Garofalini, The Journal of Physical Chemistry C **112**, 1507 (2008).
[126] G. K. Lockwood and S. H. Garofalini, The Journal of Physical Chemistry C **118**, 29750 (2014).
[127] T. S. Mahadevan and J. Du, Journal of the American Ceramic Society **103**, 3676 (2020).
[128] A. I. Hanopolskyi, V. A. Smaliak, A. I. Novichkov, and S. N. Semenov, ChemSystemsChem **3**, e2000026 (2021).
[129] P. Schuster, Monatshefte für Chemie-Chemical Monthly **150**, 763 (2019).
[130] A. K. Horváth and I. Nagypál, ChemPhysChem **16**, 588 (2015).

[131] A. Cassani, A. Monteverde, and M. Piumetti, Journal of Mathematical Chemistry **59**, 792 (2021).

[132] M. C. Cross and P. C. Hohenberg, Reviews of Modern Physics **65**, 851 (1993).

[133] D. Horváth and A. Toth, Journal of the Chemical Society, Faraday Transactions **93**, 4301 (1997).

[134] F. Jafarpour, T. Biancalani, and N. Goldenfeld, Physical Review Letters **115**, 158101 (2015).

[135] F. C. Frank, Biochimica et Biophysica acta **11**, 459 (1953).

[136] A. Yehia and K. Ezzat, Adsorption Science & Technology **27**, 337 (2009).

[137] K. Hachiya, M. Sasaki, T. Ikeda, N. Mikami, and T. Yasunaga, The Journal of Physical Chemistry **88**, 27 (1984).

[138] D. L. Sparks, *Kinetics of soil chemical processes* (Academic Press, 2013) p. 88.

[139] C. Bernasconi, *Relaxation Kinetics* (Academic Press San Diego, 1976).

[140] G. Teschl, *Ordinary differential equations and dynamical systems*, Vol. 140 (American Mathematical Soc., 2012).

[141] Z. Zhang, L. Wen, and L. Jiang, Nature Reviews Materials **6**, 622 (2021).

[142] D.-K. Kim, C. Duan, Y.-F. Chen, and A. Majumdar, Microfluidics and Nanofluidics **9**, 1215 (2010).

[143] A. Siria, P. Poncharal, A.-L. Biance, R. Fulcrand, X. Blase, S. T. Purcell, and L. Bocquet, Nature **494**, 455 (2013).

[144] A. Siria, M.-L. Bocquet, and L. Bocquet, Nature Reviews Chemistry **1**, 1 (2017).

[145] M. Elimelech and W. A. Phillip, Science **333**, 712 (2011).

[146] A. Campione, L. Gurreri, M. Ciofalo, G. Micale, A. Tamburini, and A. Cipollina, Desalination **434**, 121 (2018).

[147] T. M. Squires and S. R. Quake, Reviews of Modern Physics **77**, 977 (2005).

[148] L. Bocquet and E. Charlaix, Chemical Society Reviews **39**, 1073 (2010).

[149] R. B. Schoch, J. Han, and P. Renaud, Reviews of Modern Physics **80**, 839 (2008).

[150] J. C. Eijkel and A. v. d. Berg, Microfluidics and Nanofluidics **1**, 249 (2005).

[151] B. L. Werkhoven, S. Samin, and R. van Roij, The European Physical Journal Special Topics **227**, 2539 (2019).

[152] S. Levine, J. Marriott, G. Neale, and N. Epstein, Journal of Colloid and Interface Science **52**, 136 (1975).

[153] N. Laohakunakorn, V. V. Thacker, M. Muthukumar, and U. F. Keyser, Nano Letters **15**, 695 (2015).

[154] W.-J. Lan, M. A. Edwards, L. Luo, R. T. Perera, X. Wu, C. R. Martin, and H. S. White, Accounts of Chemical Research **49**, 2605 (2016).

[155] G. W. Bishop, M. M. Lopez Jr, P. Ramiah Rajasekaran, X. Wu, and C. R. Martin, The Journal of Physical Chemistry C **119**, 16633 (2015).
[156] H. S. White and A. Bund, Langmuir **24**, 2212 (2008).
[157] C. Wen, S. Zeng, S. Li, Z. Zhang, and S.-L. Zhang, Analytical Chemistry **91**, 14597 (2019).
[158] J. E. Proctor, *Theory of Ion Transport and Ion Current Rectification in Nanofluidic Diodes*, Msc thesis, Clemson University (2021).
[159] D. Woermann, Physical Chemistry Chemical Physics **5**, 1853 (2003).
[160] D. Woermann, Physical Chemistry Chemical Physics **6**, 3130 (2004).
[161] M. L. Kovarik, K. Zhou, and S. C. Jacobson, The Journal of Physical Chemistry B **113**, 15960 (2009).
[162] C.-Y. Lin, L.-H. Yeh, and Z. S. Siwy, The Journal of Physical Chemistry Letters **9**, 393 (2018).
[163] I. Vlassiouk, T. R. Kozel, and Z. S. Siwy, Journal of the American Chemical Society **131**, 8211 (2009).
[164] S. N. Bush, T. T. Volta, and C. R. Martin, Nanomaterials **10**, 571 (2020).
[165] X. Hou, W. Guo, and L. Jiang, Chemical Society Reviews **40**, 2385 (2011).
[166] A. Piruska, M. Gong, J. V. Sweedler, and P. W. Bohn, Chemical Society Reviews **39**, 1060 (2010).
[167] C. Li, T. Xiong, P. Yu, J. Fei, and L. Mao, ACS Applied Bio Materials **4**, 71 (2020).
[168] S. Ghosal, J. D. Sherwood, and H.-C. Chang, Biomicrofluidics **13**, 011301 (2019).
[169] H. Chun and T. D. Chung, Annual Review of Analytical Chemistry **8**, 441 (2015).
[170] C. D. Cox, N. Bavi, and B. Martinac, Cell Reports **29**, 1 (2019).
[171] A. Anishkin, S. H. Loukin, J. Teng, and C. Kung, Proceedings of the National Academy of Sciences **111**, 7898 (2014).
[172] F. Qian, W. Zhang, D. Huang, W. Li, Q. Wang, and C. Zhao, Physical Chemistry Chemical Physics **22**, 2386 (2020).
[173] L. Jubin, A. Poggioli, A. Siria, and L. Bocquet, Proceedings of the National Academy of Sciences **115**, 4063 (2018).
[174] W.-J. Lan, D. A. Holden, and H. S. White, Journal of the American Chemical Society **133**, 13300 (2011).
[175] H. S. White and A. Bund, Langmuir **24**, 2212 (2008).
[176] C. Kubeil and A. Bund, The Journal of Physical Chemistry C **115**, 7866 (2011).
[177] I. Vlassiouk, S. Smirnov, and Z. Siwy, Acs Nano **2**, 1589 (2008), fig.5.
[178] D.-H. Lin, C.-Y. Lin, S. Tseng, and J.-P. Hsu, Nanoscale **7**, 14023 (2015).
[179] J.-P. Hsu, S.-T. Yang, C.-Y. Lin, and S. Tseng, The Journal of Physical Chemistry C **121**, 4576 (2017).

[180] Y. Ai, M. Zhang, S. W. Joo, M. A. Cheney, and S. Qian, The Journal of Physical Chemistry C **114**, 3883 (2010).

[181] M. Aarts, W. Q. Boon, B. Cuénod, M. Dijkstra, R. van Roij, and E. Alarcon-Llado, ACS Applied Materials & Interfaces (2022).

[182] E. Choi, C. Wang, G. T. Chang, and J. Park, Nano Letters **16**, 2189 (2016).

[183] S. Dal Cengio and I. Pagonabarraga, The Journal of Chemical Physics **151**, 044707 (2019).

[184] A. R. Poggioli, A. Siria, and L. Bocquet, The Journal of Physical Chemistry B **123**, 1171 (2019).

[185] A. W. Adamson and A. P. Gast, *Physical Chemistry of Surfaces*, Vol. 150 (Interscience publishers New York, 1967).

[186] M.-S. Chun, S.-Y. Lee, and S.-M. Yang, Journal of Colloid and Interface Science **266**, 120 (2003).

[187] J. Happel and H. Brenner, *Low Reynolds number hydrodynamics: with special applications to particulate media*, Vol. 1 (Springer Science & Business Media, 2012).

[188] T. E. Veenstra, *Strongly Non-Linear Pressure-Induced Ion Currents in Conical Nanopores*, Bsc thesis, Utrecht University (2020).

[189] B. L. Werkhoven and R. van Roij, Soft Matter **16**, 1527 (2020).

[190] M. W. Khan, M. A. Memon, M. N. Khan, and M. M. Khan, JLUMHS **9**, 114 (2010).

[191] D. A. Bies, C. H. Hansen, and C. Q. Howard, *Engineering noise control* (CRC press, 2017).

[192] J. M. Perry, K. Zhou, Z. D. Harms, and S. C. Jacobson, Acs Nano **4**, 3897 (2010).

[193] A. Marcotte, T. Mouterde, A. Niguès, A. Siria, and L. Bocquet, Nature Materials **19**, 1057 (2020).

[194] P. Robin, N. Kavokine, and L. Bocquet, Science **373**, 687 (2021).

[195] S. Faucher, N. Aluru, M. Z. Bazant, D. Blankschtein, A. H. Brozena, J. Cumings, J. Pedro de Souza, M. Elimelech, R. Epsztein, J. T. Fourkas, *et al.*, The Journal of Physical Chemistry C **123**, 21309 (2019).

[196] M. Nishizawa, V. P. Menon, and C. R. Martin, Science **268**, 700 (1995).

[197] I. Vlassiouk, S. Smirnov, and Z. Siwy, Nano Letters **8**, 1978 (2008).

[198] H. Daiguji, Y. Oka, and K. Shirono, Nano Letters **5**, 2274 (2005).

[199] E. B. Kalman, I. Vlassiouk, and Z. S. Siwy, Advanced Materials **20**, 293 (2008).

[200] H. R. Rees, S. E. Anderson, E. Privman, H. H. Bau, and B. J. Venton, Analytical Chemistry **87**, 3849 (2015).

[201] Y. Wang, D. Wang, and M. V. Mirkin, Proceedings of the Royal Society A: Mathematical, Physical and Engineering Sciences **473**, 20160931 (2017).

[202] I. Vlassiouk, T. R. Kozel, and Z. S. Siwy, Journal of the American Chemical Society **131**, 8211 (2009).
[203] A. Piruska, M. Gong, J. V. Sweedler, and P. W. Bohn, Chemical Society Reviews **39**, 1060 (2010).
[204] Z. Liu, S. Zhang, M. Cheng, L. Yang, G. Li, W. Xu, H. Qu, F. Liang, J. Cheng, and H. Li, Analyst **147**, 1803 (2022).
[205] F. H. J. van der Heyden, D. J. Bonthuis, D. Stein, C. Meyer, and C. Dekker, Nano Letters **6**, 2232 (2006).
[206] K. Xiao, L. Jiang, and M. Antonietti, Joule **3**, 2364 (2019).
[207] D. Wang, M. Kvetny, J. Liu, W. Brown, Y. Li, and G. Wang, Journal of the American Chemical Society **134**, 3651 (2012).
[208] D. Wang and G. Wang, Journal of Electroanalytical Chemistry **779**, 39 (2016).
[209] S. H. Han, M.-A. Oh, and T. D. Chung, Chemical Physics Reviews **3**, 031302 (2022).
[210] T. Xiong, K. Zhang, Y. Jiang, P. Yu, and L. Mao, Science China Chemistry **62**, 1346 (2019).
[211] Z. S. Siwy, Advanced Functional Materials **16**, 735 (2006).
[212] W. Q. Boon, T. E. Veenstra, M. Dijkstra, and R. van Roij, Physics of Fluids **34**, 101701 (2022), https://doi.org/10.1063/5.0113035 .
[213] L.-J. Cheng and L. J. Guo, Nano Letters **7**, 3165 (2007).
[214] M. Graf, M. Lihter, D. Unuchek, A. Sarathy, J.-P. Leburton, A. Kis, and A. Radenovic, Joule **3**, 1549 (2019).
[215] J. Cervera, B. Schiedt, R. Neumann, S. Mafé, and P. Ramírez, The Journal of Chemical Physics **124**, 104706 (2006).
[216] K. Zhou, J. M. Perry, and S. C. Jacobson, Annual Review of Analytical Chemistry **4**, 321 (2011).
[217] C.-Y. Lin, C. Combs, Y.-S. Su, L.-H. Yeh, and Z. S. Siwy, Journal of the American Chemical Society **141**, 3691 (2019).
[218] X. He, K. Zhang, T. Li, Y. Jiang, P. Yu, and L. Mao, Journal of the American Chemical Society **139**, 1396 (2017).
[219] C. Lee, L. Joly, A. Siria, A.-L. Biance, R. Fulcrand, and L. Bocquet, Nano Letters **12**, 4037 (2012).
[220] J. E. Hall, The Journal of General Physiology **66**, 531 (1975).
[221] F. Xiang, M. Dong, S. Liang, W. Zhang, and W. Guan, Nanotechnology (2022).
[222] G. Yossifon, P. Mushenheim, Y.-C. Chang, and H.-C. Chang, Physical Review E **81**, 046301 (2010).
[223] Y. Ma, J. Guo, L. Jia, and Y. Xie, ACS Sensors **3**, 167 (2018).
[224] J. Su, D. Ji, J. Tang, H. Li, Y. Feng, L. Cao, L. Jiang, and W. Guo, Chinese Journal of Chemistry **36**, 417 (2018).

[225] S. W. Kowalczyk, A. Y. Grosberg, Y. Rabin, and C. Dekker, Nanotechnology **22**, 315101 (2011).
[226] B. J. Kirby, *Micro-and Nanoscale Fluid Mechanics: Transport in Microfluidic Devices* (Cambridge university press, 2010).
[227] A. V. Delgado, F. González-Caballero, R. Hunter, L. K. Koopal, and J. Lyklema, Pure and Applied Chemistry **77**, 1753 (2005).
[228] H. S. Harned and R. L. Nuttall, Journal of the American Chemical Society **71**, 1460 (1949).
[229] *CRC Handbook of Chemistry and Physics*, Vol. 85 (CRC press, 2004).
[230] M. Szekeres, I. Dékány, and A. De Keizer, Colloids and Surfaces A: Physicochemical and Engineering Aspects **141**, 327 (1998).
[231] W. Janusz, Adsorption Science & Technology **14**, 151 (1996).
[232] C. Zhao, D. Ebeling, I. Siretanu, D. van den Ende, and F. Mugele, Nanoscale **7**, 16298 (2015).
[233] J. P. de Souza, C.-M. Chow, R. Karnik, and M. Z. Bazant, Physical Review E **104**, 044802 (2021).
[234] Y. Yao, C. Wen, N. H. Pham, and S.-L. Zhang, Langmuir **36**, 8874 (2020).